

New Constraints on the Density of the  
Extragalactic Background Light and the  
Discovery of TeV  $\gamma$ -rays from the BL Lac  
1ES 0347-121 and the Extended Source  
HESS J1023-575

**Dissertation**  
**zur Erlangung des Doktorgrades**  
**des Departments Physik**  
**der Universität Hamburg**

vorgelegt von  
Martin Raue  
aus Ulm

Hamburg  
2007

Gutachter der Dissertation:	Prof. Dr. Götz Heinzelmann Prof. Dr. Robert Klanner
Gutachter der Disputation:	Prof. Dr. Götz Heinzelmann Prof. Dr. Beate Naroska
Datum der Disputation:	26. Juli 2007
Vorsitzender des Prüfungsausschusses:	Dr. Hans Dierk Rüter
Vorsitzender des Promotionsausschusses:	Prof. Dr. Günter Huber
Dekan der Fakultät für Mathematik, Informatik und Naturwissenschaften:	Prof. Dr. Arno Frühwald

## Abstract

The H.E.S.S. Collaboration operates a stereoscopic system of four large imaging atmospheric Cherenkov telescopes for the detection of very-high-energy (VHE;  $>100$  GeV)  $\gamma$ -radiation.

In this work the discovery of two new sources of VHE  $\gamma$ -rays with the H.E.S.S. telescopes is reported. The extragalactic source 1ES 0347-121 belongs to the class of BL Lac objects and is the active core of a distant galaxy. It has been discovered with a significance of more than 10 standard deviations, which makes it the most distant source of VHE  $\gamma$ -rays today (redshift  $z = 0.1880$ ). Its spectrum is well described by a power law with photon index  $\Gamma = 3.08 \pm 0.23_{\text{stat}} \pm 0.1_{\text{sys}}$ . The integral flux  $I(E>250 \text{ GeV})$  corresponds to  $\sim 2\%$  of the flux of the Crab Nebula. The VHE spectrum of 1ES 0347-121 is used to derive limits on the diffuse extragalactic photon field (see below), which are found to be only slightly less constraining than the strongest constraints derived previously from the VHE spectrum of the BL Lac 1ES 1101-232 ( $z = 0.186$ ).

The second source is the extended VHE  $\gamma$ -ray source HESS J1023-577, which is associated with the young massive star cluster Westerlund 2 and its surrounding. These young and massive stars exhibit strong stellar winds, which can produce relativistic particles through shocks. For the first time, a source of VHE  $\gamma$ -rays has been firmly associated with such an environment. The VHE energy spectrum ranging from  $\sim 400$  GeV to  $\sim 20$  TeV is well fitted by a power-law function with photon index  $\Gamma = 2.53 \pm 0.16_{\text{stat}} \pm 0.1_{\text{sys}}$ . Possible mechanisms and models for the production of VHE  $\gamma$ -rays in such an environment are discussed and compared with the observed properties of the source.

The space between galaxies is filled with a diffuse photon field, which carries cosmological information about the galaxy and star formation history. Direct measurements of this field in the ultraviolet to far-infrared wavelength regime (extragalactic background light; EBL) are difficult due to dominant foregrounds coming mainly from dust inside our planetary system and other sources in our galaxy. VHE  $\gamma$ -rays from distant sources are attenuated via pair-production with the EBL. The VHE spectra measured on Earth therefore carry an imprint, which together with assumptions about the intrinsic spectrum produced at the source can be used to derive limits on the density of the EBL. In this thesis the spectra of all known extragalactic VHE sources of TeV blazar type are used to derive strong constraints on the density of the EBL over a broad wavelength range. Since the exact shape of the EBL is unknown, a large number of different shapes, derived from a grid in EBL wavelength vs density, are tested. The derived limits are found to be only a factor of 2 - 3 higher than the lower limits from source counts, which implies that the universe is more transparent to VHE  $\gamma$ -rays than previously anticipated.

## Abstrakt

Die H.E.S.S. Kollaboration betreibt ein stereoskopisches System aus vier großen abbildenden Cherenkov-Teleskopen für den Nachweis sehr hochenergetischer  $\gamma$ -Strahlung (VHE;  $>100$  GeV).

In dieser Arbeit wird über den Nachweis zweier neuer Quellen sehr hochenergetischer  $\gamma$ -Strahlung mit den H.E.S.S.-Teleskopen berichtet. Die extragalaktische Quelle 1ES 0347-121 gehört zur Klasse der BL Lac Objekte und ist der aktive Kern einer entfernten Galaxie. Detektiert mit einer Signifikanz von mehr als 10 Standard-Abweichungen, ist es die bisher am weitesten entfernte Quelle sehr hochenergetischer  $\gamma$ -Strahlung (Rotverschiebung  $z = 0.1880$ ). Ihr Energiespektrum läßt sich gut durch ein Potenzgesetz mit Photonindex  $\Gamma = 3.08 \pm 0.23_{\text{stat}} \pm 0.1_{\text{sys}}$  beschreiben. Der integrale Fluss  $I(E > 250 \text{ GeV})$  entspricht  $\sim 2\%$  des Flusses des Krebsnebels. Mit Hilfe des hochenergetische  $\gamma$ -Strahlungsspektrum von 1ES 0347-121 werden Einschränkungen auf die Dichte des extragalaktischen diffusen Photonfeldes bestimmt (s. unten).

Bei der zweiten Quelle handelt es sich um die ausgehnte Quelle HESS J1023-577, die mit dem jungen, massiven Sternenhaufen Westerlund 2 und dessen Umgebung assoziiert wird. Junge und massereichen Sterne strahlen starke Sternwinde ab, die durch Schockbeschleunigung hochenergetische Teilchen produzieren können. Zum erstenmal konnte eine Quelle sehr hochenergetischer  $\gamma$ -Strahlung mit einer solchen Umgebung sicher identifiziert werden. Das Energiespektrum reicht von  $\sim 400$  GeV bis  $\sim 20$  TeV und läßt sich gut durch eine Potenzgesetz mit Photonindex  $\Gamma = 2.53 \pm 0.16_{\text{stat}} \pm 0.1_{\text{syst}}$  beschreiben. Mögliche Mechanismen und Modelle zur Produktion solch sehr hochenergetischer  $\gamma$ -Strahlung werden diskutiert und mit den beobachteten Eigenschaften der Quelle verglichen.

Im Raum zwischen den Galaxien existiert ein diffuses Photonen-Feld, welches Informationen über die kosmologische Geschichte der Galaxien- und Sternentstehung enthält. Direkte Messung dieses Feldes bei ultravioletten bis zu fern-infraroten Wellenlängen ist schwierig, da innerhalb unseres Sonnensystems und unserer Galaxie dominante Vordergrund-Strahlung existiert. Hochenergetische  $\gamma$ -Strahlung von entfernten Quellen wird durch Wechselwirkung (Paar-Erzeugung) mit diesem Feld absorbiert. Die auf der Erde gemessenen Spektren erhalten so einen Abdruck des Feldes, der zusammen mit Annahmen über das intrinsische Spektrum, das an der Quelle erzeugt wird, dazu verwendet werden kann, die Dichte des Strahlungsfeldes einzuschränken. In dieser Arbeit werden die Spektren aller bekannten extragalaktischen Quellen hochenergetischer  $\gamma$ -Strahlung vom Typ TeV-Blazar dazu verwendet, starke Einschränkungen auf das diffuse extragalaktische Photonen-Feld über einen weiten Bereich in der Wellenlänge zu berechnen. Da der exakte spektrale Verlauf dieses Photon-Feldes unbekannt ist, werden eine große Anzahl unterschiedlicher Verläufe getestet, die aus einem Gitter in Wellenlänge gegen Dichte des Photon-Feldes abgeleitet werden. Die bestimmten Einschränkungen liegen nur einen Faktor 2 bis 3 höher als die unteren Grenzen ermittelt aus Quellen-Zählungen. Das Universum ist somit deutlich transparenter für hochenergetische  $\gamma$ -Strahlung als ursprünglich angenommen.

# Contents

<b>1</b>	<b>Introduction</b>	<b>1</b>
<b>2</b>	<b>Imaging Atmospheric Cherenkov Telescopes</b>	<b>5</b>
2.1	Introduction . . . . .	5
2.2	Cosmic Rays . . . . .	5
2.3	Production Mechanism and Sources of VHE $\gamma$ -rays . . . . .	7
2.4	Air Showers . . . . .	8
2.5	Imaging Atmospheric Cherenkov Telescopes . . . . .	10
2.6	Stereoscopic Observations and Reconstruction . . . . .	13
2.7	The H.E.S.S. Experiment . . . . .	16
2.8	Data Analysis for H.E.S.S. . . . .	18
<b>3</b>	<b>New Constraints on the EBL from the Spectra of all known TeV Blazars</b>	<b>21</b>
3.1	Introduction . . . . .	21
3.2	The Extragalactic Background Light (EBL) . . . . .	21
3.3	Limiting the EBL with VHE $\gamma$ -ray Observations . . . . .	25
3.4	VHE $\gamma$ -ray Attenuation from the Extragalactic Background Light . . . . .	26
3.5	Grid Scan with Spline Function . . . . .	27
3.6	TeV Blazar Spectra . . . . .	31
3.7	Exclusion Criteria . . . . .	34
3.8	Results for individual Spectra . . . . .	38
3.8.1	Close by and well measured: Mkn 501 (HEGRA) . . . . .	44
3.8.2	Intermediate distance, wide energy range: H1426+428 . . . . .	44
3.8.3	Distant source, hard spectrum: 1ES 1101-232 . . . . .	45
3.8.4	<i>Extreme</i> Case: $\Gamma_{\max} > 2/3$ . . . . .	45
3.9	Combined Results . . . . .	47
3.10	Estimation of Systematic Errors . . . . .	50
3.11	Summary and Conclusions . . . . .	55
<b>4</b>	<b>Discovery of VHE <math>\gamma</math>-rays from the distant High Frequency Peaked BL Lac 1ES 0347-121</b>	<b>57</b>
4.1	Introduction . . . . .	57
4.2	Active Galactic Nuclei (AGN) . . . . .	57
4.3	Models for VHE $\gamma$ -ray emission in TeV blazars . . . . .	59
4.3.1	Leptonic Models (EC, SSC) . . . . .	60
4.3.2	Hadronic Models . . . . .	61
4.4	Extragalactic VHE $\gamma$ -ray Sources: Status of Observation . . . . .	61

4.5	Discovery of VHE $\gamma$ -rays from 1ES 0347-121 . . . . .	62
4.5.1	The High Frequency Peaked BL Lac 1ES 0347-121 . . . . .	62
4.5.2	H.E.S.S. Dataset and Analysis Results . . . . .	63
4.5.3	SWIFT X-Ray and UV/O Data . . . . .	66
4.5.4	Spectral Energy Distribution and Modeling . . . . .	67
4.5.5	Constraints on the EBL from the energy spectrum of 1ES 0347-121 . . . . .	69
4.5.5.1	Limits on the EBL I - <i>H.E.S.S. Nature paper</i> technique . . . . .	69
4.5.5.2	Limits on the EBL II - <i>EBL Scan</i> method . . . . .	71
4.6	Summary and Conclusions . . . . .	72
<b>5</b>	<b>Discovery of VHE <math>\gamma</math>-ray Emission from the Direction of Star Cluster Westerlund 2</b>	<b>75</b>
5.1	Introduction . . . . .	75
5.2	VHE $\gamma$ -rays from Young Open Stellar Clusters . . . . .	75
5.2.1	Young Massive Stars and Stellar Winds . . . . .	75
5.2.2	Stellar Winds and VHE $\gamma$ -rays . . . . .	76
5.3	The Westerlund 2 Region . . . . .	77
5.4	H.E.S.S. Observations of the Westerlund 2 Region . . . . .	80
5.5	Interpretation of the extended VHE $\gamma$ -ray Signal from Westerlund 2 . . . . .	82
5.5.1	Summary & Outlook . . . . .	87
<b>6</b>	<b>Summary and Outlook</b>	<b>89</b>
<b>A</b>	<b>Energy Estimation and Spectral Analysis</b>	<b>91</b>
A.1	Energy Estimation . . . . .	91
A.2	Spectral Analysis . . . . .	93
<b>B</b>	<b>Likelihood Ratio Test</b>	<b>97</b>
<b>C</b>	<b>Collaboration Authors Lists</b>	<b>99</b>
C.1	H.E.S.S. Collaboration . . . . .	99
C.2	HEGRA Collaboration . . . . .	99
C.3	MAGIC Collaboration . . . . .	100
	<b>Bibliography</b>	<b>101</b>

# Chapter 1

## Introduction

Astronomy is one of the oldest scientific disciplines of humanity. While for thousands of years the astronomical observations were confined to a small range of the electro-magnetic spectrum visible to the human eye, astronomical observations today span over a wide range in wavelength: from radio frequencies with wavelengths in the order of several meters to kilometers down to  $\gamma$ -rays with wavelengths less than  $10^{-11}$  m (Fig. 1.1). Every wavelength interval requires its own method of observation: Optical observations are carried out with giant mirrors focusing the light onto photon detectors (the human eye, photographic plates and today mainly semi-conductor detectors). For radio observations giant antennas and systems of several antennas are used. Optical and radio observations can be carried out from the Earth's surface, since the atmosphere is transparent for electro-magnetic radiation in these wavelength bands. For observations in other wavelength regimes e.g. in x-rays, one has to go above the atmosphere and utilize satellite borne instruments.<sup>1</sup>

The wavelength region considered in this work is the very-high-energy (VHE) end of the electro-magnetic spectrum characterized by wavelengths approx.  $10^{-18}$  m and energies  $\sim 1$  TeV =  $10^{12}$  eV =  $1.602176 \times 10^{-7}$  J.<sup>2</sup> The Earth's atmosphere is opaque to VHE  $\gamma$ -rays, so for direct observation satellite based detectors have to be utilized. In the GeV region (1 GeV =  $10^9$  eV) satellite experiments have been very successful. A common property of the photon spectra at these high energies is that the flux decreases very rapidly as the energy increases, so large detection areas are needed. Satellites have only small detection areas limited by the size of the instrument, which in turn is limited by the high cost of bringing a satellite of a certain size into space. For energies  $> 10$  GeV satellites with typical detection areas in the order of a few  $\text{m}^2$  do not detect enough photons.

A different approach for the observation of VHE  $\gamma$ -rays is the atmospheric Cherenkov method. Here, the Earth's atmosphere is used as a giant detector (calorimeter). VHE  $\gamma$ -rays interact with the molecules of the atmosphere by producing new particles. These relativistic particle cascades, called air showers, move faster than the speed of light in the atmosphere and lead to the emission of electro-magnetic radiation through a coherent polarization effect. This effect was first discovered by the russian

---

<sup>1</sup>Going above the Earth's atmosphere improves the observation conditions for almost all wavelength regions. Optical observations on the Earth's surface are subject to atmospheric conditions (seeing), which worsen the resolution. Many of the important discoveries of recent years have been made with the Hubble Space Telescope, a satellite based optical to ultraviolet telescope.

<sup>2</sup> $E = hc/\lambda$  with energy  $E$ , wavelength  $\lambda$ , Planck constant  $h$ , and speed of light  $c$ .

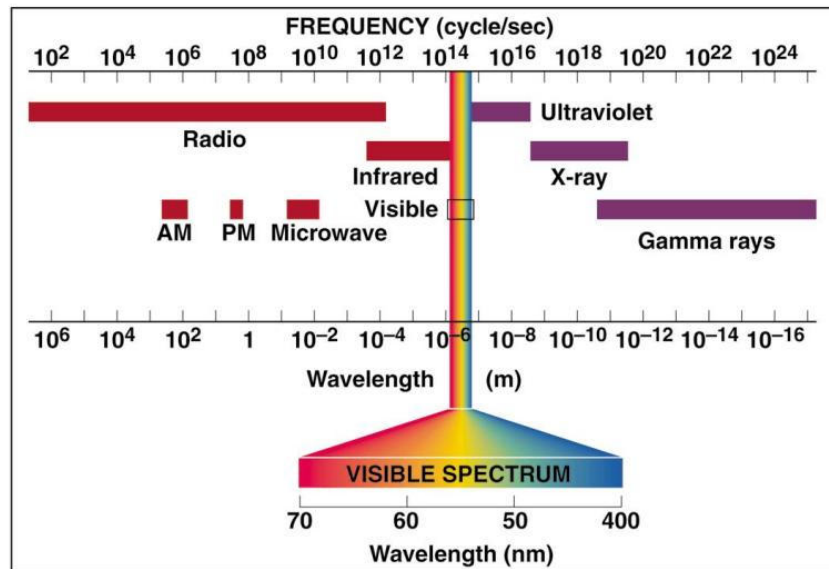


FIGURE 1.1: Electro-magnetic spectrum ranging from radio to  $\gamma$ -rays. The human eye can only detect a tiny fraction of the spectrum in the optical range. (NASA)

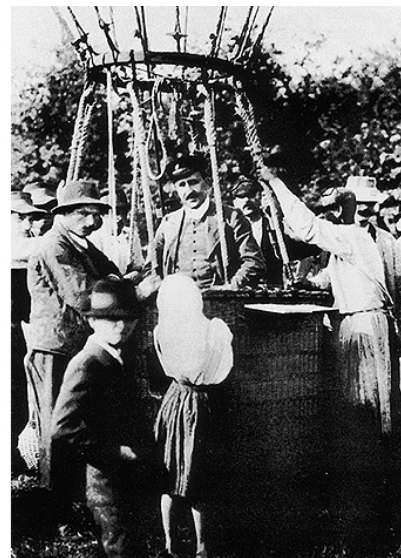


FIGURE 1.2: *Left:* Pavel Alekseyevich Cherenkov (1904 – 1990) was awarded the Nobel Prize in Physics for the discovery of the Cherenkov effect in 1958 (Russian Academy of Sciences). *Right:* Victor Hess (1883 – 1964) received the Nobel Prize in Physics for the discovery of the cosmic rays in 1936.

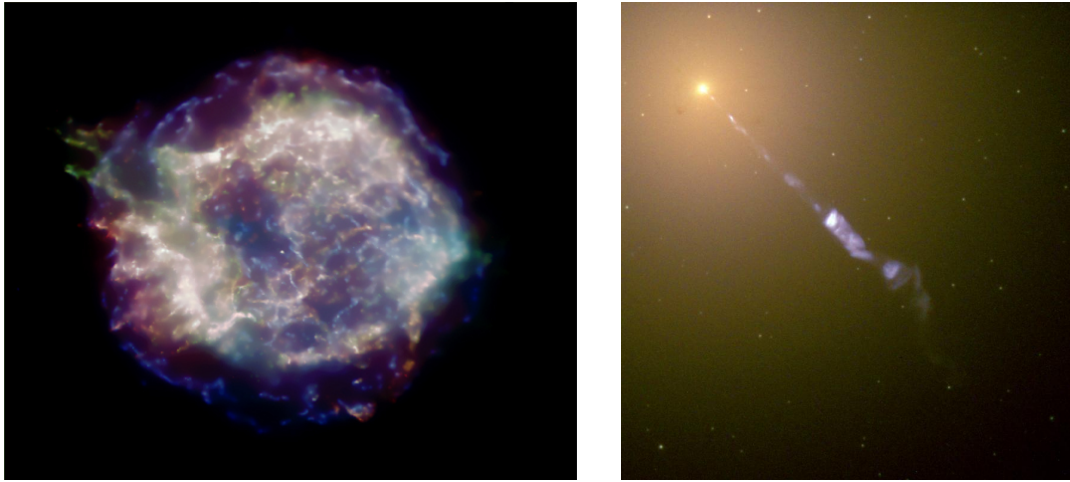


FIGURE 1.3: *Left*: Super nova remnant of shell type Cas A in x-rays measured by the CHANDRA satellite (image width: 8.5"; NASA/CXC/SAO). *Right*: Relativistic particle outflow (jet) of the active galactic nucleus M87 in the optical recorded by the Hubble space telescope. The images shows the bright core (upper left corner) and the jet structure (image width: 31"; NASA and The Hubble Heritage Team (STScI/AURA)).

physicist Pavel Alekseyevich Cherenkov (1904 –1990) (Fig. 1.2 left panel) in nuclear physics experiments. The Cherenkov light flashes from air-showers can be detected on the ground with sensitive photon detectors. The great advantage of this method is the large detection area in the order of  $10^5$ - $10^6$  m<sup>2</sup>. Observations can only be conducted in dark nights at remote locations. Further details on the atmospheric Cherenkov technique are given in Chapter 2, Section 2.4, 2.5, and 2.6.

While most of the optical light is produced in thermal processes by stars emitting Planck's famous black-body radiation, VHE  $\gamma$ -rays are messengers of the non-thermal relativistic universe. To produce VHE  $\gamma$ -rays in thermal processes unrealistically high black body temperatures of  $> 10^{10}$  K would be required. Different processes connected to relativistic particle populations (electrons/protons) and shock phenomena have to be invoked to explain VHE  $\gamma$ -rays. Possible production sites are shocks from the blast waves of exploding stars colliding with the interstellar medium (Fig. 1.3 left panel) or the relativistic particle outflows from super-massive black holes harbored in the cores of other galaxies (shock fronts; Fig. 1.3 right panel). The different production mechanisms for VHE  $\gamma$ -rays are discussed in Chapter 2, Section 2.3.

The H.E.S.S. (High Energy Stereoscopic System) collaboration, named after the discoverer of the cosmic rays Victor Hess (1883 – 1964) (Fig. 1.2 right panel), operates the most sensitive experiment for the observation of VHE  $\gamma$ -rays via the atmospheric Cherenkov technique today (Section 2.7). It is located on the Southern hemisphere in Namibia, Africa.

In this work the discovery of two new sources of VHE  $\gamma$ -rays with the H.E.S.S. Cherenkov telescope array is reported. The extended source HESSJ1023-577 (Chapter 5) coincides with a cluster of young and massive stars. These stars possess strong stellar winds, which ionize the surrounding and can produce relativistic particles through shocks. Processes associated with stellar wind from hot young stars could give a significant contribution to the cosmic ray density for which the origin is still

unclear. The detection of a VHE  $\gamma$ -ray source associated with these sources could be a strong indicator for such a contribution. The second source is associated with the active core of the galaxy 1ES 0347-121 (Chapter 4). Active cores of other galaxies have previously been detected in VHE  $\gamma$ -rays, but the basic physical mechanism producing such VHE  $\gamma$ -rays are not yet fully understood and a large sample of sources is needed to differentiate between different models and other effects (see next paragraph).

Furthermore, the space between galaxies is not empty but filled with diffuse photon fields, the most famous being the cosmic microwave background. VHE  $\gamma$ -rays from distant sources interact with these photon fields on their way to Earth and therefore carry an imprint from these fields. 1ES 0347-121 is the most distant source of VHE  $\gamma$ -rays, which makes it an ideal target for the search for such effects (Section 4.5.5). In Chapter 3 the photon spectra from all known extragalactic sources of VHE  $\gamma$ -rays are used to derive strong limits on the density of the diffuse photon fields.

## Chapter 2

# Imaging Atmospheric Cherenkov Telescopes

### 2.1 Introduction

The origin of charged cosmic rays (CR) is one of the big open questions in the field of astrophysics and one of the primary motivations for the search for very high energy (VHE)  $\gamma$ -rays from the cosmos. In this chapter a (very) brief status of the research on CR is given (Sect. 2.2) and the basic mechanisms for VHE  $\gamma$ -ray production in astrophysical objects are discussed (Sect. 2.3). The principles of the imaging atmospheric Cherenkov technique (IACT) for the detection of VHE  $\gamma$  rays utilizing the Earth's atmosphere as a detector are described (Sect. 2.4 and 2.5) and details on the stereoscopic reconstruction method are presented (Sect. 2.6). Last but not least the H.E.S.S. experiment is introduced (Sect. 2.7) and details on the analysis utilized in this work are presented (Sect. 2.8).

### 2.2 Cosmic Rays

The Earth is constantly bombarded by an isotropic flux of energetic particles from the cosmos called cosmic rays (CRs). The CRs were first discovered in 1912 by Victor Hess (Hess 1912), who showed in his balloon experiments that the ionization in the atmosphere increases with height (Fig. 1.2 right panel). He attributed this to an *ionizing radiation* from outer space. Today the energy spectrum of these particles has been measured over more than 10 decades in energy (Fig. 2.1). The main component of the CRs are protons, but the composition changes with energy (Antoni *et al.* 2005) and there are contributions by heavier elements and from other stable particles. The spectrum roughly follows a power law  $dN/dE \sim E^{-\alpha}$  with a slope  $\alpha \sim 2.7$ . The slope steepens at energies around  $10^{15}$  eV (knee). One explanation for this steepening is that the particles with energies above the knee are no longer confined by the galactic magnetic fields and diffuse out of our Galaxy. Another possible explanation is the charge dependent maximum energy which can be reached by certain acceleration processes e.g. in shocks. This would imply a change in the composition of the CRs beyond the knee, which has already been claimed (Antoni *et al.* 2005). A second change of slope (ankle) occurs at energies  $\sim 10^{18}$  eV. A suppression (sometimes referred to as cut-off) is expected at energies

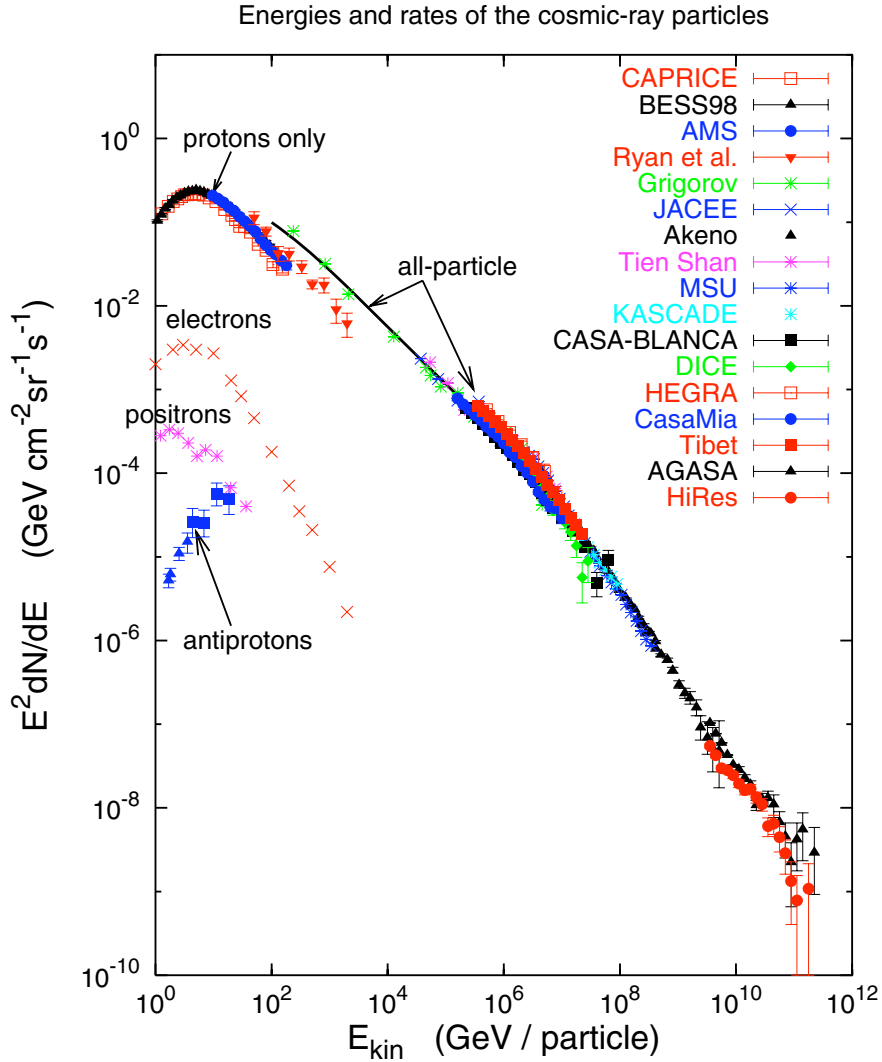


FIGURE 2.1: Differential energy spectrum of the cosmic rays as measured by various experiments (Gaisser 2006).

$> 5 \times 10^{19}$  eV, where the CRs start to interact with the photons of cosmic microwave background (CMB) (Greisen 1966; Zatsepin & Kuz'min 1966).

The origin of the CRs is not yet known. For energies up to the knee a galactic origin is plausible, with supernova remnants (SNR) of shell type being the prime candidates. SNRs seem to have a sufficiently high energy release to power the constant flux and a well known acceleration mechanism (1<sup>st</sup> order Fermi acceleration). Other proposed sources include stellar binaries and the winds of massive stars. For particles with energies exceeding  $10^{18}$  eV an extragalactic origin is likely, since these particles are no longer confined to the galaxy by the galactic magnetic fields. Proposed sources of extragalactic CRs include relativistic jets in active galactic nuclei (AGN), gamma ray bursts and massive star clusters. For a recent brief review of the status and open questions of CR astrophysics see Hillas (2006).

Finding the sources of the CRs has always been a key motivation for very high energy (VHE)  $\gamma$ -ray astronomy. The directional information of charged CRs is scrambled

by the magnetic fields in our galaxy and they arrive isotropically on Earth.<sup>1</sup> At the sites of CR acceleration VHE photons should be produced as secondaries from  $\pi^0$  decays. Since they are not affected by the magnetic fields, they point back to their production site. In 2001 the HEGRA experiment detected VHE  $\gamma$ -rays from the SNR Cassiopeia A (Aharonian *et al.* 2001). The H.E.S.S. experiment detected two more SNRs of shell type and produced for the first time images of the shell morphology in VHE  $\gamma$ -rays (Aharonian *et al.* 2004c, 2005b, 2006a). These detections point towards SNRs as at least one of the sources of the CRs, but some open questions still remain. VHE  $\gamma$ -rays can be produced in alternative scenarios which do not involve hadrons (see section 2.3). Sensitive measurements of the energy spectrum at GeV energies with the upcoming GLAST satellite (Gehrels & Michelson 1999) will help to differentiate between different acceleration mechanisms. A definitive proof for hadronic acceleration in SNR would be the detection of neutrinos from these sources with neutrino telescopes like ICECUBE (Karle *et al.* 2003) or KM3NET (Katz 2006).

## 2.3 Production Mechanism and Sources of VHE $\gamma$ -rays

To produce  $\gamma$ -rays with energies in the GeV to TeV regime sources in thermal equilibrium emitting black body radiation are not sufficient, since unrealistically high temperatures ( $>10^{10}$  K) would be needed. On the other hand, given a relativistic particle population, several well known mechanisms can give rise to VHE photons. They can be divided into two classes, depending on the type of particles that are accelerated:

**Leptonic Accelerators:** Relativistic electrons (positrons) can efficiently produce VHE  $\gamma$ -rays via the inverse Compton (IC) mechanism. The photons can come from *external* photon fields like the thermal radiation from a star or a dust torus or from the cosmic microwave background, or they can be produced by the electrons themselves via synchrotron radiation in a magnetic field. The latter is called the synchrotron self Compton (SSC) mechanism (Ginzburg & Syrovatskii 1969).

**Hadronic Accelerators:** Relativistic protons which interact with ambient matter or photon fields will produce gammas from  $\pi^0$  decays. Given a sufficiently high energy of the primary particles, these photons can reach TeV energies and beyond. Neutrinos are also produced through this kind of interaction mainly via the decay of charged pions. The detection of such high energy neutrinos from astrophysical sources would be a definitive proof for hadronic acceleration. But given their weak interaction, the detection is quite challenging. Another source of VHE photons is the synchrotron radiation from relativistic protons and their secondaries in magnetic fields (Aharonian 2000; Mücke & Protheroe 2001).

The most common mechanism for the production of such relativistic particle populations is the Fermi acceleration (see e.g. Pohl 2002): In shock fronts particles can gain large momentum by crossing the shock repeatedly. The resulting particle energy spectrum follows a power law and can reach very high energies.

There have been numerous astrophysical sources proposed, which could give rise to relativistic particle populations and quite a few of them have been detected in VHE

<sup>1</sup>For extremely high energies  $>10^{18}$  eV the direction of protons is no longer scrambled and they would point back to their origin.

$\gamma$ -rays. In the following paragraphs only a few examples are discussed. Two of the source types, namely active galactic nuclei (AGN) and young open star clusters and their surroundings, are discussed in detail in Chapter 4 and 5 respectively.

**Galactic sources:** As mentioned previously, super-nova remnants (SNR) are natural candidates for VHE  $\gamma$ -ray sources (Drury *et al.* 1994). With SNRs different phenomena are connected: (1) shells, the shock between the ejected outer shell of the super nova (SN) and the surrounding medium. The detection of this source type was an important step towards unveiling the sources of the CRs (Aharonian *et al.* 2004c, 2005b, 2006a). (2) Pulsars and related phenomena. Following a SN explosion a dense neutron star or alternatively a black hole (BH) can form. Fast spinning neutron stars are called pulsars, due to their variable (pulsed) emission. In the vicinity of pulsars electrons and positrons are accelerated, which can lead to VHE  $\gamma$ -ray emission (e.g. Aharonian 2004). The Crab Nebula is the most famous source of this type, but others have been discovered also, especially in the galactic plane scan conducted by the H.E.S.S. experiment (Aharonian *et al.* 2005a, 2006i). Further sources not related to SNR include micro-quasars, x-ray and massive binary system and young open star clusters.

**Extragalactic sources:** Only one type of extragalactic source has been detected until today: the active galactic nuclei (AGN). AGN harbor a massive black hole surrounded by an accretion disk and sometimes a dust torus. The production of VHE  $\gamma$ -rays is most likely linked to relativistic outflows (jets) of these objects. Further possible sources include massive galaxy clusters and galaxies with high star-formation rates (star-burst galaxies). A more detailed discussion of the VHE  $\gamma$ -ray production mechanisms in TeV Blazars, a sub-class of AGNs where a relativistic jet is directed towards the observer, will be given in Chapter 4.

Other source candidates for VHE  $\gamma$ -rays are decay products from dark matter or other relict particles. These so called WIMPS (weakly interacting massive particles) could annihilate and result in VHE photons as primary or secondary particles, if their mass is sufficient. Especially promising is the neutralino particle, which is predicted by the super-symmetric extension of the standard model (e.g. Ellis *et al.* 2003). The detection of a signature of such a particle would be a break-through in search for dark matter and physics beyond the standard model. But given the dominant foreground from other astrophysical processes, to disentangle such a signal is quite challenging and has not yet led to a positive detection (Ripken & et al. 2005; Aharonian *et al.* 2006f; Ripken 2007).

Besides the production mechanisms, attenuation processes for VHE  $\gamma$ -rays have to be considered. The important process of VHE  $\gamma$ -ray attenuation from pair production with low energy photons in the ultraviolet to infrared wavelength region is discussed in Sect. 3.4.

## 2.4 Air Showers

High energetic particles coming from outer space interact with the Earth's atmosphere, accelerating and creating new particles. These particle cascades are called extensive

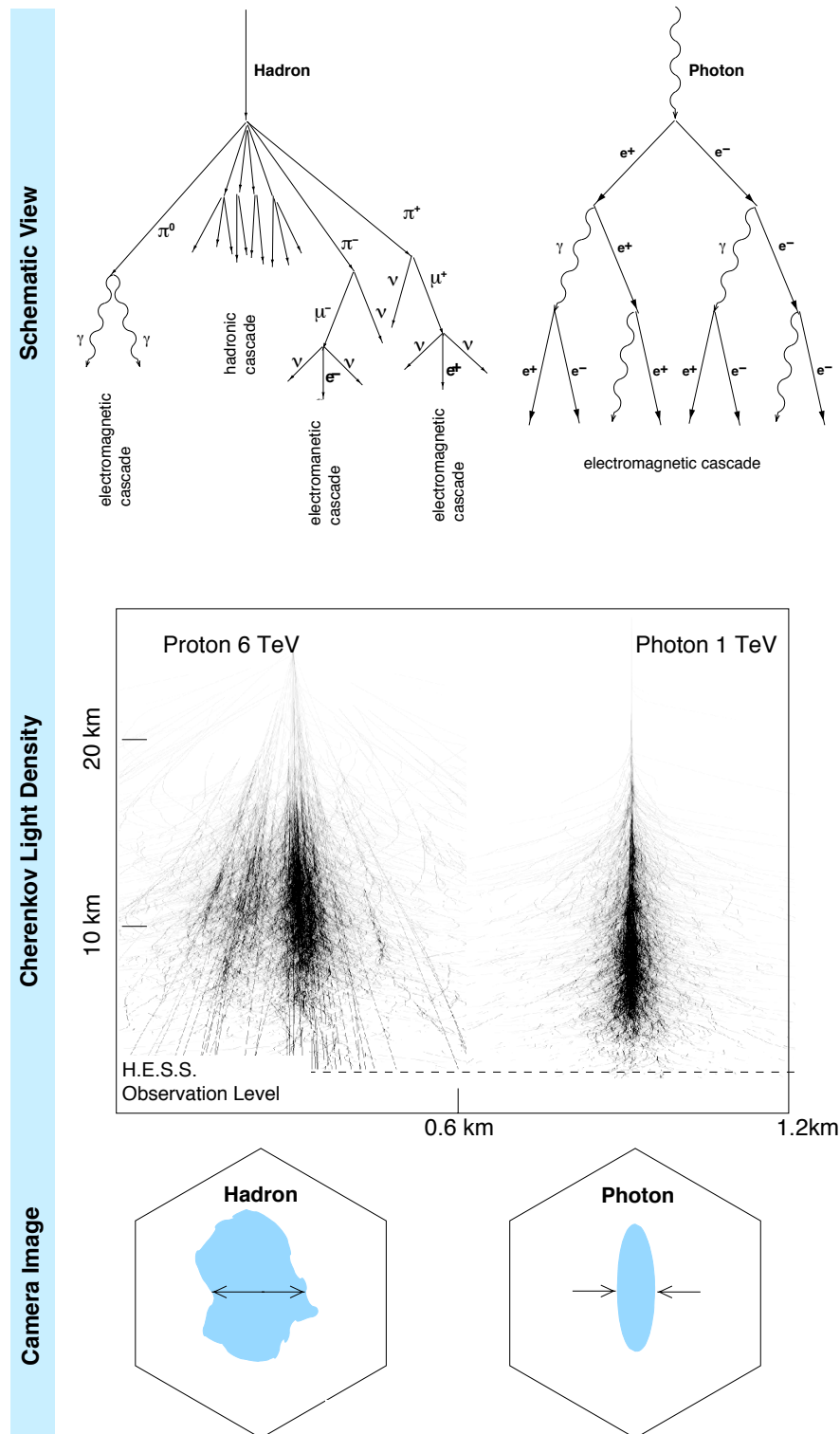


FIGURE 2.2: Extensive air shower. *Upper Panel:* Schematic view of a hadron and a lepton induced air shower. *Middle Panel:* Cherenkov light emissivity from Monte Carlo simulations for an air shower from a proton of energy 6 TeV (left) and a photon of energy 1 TeV (adapted from Horns (2001)). *Lower Panel:* Schematic view of the image of a hadronic (left) and an electro-magnetic (right) shower in a camera of an imaging Cherenkov telescope (adapted from Tluczykont (2003)).

air showers. They come in two flavours: electro-magnetic and hadronic. Electro-magnetic showers are initiated by electrons or photons and mainly evolve through bremsstrahlung and pair creation processes (Fig. 2.2 top left). Hadronic air showers are initiated by hadronic particles and are schematically shown in Fig. 2.2 top right panel. The most likely first interaction is a strong interaction, which produces other hadrons, mainly pions. Pions decay

$$\begin{aligned} \pi^{+/-} &\rightarrow \mu^{+/-} + \nu \\ (\pi^{+/-} &\rightarrow e^{+/-} + \nu, \text{ strongly suppressed}) \\ \pi^0 &\rightarrow \gamma + \gamma \end{aligned}$$

and the produced muons decay into electrons:  $\mu^{+/-} \rightarrow e^{+/-} + 2\nu$ . Due to their high mass (compared to the electron  $m_\mu \approx 200 \cdot m_e$ ) the cross section for shower relevant processes is smaller than for electrons and they are not dominantly involved in the further shower development. The photons and electrons initiate further sub-cascades, if their energy is sufficient.

Cherenkov light is produced, when a particle in a medium moves faster than the speed of light in this medium:  $v > c_0/n$  (e.g. Longair 1992, 1994). The electro-magnetic wavefront is coherently emitted with an angle  $\theta$  to the trajectory of the particle:  $\cos \theta = c/(v \cdot n)$ . The energy spectrum of the emitted Cherenkov light has a  $1/\lambda^2$  dependency ( $\lambda$  =wavelength) and is thus dominated by blue light.

The duration of Cherenkov light flashes from air showers is in the order of a few nano-seconds. The observability of these short Cherenkov flashes depends on the weather and background light characteristics of the atmosphere. Aerosols like clouds or dust can scatter and absorb the light. A bright night sky can make Cherenkov light observations impossible. For optimal detection conditions a dark and remote site with excellent weather conditions is needed.

Air showers from particles with energies in the GeV to TeV domain are compact. Most secondary particles are produced with velocity pointing in the direction of the original particle. The emission angle for Cherenkov light for the particle is typical  $\sim 2^\circ$  which results in a Cherenkov light pool of the shower on the ground with typically diameter  $\sim 100$  m. The Cherenkov light production density from an electro-magnetic shower in comparison to a hadronic shower is shown in Fig. 2.2 middle panel. Please note the factor of  $\sim 20$  in scale between the x and the y-axis. Though still compact the hadronic shower is wider.

## 2.5 Imaging Atmospheric Cherenkov Telescopes

Imaging Atmospheric Cherenkov Telescopes (IACTs) record images of extensive air showers in Cherenkov light. They consist of two main components: (i) the reflector, which collects and focuses the light, and (ii) the camera.

The energy threshold of the telescope is primarily determined by the size of the reflector.<sup>2</sup> For energy thresholds around 500 GeV mirror areas in the order of 10 m<sup>2</sup> are

<sup>2</sup>Less energetic particles produce smaller air showers and therefore less Cherenkov light, so larger light collecting areas are needed. The energy threshold can be lowered further by using photo-multiplier tubes (or photon detectors in general) with high quantum efficiencies and locating the experiment at higher altitudes (i.e. closer to the shower).

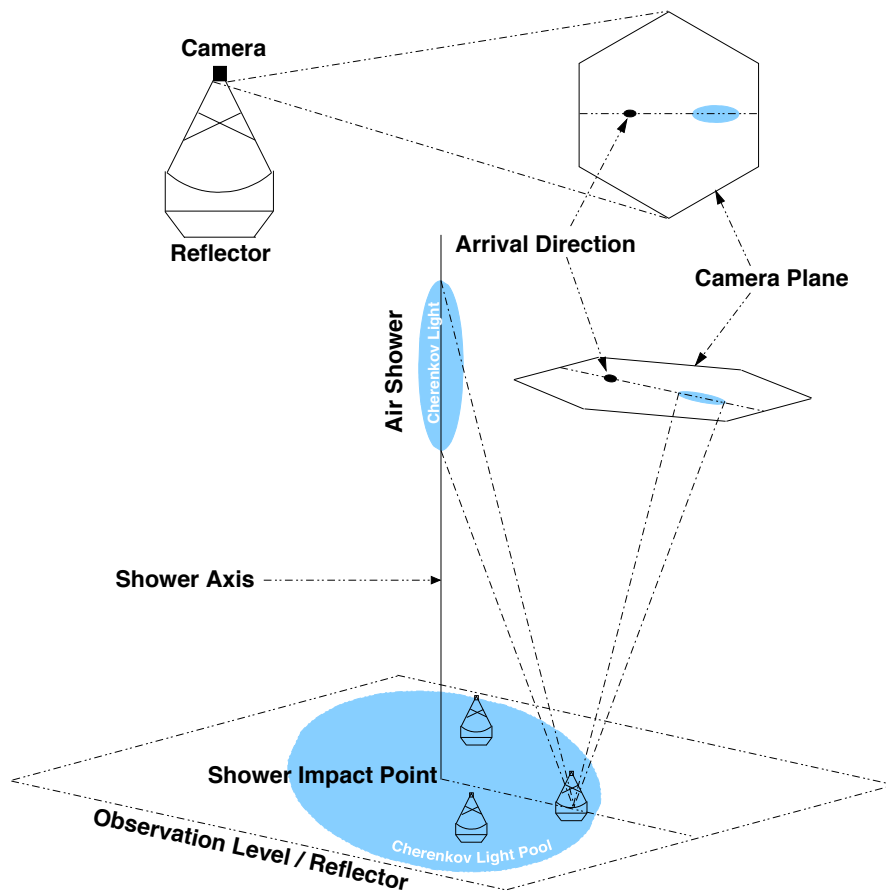


FIGURE 2.3: Detection principle of imaging Cherenkov telescopes (IACT) (adapted from Tluczykont (2003)).

sufficient. For energy thresholds in the order of 100–200 GeV the mirror area has to exceed 100 m<sup>2</sup>. Building large mirrors is difficult and expensive. For IACT the optical requirements are not so demanding, so Cherenkov telescopes generally use reflectors made of smaller individual mirror segments.

The camera is located in the focal plane of the reflector and consists of a number of fast and sensitive photon detectors, for the detection of the short blue Cherenkov light flashes. Photo multiplier tubes (PMTs) are commonly used, but other improved detectors (like hybrid or semiconductor detectors) are under development. The camera is equipped with a topological trigger to suppress random detections e.g. from random air glow (night-sky background, NSB). In principle a single photon detector would be sufficient to detect the Cherenkov light signals (conducting a simple counting experiment), and this technique has been used in the past (see e.g. Weekes (2003) for a short review). But given the dominant background from cosmic rays, airglow etc. no reliable detection of a source of VHE  $\gamma$ -rays has been made.

The imaging technique is based on the idea of recording an image of the Cherenkov light emitted in an air shower. For recording the Cherenkov light an array of PMTs is used. Properties of the primary particle like the arrival direction, energy and particle type can be reconstructed from an image analysis. Through the use this technique

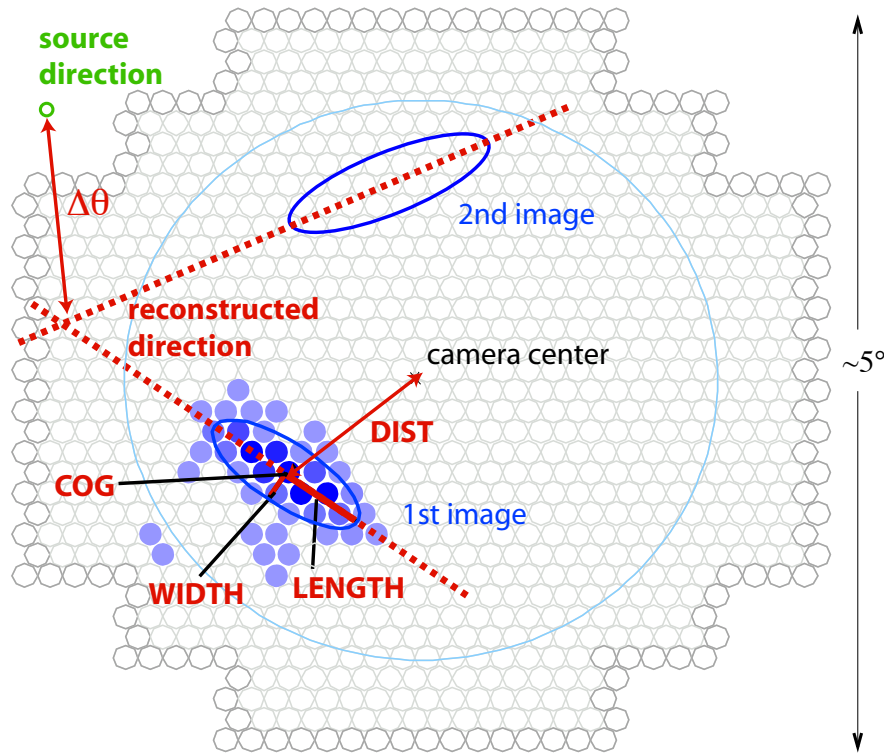


FIGURE 2.4: Cherenkov light image of a shower in the camera with Hillas parameters (adapted from Beilicke (2005)).

the background from hadronic cosmic rays can be greatly reduced. With the imaging technique the first astrophysical source of VHE  $\gamma$ -rays, the Crab Nebula, was detected by the WHIPPLE experiment in 1989 (Weekes 1989).

The Cherenkov image of an electro-magnetic air shower (leptonic particle) has an ellipse shape (see Fig. 2.3).<sup>3</sup> To parameterize the image a set of parameters introduced by Hillas (1985) are utilized (Hillas Parameters). These parameters come from a moment analysis of the pixel intensities and are shown together with an image of a shower in the Cherenkov camera in Fig. 2.4. The distance between the center of gravity (COG) of the image and the camera center is called distance (DIST), the total number of photo electrons detected is the size of the image (SIZE). The main axis of the ellipse points to the direction of the source. Further parameters that are derived are the width (WIDTH) and the length (LENGTH) of the ellipse. Especially the WIDTH has proven to be a powerful parameter for the rejection of background from hadronic showers (see Fig. 2.2 lower panel).

When there is only one image available (single telescope) only the plane of the shower direction is known (dashed lines in Fig. 2.4), not the exact direction. The direction of the source can be estimated with the help of Monte Carlo data (e.g. Ripken (2001)). The same holds for the impact point, which is the intersection between the shower main axis and the plane at the location of the telescopes perpendicular to the observation direction. The distance between impact point and telescopes (impact pa-

<sup>3</sup>One can think of the shower as a glowing pillar (cigar shaped) which becomes an ellipse when projected into a plane.

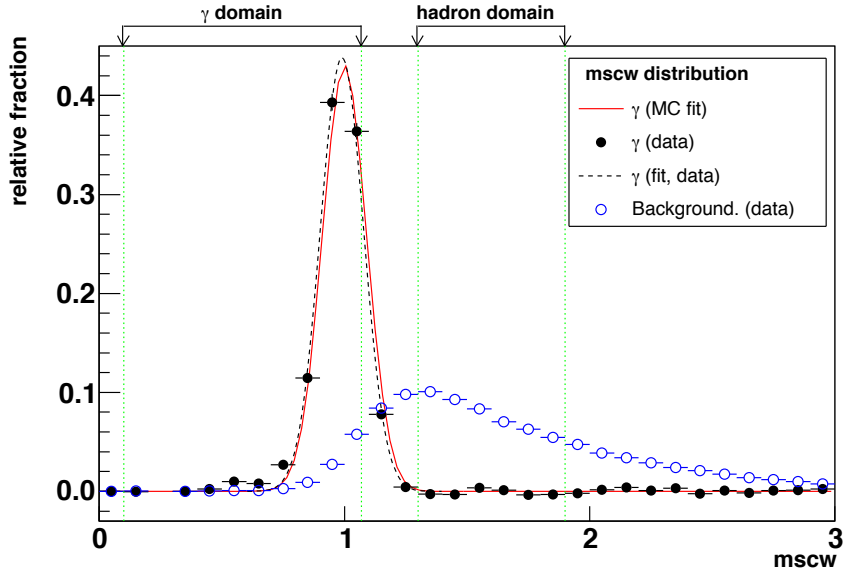


FIGURE 2.5: Normalized distribution of the mean scaled width (MSCW) parameter for photon (black markers, red/black curve) and hadron showers (blue markers) (adapted from Beilicke (2005)).

parameter) is an important parameter used for energy estimation. Both the reconstruction of the direction of origin and the impact point can greatly be improved by using the stereoscopic reconstruction techniques described in the next section.

Most Cherenkov telescopes only operate during moonless nights, but experiments with data taking under partial moon light have also been conducted (e.g. Albert *et al.* 2007d).

## 2.6 Stereoscopic Observations and Reconstruction

The basic principle of stereoscopic observations is to use two or more telescopes to observe the shower *stereoscopically* from different directions. Each telescope records an image of the shower and the information, that can be extracted, is therefore doubled (tripled, etc. depending on the number of telescopes involved). In addition, the direction of origin of the shower can now easily be reconstructed by simply transforming the two (three, etc.) images of the shower into a common coordinate system (see Fig. 2.4). The shower direction is then given by the intersection point of the two main axes (more advanced reconstruction mechanisms are discussed in Hofmann *et al.* (1999); Hofmann *et al.* (2000)). Angular resolutions achieved with this simple method are typically in the order of  $0.1^\circ$  per event. Similar methods can be used to reconstruct the impact point of the shower<sup>4</sup>, which helps to improve the energy reconstruction and background suppression (see below). The parameter used is the impact parameter, which is the distance between the impact point and the telescope.

To conduct stereoscopic observations a central trigger unit is needed, which only

<sup>4</sup>Intersection between the observation plane (plane perpendicular to the observation direction) and the main axis of the shower.

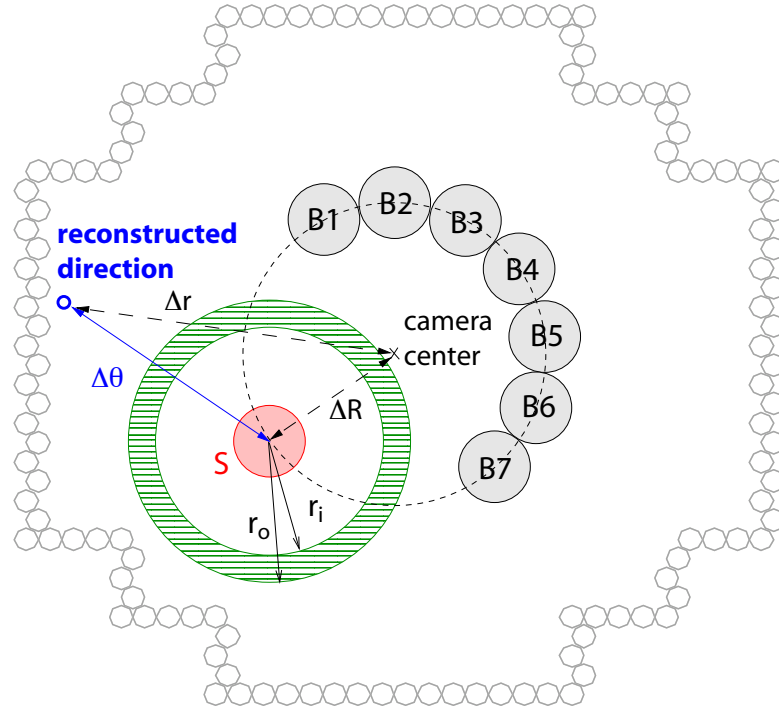


FIGURE 2.6: Background estimation for IACT. Two methods are show: (1) Displacement background (grey circles), where the background is estimated from several background regions located at the same distance from the camera center and with the same size as the signal region (red circle). (2) Ring background (green ring), where the background is estimated using a ring around the signal region (adapted from Beilicke (2005)).

records shower images detected by two or more telescopes. A central trigger also helps to greatly reduce the number of background events triggered by single, local muons. The telescopes should be placed to optimize the effective area for stereoscopic observation. Given that the average light-pool from an air-shower has a diameter  $\sim 100$  m the average distance between the telescopes should be of the same order. The stereoscopic technique has been very successfully pioneered by the HEGRA collaboration (Daum *et al.* 1997) and has consequently been used for the H.E.S.S. experiment (see section 2.7) and all other new IACT instruments.

Cherenkov light from hadronic cosmic ray induced air-showers is the largest source of background for IACTs, for a typical setup over 99.99% of the recorded events. To reduce the number of background events parameters have to be constructed to differentiate between hadronic and leptonic/photonic air-showers. As discussed in section 2.4 the showers from hadronic primaries tend to be wider due to the hadronic interactions. This is reflected in the recorded images, which are in general wider for hadronic induced showers (see Fig. 2.2 bottom panel). The corresponding Hillas parameter is WIDTH. One can now construct the parameter mean scaled width (MSCW) which is given by

$$MSCW = \frac{1}{N} \cdot \sum_{k=1}^N \frac{w_k}{w_{MC}(z, s, i)} \quad (2.1)$$

where  $w_k$  is the WIDTH of image  $k$ ,  $w_{MC}(z, s, i)$  is the expected WIDTH for a photon

shower from Monte Carlo simulation depending on the zenith angle  $z$ , the SIZE  $s$ , and the impact parameter  $i$  of the shower  $k$ , and  $N$  is the number of images. The MSCW distributions for photons (data and Monte Carlo) and hadronic background (data) are shown in Fig. 2.5. The two distributions are well separated and an optimum cut can be found to exclude almost all hadrons by keeping most of the photons. Of course these distributions depend on energy and the overlap between signal and background increases for lower energies ( $<100$  GeV). A similar parameter can be constructed for the LENGTH (MSCL), but the two distributions for signal and background are not as well separated as in the case of the MSCW.

To extract a signal, a region around the source position is chosen (usually a circle). For a point source, the signal region has an optimum size given by the point-spread function (depending on cuts). The size of a circular signal region is given by a cut on the parameter  $\theta^2$ , which denotes the squared angular distance from the source position. To estimate the number of remaining background events in the signal region different background models are used:

**Region background** The background is estimated from several regions with the same shape and size as the signal region (Fig. 2.6 grey circles). The background regions are positioned at the same distance from the camera center as the signal region, which compensates for the acceptance which decreases with distance from the camera center. To utilize this background the telescope has to be pointed with a slight offset (usually  $0.5$  or  $0.7^\circ$ ) to the nominal source position (Wobble mode). Wobble mode is the standard mode for H.E.S.S. observations and the region background is used for signal finding and spectral analysis.

**Ring background** For the ring background a ring around the source region is used (Fig. 2.6 green ring) with an inner radius  $r_i$  and an outer radius  $r_o$ . Events from this background method should be corrected for the acceptance of the camera and zenith angle effects. If the ring area is large enough and background events come from different telescope pointings towards the same field of view many of these effects cancel out and neglecting the correction for the camera acceptance introduces only a small error. The ring background is mainly used to create sky-plots.

**Template background** The template background (Rowell 2003) uses events from the same spatial region as the signal region but from a different domain in the MSCW distribution. The different domains are marked in Fig. 2.5. All events with a  $MSCW > 1.3$  are background events. Since the acceptances over the field of view of the camera for events from the two domains are different, the background events have to be corrected for camera and zenith angle acceptance. The corresponding correction factors can be extracted from the data. The template background method is used for sky-plots and the analysis of extended sources.

For the signal search from source candidates and for spectral reconstruction usually the Region background is used, since no additional corrections e.g. for the camera acceptance are necessary, which could introduce systematic uncertainties. For the discovery of unknown sources through the scan of a region of the sky, two-dimensional sky-plots (skymap) are utilized. An observed region of the sky is divided into a grid and for every grid cell or sky position the number of  $\gamma$ -ray events is calculated. The background



FIGURE 2.7: The four imaging Cherenkov telescopes of the H.E.S.S. experiment.

Field of View (FOV)	$\sim 5^\circ$
Direction Resolution	$0.1^\circ$ per event
Energy Threshold (Zenith)	$\sim 100$ GeV
Energy Resolution	$\sim 15\%$
Sensitivity ( $5\sigma$ in 25 h)	$< 2.0 \cdot 10^{-13} \text{ m}^{-2} \text{ s}^{-1}$

TABLE 2.1: Properties of the H.E.S.S. experiment.

is usually taken from the Ring or the Template background. Two different sky-plots are used: (1) The uncorrelated sky-plot, where the events for a sky position are accumulated over the grid cell. The size of the grid cells should correspond to the size of the point-spread-function of the instrument. (2) The correlated or over-sampled sky-plot. In the correlated sky-plot the number of events for a sky position is accumulated in a circular region around the sky position with a radius  $r$  (oversampling radius) usually taken to be the optimized  $\theta^2$ -cut for signal search. For the search for extended sources larger radii are used ( $0.2^\circ$ ). The number of sky positions to be tested and the locations are usually taken from a dense grid (typical distances between grid points:  $1' - 2'$ ). The individual signals for the sky positions are not independent from each other, since the signal regions for different sky positions overlap. When calculating the significance of an excess in a correlated sky-plot, the number of sky positions tested has to be taken into account as trial factor.

The energy of a shower is correlated with the SIZE parameter of the recorded image and estimated from Monte Carlo simulations. Usually a lookup-table created for steps in zenith angle, azimuth angle and offset in the camera and binned in impact parameter and SIZE is used. In this work a slightly different approach is used which is described in more detail in Appendix A.

## 2.7 The H.E.S.S. Experiment

The H.E.S.S. collaboration operates an array of four identical IACTs located in the Khomas Highland of Namibia at a height of 1800 m above sea level ( $23^\circ 16' 17''$  S  $16^\circ 29' 58''$  E). The telescopes are placed at the corners of a square with side lengths of 100 m. Each telescope has a tessellated reflector of Davies-Cotton (Davies *et al.* 1957) design consisting of 380 circular, quartz-coated glass mirrors with a diameter of 60 cm resulting in a total mirror area of  $107 \text{ m}^2$  (Berndlöhr *et al.* 2003). The individual mirrors can be moved by actuators, allowing for an automated mirror alignment using star light. This method has proven to be extremely successful, resulting in a point spread function well below the size of the camera pixel (Cornils *et al.* 2003; Cornils 2006).



FIGURE 2.8: *Left Panel:* One of the telescopes of the H.E.S.S. experiment. During daytime the telescopes are positioned with the mast pointing towards the ground, so that the camera is parked in the small building on the right side of the image. *Right Panel:* Camera on the mast of a H.E.S.S. telescope. The open lid and the Winston cone plate (light guiding system) are visible. The PMTs are situated behind the Winston cone plate.

The Cherenkov light is recorded with a fast camera consisting of 960 photo-multiplier tubes (PMTs). The size of one pixel (one PMT) is  $0.16^\circ$  resulting in a field of view of about  $5^\circ$ . To increase the light collecting area in the camera plane a light collecting system (Winstan cones) is installed in front of the PMTs. An automated lid protects the camera against daylight. The PMT signal is amplified with two different gains, stored in analogue ring samplers (ARS) and digitized in the camera via ADCs (analogue to digital converter). To trigger the event recording a trigger system with three steps is used. On the level of the single PMT a certain voltage threshold has to be exceeded to set the trigger. On the camera level a sector trigger is used: The PMTs in the camera are grouped into overlapping sectors of 64 PMTs. The camera triggers when more than a minimum number of PMTs in one sector triggers (usually two). These two trigger conditions help to suppress false trigger signals from night-sky background. The third trigger step is on the system level: The cameras send their triggers to a central trigger unit. The event will only be recorded, if two or more telescopes trigger in a certain time interval (Funk *et al.* 2004). With this 'stereoscopic' trigger system the background from single muons can be greatly reduced and it allows for stereoscopic reconstruction of the particle parameters.

The detection system is calibrated performing different calibration runs (Aharonian *et al.* 2004a): The dark current of the PMTs is measured by switching on the high voltage with the camera lid closed. To measure the single photo-electron signal of the PMTs, the camera is illuminated by a very dim light source, which should only produce one to a few photo-electrons. From the signal distribution of these measurements, the single photo-electron signal can be calculated. To measure relative differences between the PMTs, the camera is evenly illuminated by a brighter source (flat-fielding). Single muons produce characteristic ring images, which can be used for an absolute calibration of the optical system including the mirrors and the Wynston cones. Since the central trigger suppresses the muon detection, special runs without the central trigger are performed to collect single muon images.

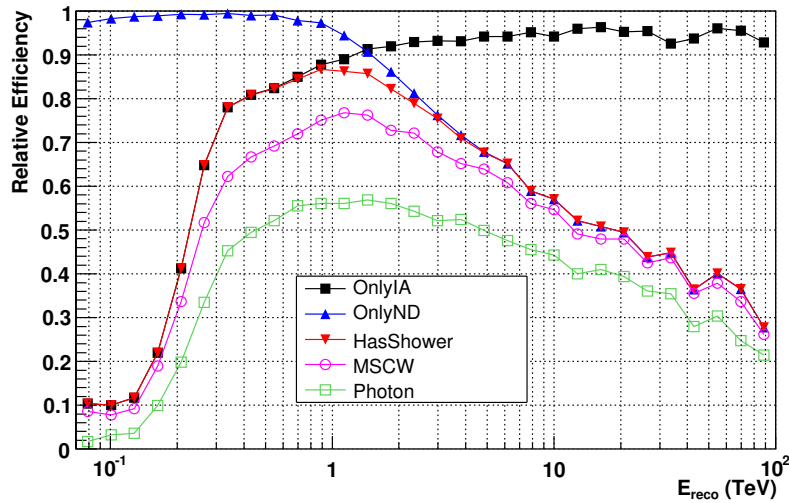


FIGURE 2.9: Effect of different cuts on the efficiency for VHE  $\gamma$ -rays (fraction of Monte Carlo  $\gamma$  events passing the cuts) vs energy (standard cuts,  $20^\circ$  zenith angle,  $0.5^\circ$  offset). *OnlyIA* – IA cut only; *OnlyND* – DIST cut only; *HasShower* – events for which a shower could be reconstructed (after IA and DIST cut); *MSCW* – reconstructed events with MSCW and MSCL cut; *Photon* – cut on  $\theta^2$  in addition to MSCW, final cut for signal; For a Monte Carlo simulation with an energy spectrum of  $dN/dE \sim E^{-2}$  an overall  $\gamma$ -efficiency of 43% is achieved.

To ensure good data quality extensive weather monitoring is performed during data-acquisition involving radiometer measurements in the direction of the telescope pointing, cloud and dust measurements via lidar systems and the recording of basic weather parameters like humidity and temperature.

The data acquisition (DAQ) is largely automatized. A shift crew of two to three persons supervises the data taking, ensures the data quality and takes care of technical problems in collaboration with the corresponding experts during data taking.

With its four telescopes the H.E.S.S. experiment achieves an angular resolution of about 6 arcminutes per detected event and a point source sensitivity above 1 TeV of  $< 2.0 \cdot 10^{-13} \text{ m}^{-2}\text{s}^{-1}$  (1% of the flux from the Crab nebula) for a detection with a statistical significance of 5 standard deviations in a 25 hour observation (Aharonian *et al.* 2006h).

## 2.8 Data Analysis for H.E.S.S.

Data acquisition for H.E.S.S. is organized in time segments of 28 min of length (run). For each event that meets the trigger criteria, the current signals from all PMTs of the triggered cameras are read out and stored on mass storage devices. The signal is usually not sampled in time but integrated over a certain short time period (16 ns).

The current signals are calibrated off-line and result in a number of photo-electrons (p.e.) per PMT. To extract the PMT pixels which contain Cherenkov light from the shower, a so called tail-cut is used: only pixels which have more than  $A_{min}$  p.e. and a neighboring pixel with at least  $A_{neighb}$  p.e. are kept in the image. The choice of the

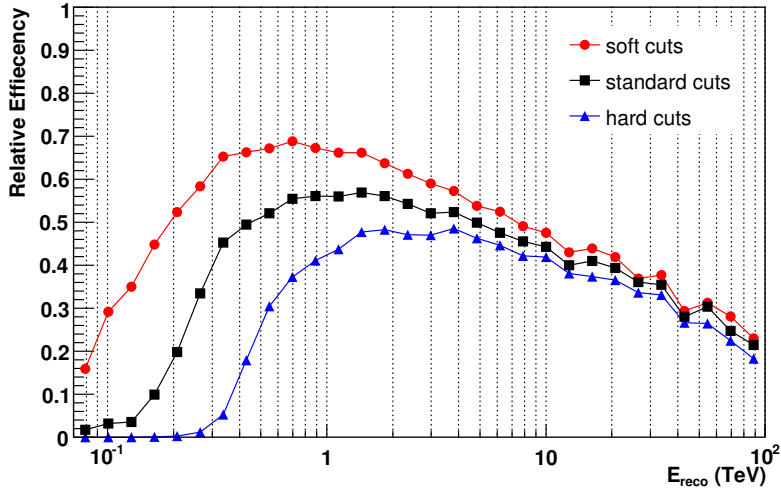


FIGURE 2.10:  $\gamma$ -efficiency for different cuts vs energy. Shown is the *Photon* curve from Fig. 2.9 for standard, hard and soft cuts.

two values affects the energy threshold and the noise remaining in the extracted images from e.g. night-sky background. The standard values used for the tail-cuts are  $A_{min} = 5$  and  $A_{neighb} = 10$ .

The images with the pixels remaining after the tail-cuts are parameterised with the Hillas parameters (as described in Sect. 2.5). Before the reconstruction of the shower parameters certain cuts are used on the single image from every telescope, to ensure that only complete shower images with a certain number of photo-electrons are utilized. Only images passing the following cuts are used to reconstruct the shower parameters.

**Distance (DIST) cut** This cut ensures, that only complete images which are not affected by the edge of the camera are used in the analysis. Images, which are not fully contained in the camera, can lead to a false reconstruction of directions and energies. Usually a value of  $DIST < 2^\circ$  (0.035 rad) is used (light blue circle in Fig. 2.4). Other parameters and corresponding cuts to identify images affected by the edge of the camera are presented in Beilicke (2005).

**Image amplitude (IA) cut** With a cut on the IA, images are selected by their photo-electron statistics. The more p.e. an image has, the better the reconstruction of the shower parameters. On the other hand, the energy of a shower is directly related to the number of p.e.. A high IA cut can increase the energy-threshold. Several IA cuts are used optimized for different source types and purposes (energy reconstruction, sky-plots) ranging from 40 to 200 p.e..

The effects of these cuts on the  $\gamma$ -efficiency, defined as the fraction of Monte Carlo  $\gamma$  events passing the cuts, versus energy is shown in Fig. 2.9.

The Hillas parameters from the remaining images are used to reconstruct the shower parameters direction, impact-parameter, MSCW and MSCL, and the energy as described in Sect. 2.6. The energy estimation and spectral analysis used in this work is discussed in more details in Appendix A. To decrease the number of background

	IA >	MSCW	MSCL	$\theta^2 <$
<b>standard</b>	80 p.e.	0.1– 1.1	0.1 – 1.33	0.015 deg <sup>2</sup>
<b>hard</b>	200 p.e.	0.1 – 1.1	0.1– 1.33	0.01 deg <sup>2</sup>
<b>soft</b>	40 p.e.	0.1– 1.2	0.1 – 1.5	0.02 deg <sup>2</sup>

TABLE 2.2: Cuts on different shower parameters for the standard, hard and soft cut sets. The cut on the DIST for all cut-sets is  $\text{DIST} < 2^\circ$ .

events, cuts on the shower parameters are used. In this work three different sets of cuts are used, which mainly differ in the choice of the IA cut and consequently in the energy threshold. The cut-sets are summarized in Table 2.2.

**Standard cuts** The standard cuts have been optimized on Monte Carlo data assuming a source with a Crab like energy spectrum ( $dN/dE \sim E^{-2.67}$ ) and a flux  $\sim 5\%$  of the Crab Nebula. Real events from a sky region without a source with the same zenith angle are used for the background estimation. The IA cut is  $\text{IA} > 80$  p.e.. This cut set is used for signal search and energy reconstruction.

**Hard cuts** For the hard cuts, the cut on the IA is increased to  $\text{IA} > 200$  p.e., which results in much better reconstruction of the shower parameters. The direction reconstruction is improved, resulting in a better point-spread function, and the separation of the MSCW distributions of signal and background is larger, giving a better background suppression. On the other hand, the energy threshold is raised and sensitivity is lost at the lower energies. This cut is mainly used to produce low background sky-plots.

**Soft cuts** The soft cuts are optimized for high sensitivity at low energies, giving best results for sources with steep spectra. For the IA a cut  $\text{IA} > 40$  p.e. is chosen and the other cuts are optimized for a source with a flux  $\sim 10\%$  of the flux of the Crab Nebula with a steep energy spectrum of  $dN/dE \sim E^{-4}$ .

The  $\gamma$ -efficiency for different sets of cuts are compared in Fig. 2.10.

For different parts of the analysis (cut optimization, energy estimation etc.) Monte Carlo data is needed. Monte Carlo data for the H.E.S.S. experiment is created in two steps: the atmospheric shower and the Cherenkov light produced by the shower are generated with the `CORSIKA` code (Heck *et al.* 1998), the complete detector system incl. mirrors, PMTs and the full electronic chain are simulated with the `sim_hessarray` code (Bernlöhr 2001). The Monte Carlo production chain utilized in this work is described in more detail in e.g. Beilicke (2005).

## Chapter 3

# New Constraints on the Extragalactic Background Light from the Spectra of all known TeV Blazars

### 3.1 Introduction

The space between galaxies is not empty but filled with low density gases and radiation fields. The meta-galactic radiation field (MRF) covers a wide range in wavelength from radio to  $\gamma$ -rays, originating from very different processes (Fig. 3.1). The most prominent and dominant part is the cosmic microwave background (CMB), the decoupled black-body radiation from the last scattering surface ( $z \sim 1000$ ). In the ultraviolet to infrared wavelength regime the MRF contains information about the cosmological star and galaxy formation-history and is commonly referred to as extragalactic background light (EBL). Direct measurements in this wavelength regime, especially in the infrared, are difficult due to dominant foregrounds in the solar system and our galaxy. The observation of VHE  $\gamma$ -rays provides an indirect method of constraining the EBL: VHE photons are attenuated via pair production with the low energy photons of the EBL and the measured VHE spectra receive an *imprint* of the EBL. With assumptions about the VHE  $\gamma$ -ray emission processes in the sources, constraints on the EBL density can be derived from the measured spectra. In this chapter an extensive study of this technique is presented, utilizing the spectra of all known TeV blazars. The work has been conducted in collaboration with Daniel Mazin<sup>1</sup> and has been published in Mazin & Raue (2007).

### 3.2 The Extragalactic Background Light (EBL)

The diffuse extragalactic background light in the ultraviolet (UV) to far-infrared (IR) wavelength regime (EBL) carries important information about the galaxy and star formation history of the universe. The present EBL (redshift  $z = 0$ ) consists of the integrated electromagnetic radiation from all epochs, which is redshifted, corresponding to its formation epoch. In the energy density distribution a two peak structure is commonly expected: a first peak around  $1 \mu\text{m}$  produced by starlight and a second peak

---

<sup>1</sup>Max-Planck-Institut für Physik, Foehringer Ring 6, 80805 Munich, Germany, mazin@mppmu.mpg.de

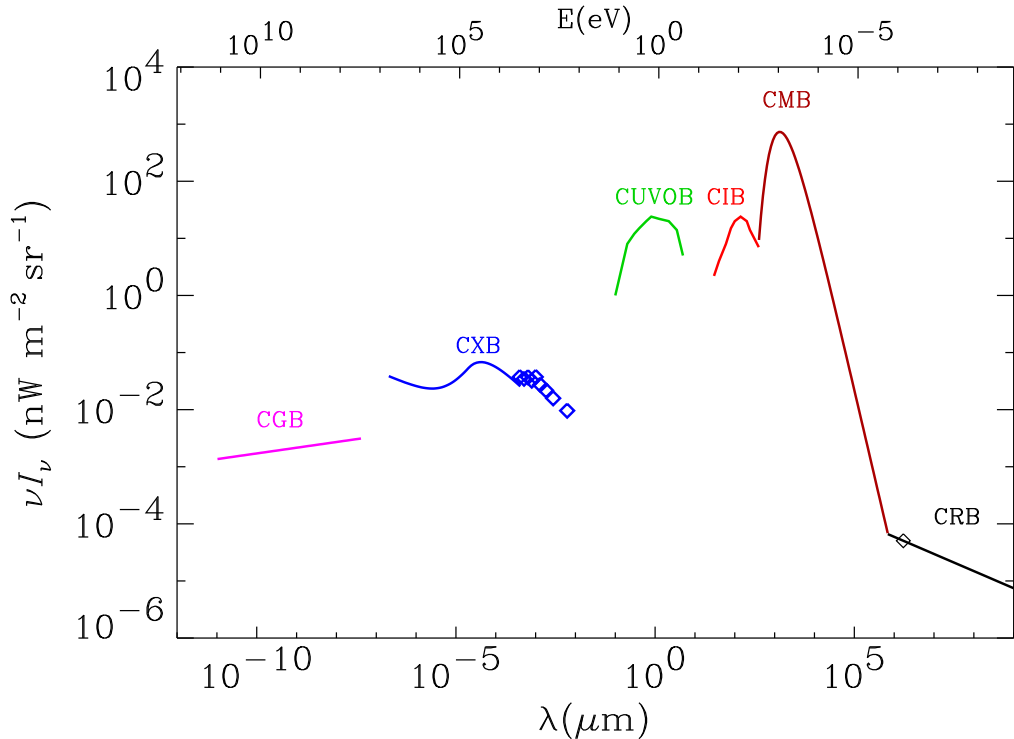


FIGURE 3.1: Spectral energy distribution of the meta-galactic radiation field (MRF) from  $\gamma$ -rays to radio. CGB - cosmic  $\gamma$ -ray background, CXB - cosmic x-ray background, CUVOB - cosmic ultraviolet/optical background, CIB - cosmic infrared background, CMB - cosmic microwave background, CRB - cosmic radio background. (from Hauser & Dwek (2001))

at  $\sim 100 \mu\text{m}$  resulting from starlight that has been absorbed and reemitted by dust in galaxies. Other contributions, like emission from AGN and quasars are expected to produce no more than 5 to 20% of the total EBL density in the mid-IR (see e.g. Matute *et al.* (2006) and references therein).

Solid lower limits for the EBL level are derived from source counts (e.g. Madau & Pozzetti 2000; Fazio *et al.* 2004; Frayer *et al.* 2006) and their extrapolation via stacking (Dole *et al.* 2006). Direct measurements of the EBL have proven to be a difficult task due to dominant foregrounds (e.g. Hauser *et al.* 1998). The various foregrounds in comparison to the residual signal are shown in Fig. 3.2. The dominant foreground is zodiacal light (sunlight reprocessed from interplanetary dust), whose photon energy density is one to two magnitudes higher than the expected photon energy density of the EBL. The spectral energy distribution of the zodiacal light peaks around 10 to 20  $\mu\text{m}$ , making direct detections of the EBL at mid-infrared very unlikely. Furthermore, in the near-infrared galactic sources give a significant contribution to the foreground. Given all these obstacles, it is not expected that the sensitivity of these measurements will greatly improve over the next years. Several upper limits in the infrared wavelength region were reported from direct observations with the DIRBE instrument onboard the Cosmic Background Explorer (COBE) satellite (e.g. Hauser *et al.* 1998) and from fluctuation analyses of the same data (e.g. Kashlinsky & Odenwald 2000). In total, the

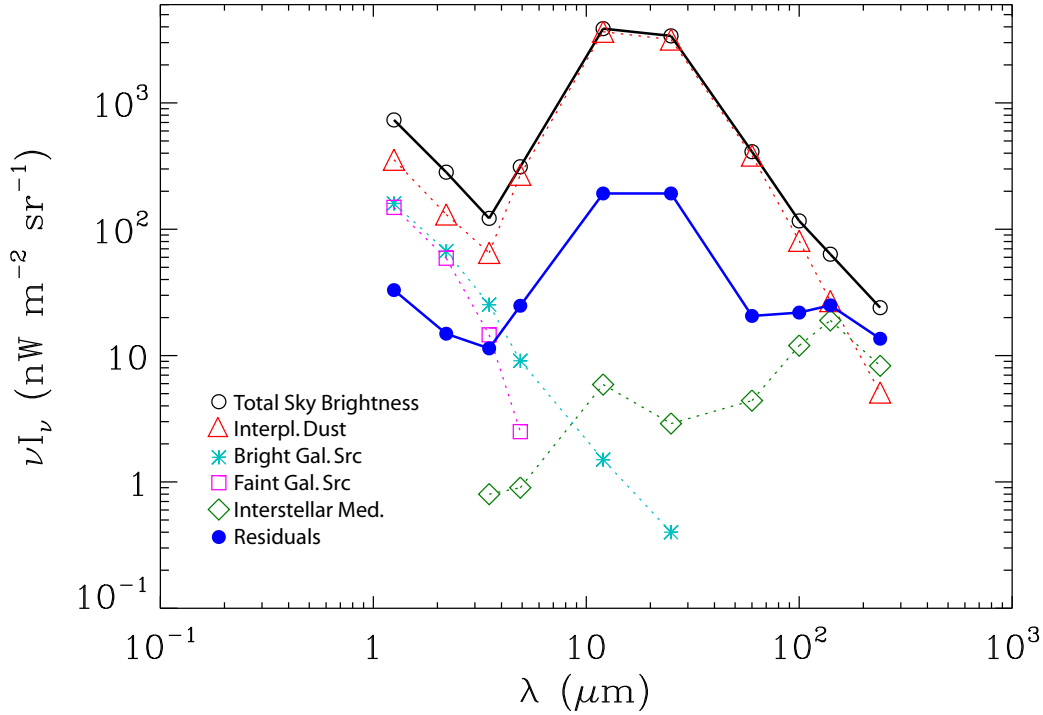


FIGURE 3.2: Spectral energy distribution of various foregrounds for the direct measurement of the EBL. Zodiacal light from interplanetary dust (red open triangles) is the dominant component. The residual emission (all foregrounds subtracted from the total sky brightness) is also given. (from Hauser *et al.* (1998))

collective limits on the EBL between the UV and far-IR confirm the expected two peak structure, although the absolute level of the EBL density remains uncertain by a factor of 2 to 10 (see Fig. 3.3). In addition, several direct detections were also reported, which do not contradict the limits but lie significantly above the lower limits (see Hauser & Dwek (2001) and Kashlinsky (2005) for recent reviews). In particular, a diffuse residual excess in the near-IR (NIR; 1 to 4  $\mu\text{m}$ ) was reported by the IRTS satellite (Matsumoto *et al.* 2005), which is significantly higher than the EBL density expected from galaxy number counts.

The reported excess led to a controversial discussion about its origin. If the excess would be of extragalactic origin (i.e. associated with the EBL), it might be attributed to emissions by the first stars in the history of the universe (Population III) and would make the EBL and its structure a unique probe of the epoch of Population III formation and evolution (Mapelli *et al.* 2004; Kashlinsky *et al.* 2005). Such a luminous Population III star generation, however, over-predicts the number of Ly- $\alpha$  emitters in ultra-deep field searches (Salvaterra & Ferrara 2006) and violates common assumptions on baryon consumption and star formation rates (Dwek *et al.* 2005b). In addition, Dwek *et al.* (2005b) and Matsumoto *et al.* (2005) have pointed out that the NIR excess could be attributed to zodiacal light.

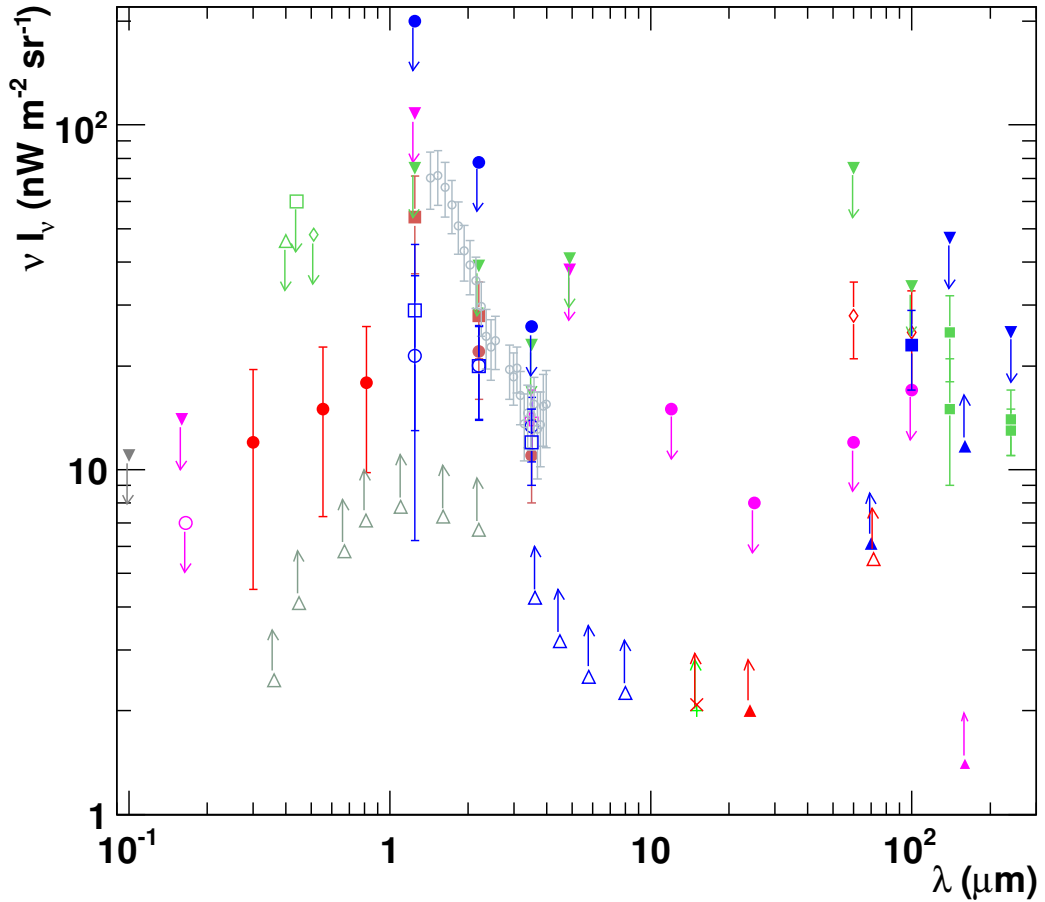


FIGURE 3.3: EBL measurements and limits. Upper limits in the UV to optical: Edelman *et al.* (2000) (grey filled triangle), Martin *et al.* (1991) (open pink circle), Brown *et al.* (2000) (filled pink triangle), Mattila (1990) (open green triangle), Toller (1983) / Leinert *et al.* (1998) (open green square), Dube *et al.* (1979) / Leinert *et al.* (1998) (open green diamond); Tentative detection in the UV/optical: Bernstein *et al.* (2002, 2005) (filled red circle); Lower limits from source counts: Madau & Pozzetti (2000) (open grey triangles), Fazio *et al.* (2004) (open blue triangles), Elbaz *et al.* (2002) (green cross), Metcalfe *et al.* (2003) (red x), Papovich *et al.* (2004) (filled red triangle), Dole *et al.* (2006) (filled pink triangles), Frayer *et al.* (2006) (open red triangle); Detections in the near IR: Dwek & Arendt (1998) (open pink cross), Gorjian *et al.* (2000) (filled brown circle), Wright & Reese (2000) (open blue squares), Cambrésy *et al.* (2001) (filled brown squares), Matsumoto *et al.* (2005) (small open grey circles), Levenson *et al.* (2007) (open blue circles); Upper limits from direct measurements: Hauser *et al.* (1998) (filled green triangles), Dwek & Arendt (1998) (filled pink triangles), Lagache & Puget (2000) (filled blue triangles); Upper limits from fluctuation analysis: Kashlinsky *et al.* (1996) (filled blue circles), Kashlinsky & Odenwald (2000) (filled pink circles); Lower limits from stacking analysis in the far-IR: Dole *et al.* (2006) (blue triangles); Detections in the far-IR: Hauser *et al.* (1998) (filled green squares), Lagache & Puget (2000) (tentative, filled blue square), Finkbeiner *et al.* (2000) (tentative, open red diamonds).

### 3.3 Limiting the EBL with VHE $\gamma$ -ray Observations

A different approach to derive constraints on the EBL (labeled “clever” by Dwek & Slavin (1994)) became available with the detection of very high energy (VHE)  $\gamma$ -rays from distant sources (Punch *et al.* 1992). These VHE  $\gamma$ -rays are attenuated via pair production with low energy photons from the EBL (Gould & Schröder 1967). It was soon realized that the measured spectra can be used to test the transparency of the universe to VHE  $\gamma$ -rays and thus to derive constraints on the EBL density (Fazio & Stecker 1970). With reasonable assumptions about the intrinsic spectrum emitted at the source, limits on the EBL density can be inferred. In a pioneering work conducted by Stecker *et al.* (1996), first limits on the EBL were derived (Stecker & de Jager 1993; de Jager *et al.* 1994). The method is, however, not straightforward. It is in principle not possible to distinguish between source inherent effects (such as absorption in the source, highest particle energies, magnetic field strength etc.) and an imprint of the EBL on a measured VHE spectrum. The emission processes in the detected extragalactic VHE  $\gamma$ -ray emitters<sup>2</sup> are far from being fully understood, which makes it more difficult to use robust assumptions on the shape of the intrinsic spectrum. Different EBL shapes can lead to the same attenuation imprint in the measured spectra, thus a reconstructed attenuation imprint cannot uniquely be identified with one specific EBL shape. A further uncertainty arises due to the unknown evolution of the EBL with time, which becomes more important for distant sources.

Nevertheless, measured VHE  $\gamma$ -ray spectra can provide robust upper limits on the density and spectral distribution of the EBL, if conservative assumptions about the emission mechanisms of  $\gamma$ -rays are considered. A review of the various efforts to detect the EBL or to derive upper limits via the observation of extragalactic VHE  $\gamma$ -ray sources up to the year 2001 can be found in Hauser & Dwek (2001). The measured spectrum of the TeV blazar H 1426+428 at a redshift of  $z = 0.129$  (Aharonian *et al.* 2002a) led to a first tentative detection of an imprint of the EBL in a VHE spectrum (Aharonian *et al.* 2002a, 2003c). Using the H 1426+428 spectrum together with the spectra of previously detected TeV blazars, limits on the EBL were derived (Costamante *et al.* 2003; Kneiske *et al.* 2002). Later, Dwek & Krennrich (2005) utilized a large sample of TeV blazar spectra and solid statistical methods to test a set of EBL shapes on their physical feasibility. EBL shapes were considered forbidden, when, under the most conservative assumptions, the intrinsic spectra showed a significant exponential rise at high energies. Using the VHE spectra of the TeV blazars Mkn 421, Mkn 501, H 1426+428, and PKS 2155-304, Dwek *et al.* (2005a) argued that the claimed NIR excess is very unlikely of extragalactic origin and that an EBL density on the level of the source counts gives a good representation of the intrinsic spectra. Recently, the detections of the two distant TeV blazars H 2356-309 and 1ES 1101-232 by the H.E.S.S. experiment have been used to derive strong limits on the EBL density around  $2 \mu\text{m}$  (Aharonian *et al.* 2006b). The method is based on the hypothesis that the intrinsic TeV blazar spectrum cannot be harder than a theoretical limit and that the spectrum of the EBL follows a certain shape (Primack *et al.* 1999). To derive limits on the EBL density, the shape is scaled until the de-absorbed TeV blazar spectrum meets the exclusion criteria.<sup>3</sup> The derived upper lim-

<sup>2</sup>So far, all but one of the detected extragalactic VHE  $\gamma$ -ray emitters belong to the class of blazars.

<sup>3</sup>A similar technique (scaling of a certain shape until the de-absorbed spectrum reaches an exclusion criteria) was previously used by Guy *et al.* (2000) to derive limits on the EBL from the Mkn 501 spectrum measured by the CAT experiment during a flare in 1997.

its are only a factor of two above the lower limits from the integrated light of resolved galaxies.

In the last 2 to 3 years, many new TeV blazars were discovered and the established ones were remeasured with higher sensitivity with the new Imaging Atmospheric Cherenkov Telescopes (IACT) as H.E.S.S and MAGIC. It is therefore of high interest, whether the new measurements agree with the previous limits on the EBL. Furthermore, to derive limits on the EBL from the data, it is important to scrutinize all available data together to obtain a consistent picture and to maximize the constraints. In this paper we use, therefore, spectra from all TeV blazars to derive upper limits on the EBL density in a wide wavelength range from the optical to far-infrared. Moreover, a common criticism of the EBL limits previously derived from the spectra of TeV blazars is that these limits are obtained by assuming a certain EBL shape and e.g. scaling the overall EBL density, or by exploring just a few model parameters of an EBL model. Since EBL models are complex and different models do not agree in detail, the derived limits become strongly model dependent. In order to avoid this dependency, we developed a novel technique of describing the EBL number density by spline functions, which allows to test a large number of hypothetical EBL shapes. Our aims are:

1. Provide limits on the EBL density, which do not rely on a predefined shape or model, but rather allow for any shape compatible with the current limits from direct measurements and model predictions.
2. Treat all TeV blazar spectra in a consistent way, using simple and generic assumptions about the intrinsic VHE  $\gamma$ -ray spectra and a statistical approach to find exclusion criteria.
3. Use spectral data from all detected TeV blazars to (a) derive upper limits on the EBL density from the individual spectra and then (b) combine these results into a single robust limit on the EBL density for a wide wavelength range.

Throughout this study we adopt a Hubble constant of  $H_0 = 72 \text{ km s}^{-1} \text{ Mpc}^{-1}$  and a flat universe cosmology with a matter density normalized to the critical density of  $\Omega_m = 0.3$  and  $\Omega_\lambda = 0.7$ .

### 3.4 VHE $\gamma$ -ray Attenuation from the Extragalactic Background Light

VHE  $\gamma$ -rays traversing the extragalactic radiation fields are attenuated via pair production with the low energy photons of the EBL. The optical depth for a VHE  $\gamma$ -ray for this process can be calculated as following (e.g. Mazin (2003)): The cross section for the  $\gamma \gamma \rightarrow e^+ e^-$  interaction of a  $\gamma$ -ray photon of energy  $E_\gamma$  with a background photon of energy  $\epsilon$  is given by (e.g. Heitler 1960)

$$\begin{aligned} \sigma_{\gamma\gamma}(E_\gamma, \epsilon, \mu) &= \frac{3\sigma_T}{16} (1 - \beta^2) \left[ 2\beta(\beta^2 - 2) + (3 - \beta^4) \ln \left( \frac{1 + \beta}{1 - \beta} \right) \right] \quad (3.1) \\ \beta &\equiv \sqrt{1 - \frac{\epsilon_{th}}{\epsilon}} \\ \epsilon_{th}(E_\gamma, \mu) &= \frac{2(m_e c^2)^2}{E_\gamma(1 - \mu)} \end{aligned}$$

where  $\sigma_T = 6.65 \times 10^{-25} \text{ cm}^2$  is the Thompson cross section,  $\epsilon_{th}$  the threshold energy of the interaction, and  $\mu \equiv \cos \theta$ , where  $\theta$  is the angle between the incident photons. The  $\gamma$ - $\gamma$  cross section for the interaction with an isotropic distribution of background photons has a pronounced peak value of  $1.70 \times 10^{-25} \text{ cm}^2$  (for  $\beta = 0.70$ ) near the threshold of the reaction. This corresponds to energies for which the product  $E_\gamma \epsilon \approx 4(m_e c^2)^2 \approx 1 \text{ MeV}^2$ , or  $\lambda_\epsilon (\mu\text{m}) \approx 1.24 E_\gamma (\text{TeV})$ , where  $\lambda_\epsilon$  is the wavelength of the background photon. Therefore the attenuation at different TeV energies tests different wavelengths of the EBL.

The optical depth traversed by a photon observed at energy  $E_\gamma$  that was emitted by a source at redshift  $z$  is given by:

$$\tau_\gamma(E_\gamma, z) = \int_0^z \left( \frac{d\ell}{dz'} \right) dz' \int_{-1}^{+1} d\mu \frac{1-\mu}{2} \int_{\epsilon'_{th}}^{\infty} d\epsilon' n_\epsilon(\epsilon', z') \sigma_{\gamma\gamma}(E'_\gamma, \epsilon', \mu) \quad (3.2)$$

where  $n_\epsilon(\epsilon', z') d\epsilon'$  is the comoving number density of EBL photons with energies between  $\epsilon'$  and  $\epsilon' + d\epsilon'$  at redshift  $z'$ ,  $\epsilon'_{th} = \epsilon_{th}(E'_\gamma, \mu)$ ,  $E'_\gamma = E_\gamma(1+z')$ , and where  $d\ell/dz$ , is given by (e.g. Peacock 1999):

$$\left( \frac{d\ell}{dz} \right) = c \left( \frac{dt}{dz} \right) = \frac{R_H}{(1+z)E(z)} \quad (3.3)$$

$$E(z) \equiv \left\{ (1+z)^2(\Omega_m z + 1) + z(2+z)[(1+z)^2\Omega_r - \Omega_\Lambda] \right\}^{1/2},$$

where  $\Omega_m$  and  $\Omega_r$  are, respectively, the matter and radiation energy density normalized to the critical density,  $\Omega_\Lambda = \Lambda/3H_0^2$  is the dimensionless cosmological constant ( $\Omega_m + \Omega_r + \Omega_\Lambda = 1$  in a flat universe),  $R_H \equiv c/H_0$  is the Hubble radius,  $c$  is the speed of light, and  $H_0$  is the Hubble constant. The comoving number density of EBL photons  $n_\epsilon(\epsilon, z)$  of energy  $\epsilon$  at redshift  $z$  is given by:

$$\begin{aligned} \epsilon^2 n_\epsilon(\epsilon, z) &= \left( \frac{4\pi}{c} \right) \nu I_\nu(\nu, z) \\ &= \int_z^\infty \nu' \mathcal{L}_\nu(\nu', z') \left| \frac{dt}{dz'} \right| \frac{dz'}{1+z'} \end{aligned} \quad (3.4)$$

where  $\epsilon = h\nu$ ,  $\nu' = \nu(1+z')$ , and  $\mathcal{L}_\nu(\nu', z')$  is the specific comoving luminosity density at frequency  $\nu'$  and redshift  $z'$ .

In this study, the EBL photon density  $n_\epsilon(\epsilon, z)$  is not calculated via integration over the luminosity density, but a certain spectral EBL shape is assumed, which does not have a redshift dependence. The construction of the EBL shapes and the consequences of this method are further discussed in the following Section.

### 3.5 Grid Scan with Spline Function

To calculate the optical depth  $\tau_\gamma$  for a VHE- $\gamma$  ray with energy  $E_\gamma$ , emitted at a redshift  $z$ , and for one specific shape of the EBL, one needs to solve the three-fold integral given in Equation 3.2. For the large number of shapes ( $\sim 8$  million) we will analyze, a full numerical integration would require an extensive amount of computing power. To

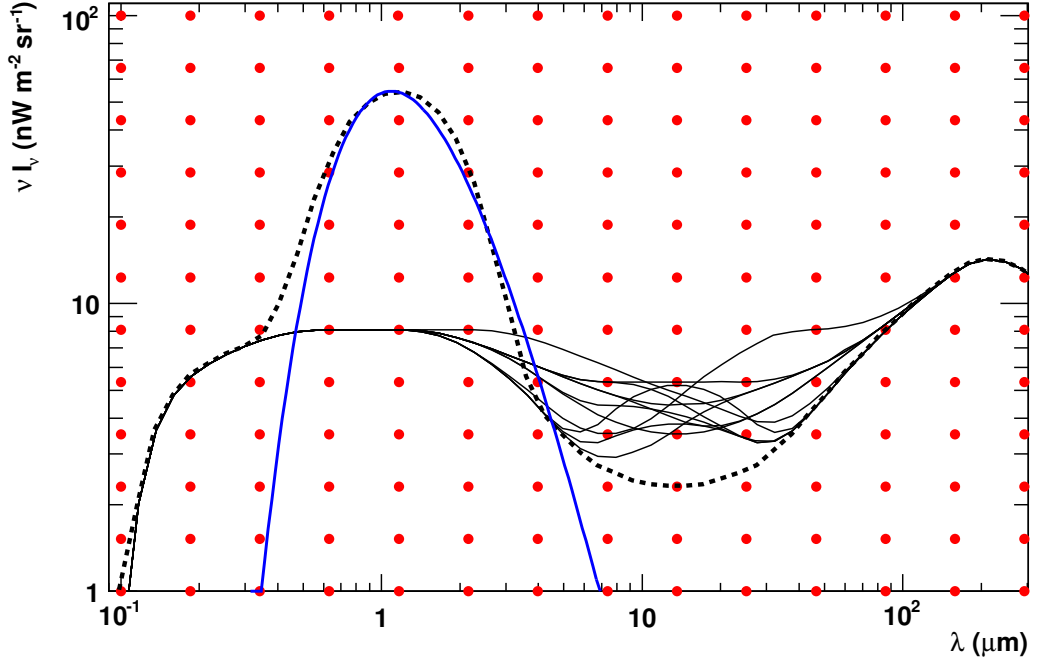


FIGURE 3.4: Examples for spline shapes resulting from the grid layout, overlaid on the grid points (filled circles). The dashed black line illustrates the thinnest structure that can be achieved with our grid setup. A Planck spectrum (blue line) is given for comparison. Further examples for shapes are given as solid black lines.

avoid this problem, we parameterize the EBL number density at redshift  $z = 0$  as a spline<sup>4</sup>

$$n_{\epsilon}(\epsilon, 0) = \sum_{i=0}^k w_i s_{i,p}(\epsilon) \quad (3.5)$$

with base functions

$$s_{i,0}(\epsilon) = \begin{cases} 1 & \text{if } \epsilon_i \leq \epsilon < \epsilon_{i+1} \text{ and } \epsilon_i < \epsilon_{i+1} \\ 0 & \text{otherwise} \end{cases} \quad (3.6)$$

$$s_{i,p}(\epsilon) = \frac{\epsilon - \epsilon_i}{\epsilon_{i+p} - \epsilon_i} s_{i,p-1}(\epsilon) + \frac{\epsilon_{i+p+1} - \epsilon}{\epsilon_{i+p+1} - \epsilon_{i+1}} s_{i+1,p-1}(\epsilon).$$

$w_1, \dots, w_k$  are weights controlling the shape of the curve,  $p$  is the order of the spline and is set to  $p = 3$  throughout the paper,  $k$  is the number of supporting points, and  $\epsilon_1, \dots, \epsilon_k$  are the positions of the supporting points.

One can now insert the spline parameterization for the EBL from Equation (3.5) into the calculation of the optical depth (Equation (3.2)) and then swap the integration and the spline summation part. The optical depth for one base function  $\tau_i(E_{\gamma}, z)$  can then

<sup>4</sup>A way to visualize this spline is the following: A number of Gaussian like base functions are added to result in a smooth curve, whereby the base functions can be weighted ( $w_i$ ) to achieve different overall shapes. These base functions are characterized by the position of the peak and a certain width, which depends on the order  $p$  and the spacing of the supporting points.

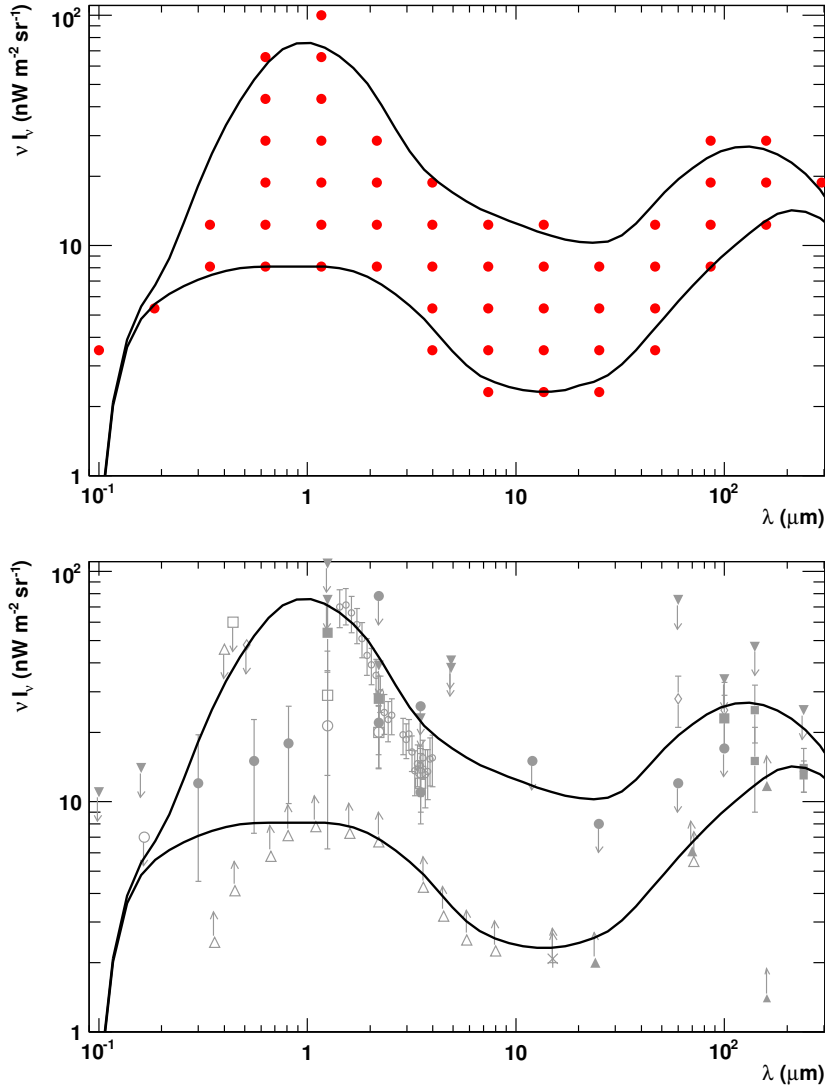


FIGURE 3.5: *Top*: Grid points (red filled circles) and minimum and maximum shape of the scan. *Bottom*: Minimum and maximum shape overlaid on the EBL measurements from Fig. 3.3

be calculated easily. The total optical depth is given by a simple summation over the optical depths of the base functions (already integrated), weighted with the weights  $w_i$ :

$$\tau(E_\gamma, z) = \sum_{i=0}^k w_i \tau_i(E_\gamma, z) \quad (3.7)$$

The choice of the weights  $w_i$  controls the shape of the EBL, so the EBL shape can be changed after the integration.

The generic spline shapes do not have a redshift dependency, thus an evolution of the EBL cannot be taken into account. We assume a constant photon number density, only expanding and shifting in wavelength with expansion of the universe:

$$n_\epsilon(\epsilon, z) = n_\epsilon(\epsilon/(z+1), 0) \cdot (z+1)^3 \quad (3.8)$$

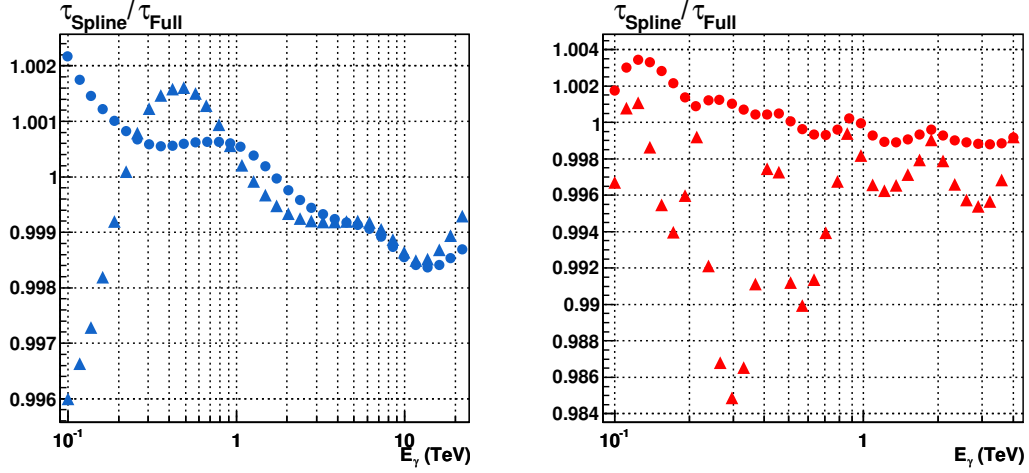


FIGURE 3.6: Comparison of the optical depth from spline summation  $\tau_{\text{Spline}}$  vs the optical depth from full numerical integration over the curve  $\tau_{\text{Full}}$ . *Left:*  $\tau_{\text{Spline}}/\tau_{\text{Full}}$  for Mkn 501 for the minimum (circles) and maximum (triangles) shapes in the scan. *Right:*  $\tau_{\text{Spline}}/\tau_{\text{Full}}$  for 1ES 1101-232 for the minimum (circles) and maximum (triangles) shapes in the scan.

Neglecting the evolution of the EBL is a valid assumption for nearby sources (e.g. Mkn 501), but for distant sources<sup>5</sup> this can result in an additional error on the upper limits in the order of 10 to 20% depending on the evolution model and redshift (see e.g. Aharonian *et al.* (2006b)). The systematic error arising from this assumption is further discussed in Sect. 3.10.

In order to estimate the numerical uncertainties arising from the integration of the base functions, the result for  $\tau_\gamma$  from the summation is compared to the results from a full integration over the actual EBL shapes (only one integration) for several shapes and spectra used in this study. The deviation for almost all settings is found to be less than 0.5%. Even for extreme cases (high redshift, high EBL density) the deviation is always less than 2% (see Fig. 3.6 for results from Mkn 501 and 1ES 1101-232). These small deviations arise from inaccuracies in the numerical integration of the base functions.

The EBL spline shapes that we will examine in this study, are constructed from a grid in EBL energy density vs wavelength: the x-positions of the grid points (wavelength) are used as positions for the supporting points  $\epsilon_i$  of the spline. The y-positions of the grid points (energy density) are used as weights  $w_i$ .

For the supporting points (x-axis of the grid)  $\epsilon_i$  we use 16 equidistant points in  $\log_{10}(\lambda)$  ( $\lambda = hc/\epsilon$ ) from 0.1 to 1000  $\mu\text{m}$ . The number and distance of the supporting points together with the order of the spline determines the width of the structures, that can be described with the spline. Given the grid setup and the spline of order  $p = 3$ , the thinnest peak or dip that can be modeled is about three grid points wide (FWHM, Fig. 3.4 shape with dashed line). This minimum width is similar to a Planck spectrum from a black body radiation (blue line in Fig. 3.4). Noteworthy, extremely sharp and strong cut-offs or bumps can only be described in an approximate way. Such features could arise from the Lyman- $\alpha$  drop-off of massive Population III stars in certain models (e.g. Salvaterra & Ferrara 2003), but they are generally not expected on larger

<sup>5</sup>The most distant source considered in this study, 1ES 1101-232, has a redshift of  $z = 0.186$ .

wavelength scales, since they would be smoothed out by redshift. Mainly, the EBL originates from an overlap of the redshifted spectra of single stars and dust reemission, the resulting spectral form of which is similar to or broader than a Planck spectrum.

The upper limits derived in this study depend on the width of the structures modeled, and the choice of the minimum width has to be physically motivated, as it is in our case. The dependency of the limits on the choice of the grid setup is discussed in more detail in Section 3.10.

The weight  $w_i$  of the spline (y-axis of the grid) are varied in 12 equidistant steps in  $\log_{10}(\text{energy density})$  from 0.1 to  $100 \text{ nW m}^{-2} \text{ sr}^{-1}$ . Since we apply the grid point positions directly as weights  $w_i$ , the resulting curve does not directly go through the grid points. So for all limits etc. the actual curve has to be considered and not the grid point positions. Our usage of the grid point positions as weights also results in several shapes lying between two grid points. This is illustrated in Fig. 3.4 for two arbitrarily chosen grid points between 10 and  $20 \mu\text{m}$ .

For the scan a subset of grid points is selected such that all resulting shapes are within the limits given by the galaxy counts on the lower end and the limits from the direct measurements and the fluctuation analyses on the upper end. In the 20 to  $100 \mu\text{m}$  regime we choose a hugher shape, given the wider spread of the (tentative) measurements. The final grid is shown in Fig. 3.5 as red filled circles. By iterating over all grid points we obtain 8 064 000 different EBL shapes, which will be examined.

For a given optical depth  $\tau_\gamma(E_\gamma, z)$  one can determine the intrinsic differential energy spectrum of a source using:

$$dN/dE_{\text{intr.}} = dN/dE_{\text{obs}} \times \exp[\tau_\gamma(E_\gamma, z)], \quad (3.9)$$

where  $dN/dE_{\text{obs}}$  is the observed spectrum. The intrinsic spectrum is then tested for its physical feasibility as described in Section 3.7. This process is repeated for all VHE  $\gamma$ -ray sources (described in the next section) and for all 8 064 000 EBL shapes.

### 3.6 TeV Blazar Spectra

Since the detection of the first extragalactic VHE  $\gamma$ -ray source in 1992 (Punch *et al.* 1992), a wealth of new data has become available. Up to now all extragalactic VHE  $\gamma$ -ray sources belong to the class of active galactic nuclei (AGN), and, with the only exception of the radio galaxy M87 (Aharonian *et al.* 2003b, 2006e), to the subclass of TeV blazars. AGNs are known to be highly variable sources, with variations of the absolute flux levels in the TeV range by more than an order of magnitude and in time scales as short as 15 min (e.g. Gaidos *et al.* 1996; Aharonian *et al.* 2002b). Changes of the spectral shapes are also observed (e.g. Krennrich *et al.* 2002; Aharonian *et al.* 2002b).

In this study we utilize spectral data obtained during the last seven years by four different experimental groups operating ground-based imaging atmospheric Cherenkov telescopes (IACTs): Whipple (Finley & The VERITAS Collaboration 2001), HEGRA (Daum *et al.* 1997), H.E.S.S. (Hinton 2004) and MAGIC (Cortina *et al.* 2005). We select at least one spectrum for every extragalactic source with known redshift. If there is more than one measurement with a comparable energy range, we take the spectrum with the better statistics and the harder spectrum (expected to give stronger constraints, see Section 3.7). If different measurements of one source cover different energy ranges, we include both spectra as independent tests. Another possibility would

TABLE 3.1: TeV blazar spectra used in this paper. In case the measured spectrum can be well described by a simple power law  $dN/dE \propto E^{-\Gamma}$ , only the slope  $\Gamma$  is quoted. Otherwise the cut-off energy  $E_{\text{cutoff}}$  according to  $dN/dE \propto E^{-\Gamma} \exp(-E/E_{\text{cutoff}})$  is also quoted. If no systematic error on the photon index is given in the corresponding publication, we use a value of 0.2 (values in brackets).

Source	Redshift $z$	Experiment	Energy range (TeV)	Slope $\Gamma \pm \sigma_{\text{stat}} \pm \sigma_{\text{sys}}$	Cut-off energy (TeV)	Reference
Mkn 421	0.030	MAGIC	0.10 – 3.0	$2.20 \pm 0.08 \pm 0.20$	$1.44 \pm 0.28$	Albert <i>et al.</i> (2006c)
Mkn 421	0.030	HEGRA	0.70 – 18.0	$2.19 \pm 0.02 \pm 0.20$	$3.6 + 0.4 - 0.3$	Aharonian <i>et al.</i> (2002b)
Mkn 421	0.030	Whipple	0.35 – 0.90	$2.31 \pm 0.04 \pm 0.05$	—	Krennrich <i>et al.</i> (2002)
Mkn 501	0.034	HEGRA	0.50 – 22.0	$1.92 \pm 0.03 \pm 0.20$	$6.2 \pm 0.4$	Aharonian <i>et al.</i> (1999b)
1ES2344+514	0.044	Whipple	0.80 – 11.0	$2.54 \pm 0.17 \pm 0.07$	—	Schroedter <i>et al.</i> (2005)
Mkn 180	0.045	MAGIC	0.14 – 1.5	$3.25 \pm 0.66 \pm 0.2$	—	Albert <i>et al.</i> (2006b)
1ES1959+650	0.047	HEGRA	1.5 – 13.0	$2.83 \pm 0.14 \pm 0.08$	—	Aharonian <i>et al.</i> (2003a)
PKS2005-489	0.071	H.E.S.S.	0.20 – 2.5	$4.0 \pm 0.4 (\pm 0.2)$	—	Aharonian <i>et al.</i> (2005c)
PKS2155-304	0.116	H.E.S.S.	0.20 – 3.5	$3.37 \pm 0.07 \pm 0.10$	—	Aharonian <i>et al.</i> (2005e)
H1426+428	0.129	HEGRA	0.70 – 12.0	$2.6 \pm 0.6 \pm 0.1$	—	Aharonian <i>et al.</i> (2003c)
H2356-309	0.165	H.E.S.S.	0.16 – 1.0	$3.06 \pm 0.21 \pm 0.10$	—	Aharonian <i>et al.</i> (2006c)
1ES1218+304	0.182	MAGIC	0.08 – 0.7	$3.0 \pm 0.4 \pm 0.6$	—	Albert <i>et al.</i> (2006a)
1ES1101-232	0.186	H.E.S.S.	0.16 – 3.3	$2.88 \pm 0.14 \pm 0.1$	—	Aharonian <i>et al.</i> (2006b)

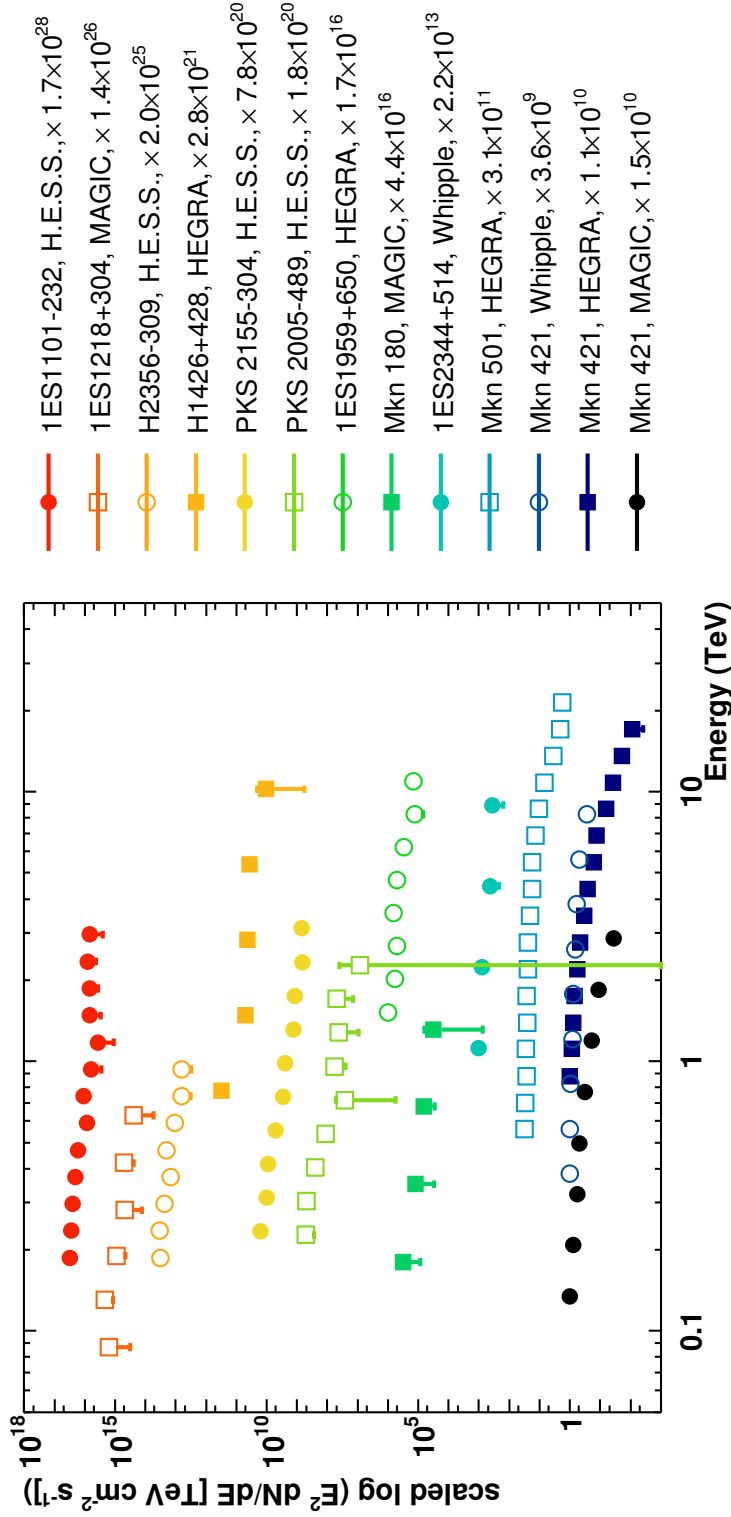


FIGURE 3.7: TeV blazar sample chosen for this study. All detected TeV blazars are represented with at least one spectrum with the exception of PG 1553+113 (unknown redshift). The spectra are multiplied by  $E^2$  to emphasize spectral differences and are spread out along the Y-axis and ordered in redshift to avoid cluttering of the plot. The corresponding scaling factors are given in the legend of the plot.

be to combine the measurements from different experiments, as it was done before in the case of H 1426+428 (Aharonian *et al.* 2003c). However, since the sources are known to be variable in flux level and spectral shape, a combination of non-simultaneous data is not trivial. In addition, in a conservative approach one has to take into account the systematic errors reported by the individual experiments, which are in the order of 20%. Our method is quite sensitive to the errors of the individual flux points<sup>6</sup>, and this additional error would weaken our results. We therefore do not use combined spectra. The selected TeV blazar spectra are summarized in Fig. 3.7 and Table 3.1. In Fig. 3.7 the spectra are multiplied by  $E^2$  to emphasize spectral differences and are spread out along the Y-axis and ordered in redshift to avoid cluttering of the plot.

We did not include data from the radio galaxy M 87, which was recently confirmed as a VHE  $\gamma$ -ray emitter (Aharonian *et al.* 2006e). M 87 is a close by source ( $z = 0.00436$ ), so even for high EBL densities the attenuation is weak and would only be noticeable at high energies  $\sim 30$  TeV. Nevertheless, M 87 has a hard spectrum with a photon index of  $\Gamma \sim 2.2$  currently measured up to 20 TeV, so further observations, extending the energy range to even higher energies, could make M 87 an interesting target for EBL studies as well.

As discussed in Sect. 3.4, the cross section  $\sigma_{\gamma\gamma}$  of the pair production process has a distinct peak close to the threshold. The maximum attenuation of VHE photons of energy  $E_\gamma$  occurs by interaction with low energy photons with a wavelength:

$$\lambda^{\max}(\mu\text{m}) \approx 1.24 E_\gamma(\text{TeV}) \quad (3.10)$$

Since the selected spectra cover an energy region from 100 GeV up to more than 20 TeV, the EBL wavelength range for the absorption of VHE  $\gamma$ -rays spans from the UV ( $\sim 0.1 \mu\text{m}$ ) to the mid IR ( $\sim 30 \mu\text{m}$ ). This region is of particular cosmological interest since it might contain a signature of Population III stars.

### 3.7 Exclusion Criteria

We aim to construct an upper limit on the EBL density using the TeV blazar sample described in Section 3.6. In order to achieve this, we examine for every EBL shape (as introduced in Section 3.5), whether the intrinsic TeV blazar spectra, which result from correcting the measured spectra for the corresponding optical depths, are physically possible. EBL shapes are considered allowed if the intrinsic spectra of all tested TeV blazars are physical feasible, i.e. in the limits of the theory. As upper limit of the EBL density we define the upper envelope of all allowed shapes. It is constraining in the wavelength range where it lies below the maximum shape of the scan. Otherwise no upper limit is quoted.

There are different ways to examine a TeV blazar spectrum upon its feasibility. In this paper we follow very general arguments arising from the shock acceleration scenario of relativistic particles. In this well accepted view, electrons are Fermi-accelerated with a resulting power law spectrum of  $dN/dE \sim E^{-\alpha}$ , with a slope  $\alpha$  of about 2. Due to a faster cooling of high energy electrons compared to lower energies, the slope  $\alpha$  can be larger than 2 but there is no simple theoretical possibility to produce an electron

<sup>6</sup>As further discussed in Sect. 3.7, we take into account the errors of parameters derived from a fit. These parameter errors depend on the errors of the individual flux points.

TABLE 3.2: Analytical functions which are used to fit the intrinsic TeV blazar spectrum. The fitting procedure is performed starting with the simplest function (PL) and the determined parameters are evaluated. In case the parameters do not lead to an exclusion or the fit has a bad quality, the next higher function is used. In case the higher function has a good fit probability and the likelihood ratio test (Appendix B) favors it in respect to the lower functions, the fit parameters are evaluated.

#	Description	Abbreviation	Formula $f(E) = dN/dE$	Parameters to evaluate
1	simple power law	PL	$N_0 E^{-\Gamma}$	$\chi^2, \Gamma^{\text{PL}}$
2	broken power law with transition region	BPL	$N_0 E^{-\Gamma_1} \left[ 1 + \left( \frac{E}{E_b} \right)^f \right]^{\frac{\Gamma_1 - \Gamma_2}{f}}$	$\chi^2, \Gamma_1^{\text{BPL}}, \Gamma_2^{\text{BPL}}$
3	broken power law with transition region and super-exponential pile-up	BPLSE	$N_0 E^{-\Gamma_1} \left[ 1 + \left( \frac{E}{E_b} \right)^f \right]^{\frac{\Gamma_1 - \Gamma_2}{f}} \exp\left(\frac{E}{E_p}\right)$	$\chi^2$
4	double broken power law with transition regions	DBPL	$N_0 E^{-\Gamma_1} \left[ 1 + \left( \frac{E}{E_{b1}} \right)^{f_1} \right]^{\frac{\Gamma_1 - \Gamma_2}{f_1}} \left[ 1 + \left( \frac{E}{E_{b2}} \right)^{f_2} \right]^{\frac{\Gamma_2 - \Gamma_3}{f_2}}$	$\chi^2, \Gamma_1^{\text{DBPL}}, \Gamma_2^{\text{DBPL}}, \Gamma_3^{\text{DBPL}}$
5	double broken power law with transition regions and super-exponential pile-up	DBPLSE	$\text{DBPL} \times \exp\left(\frac{E}{E_p}\right)$	$\chi^2$

spectrum with a harder spectrum. Given an electron spectrum, one can calculate the slope of the synchrotron energy spectrum: it is  $dN/dE_\gamma \sim E_\gamma^{-\Gamma}$  with a photon index  $\Gamma = \frac{\alpha+1}{2} = 1.5$ . The energy spectrum of inverse Compton (IC) photons, independent of the origin of the target photons, has approximately the same photon index as the synchrotron energy spectrum if the scattering occurs in the Thomson regime. In case of the Klein-Nishima regime, the index is even larger. Thus, the photon index of the energy spectrum of VHE photons originating from an IC scattering is  $\Gamma = 1.5$  or larger. In the case of hadronic origin, the photon spectrum can be more complicated. Assuming the VHE  $\gamma$ -rays are produced via  $\pi^0$  decay of high energy protons following a power-law distribution with index  $\Gamma_p$ , the photon spectral distribution will also be a power law with spectral index  $\Gamma_\gamma = 4/3(\Gamma_p - 1/2)$  (e.g. Weekes (2003)). For reasonable values of  $\Gamma_p \sim 2$  the gamma spectrum has the same spectral index  $\Gamma_\gamma \sim 2$ . In conclusion, we assume that the photon index  $\Gamma$  of the intrinsic TeV blazar spectrum is 1.5 or larger. These arguments were recently used in (Aharonian *et al.* 2003c, 2006b,d; Albert *et al.* 2007a).

However, a possibility to obtain even harder photon spectra is not fully excluded. For instance, though in contrary to a wide acceptance of these general arguments, Katarzyński *et al.* (2006) argued that synchrotron emission as well as IC scattering of relativistic electrons does not necessarily occur close to the region of electron acceleration. If so, due to propagation effects, the electron spectrum can become truncated, i.e. the minimum energy of electrons can be as high as several GeV. In an extreme case, we deal with a monoenergetic spectrum of VHE relativistic electrons. Then, and this is the most extreme case, a resulting IC photon index can be as small as  $\Gamma = 2/3$ . We use this limit in the present paper, in addition to the standard limit of  $\Gamma = 1.5$ , to demonstrate the strength of our method.

In the simplest models, it is assumed that the VHE photons originate from a single compact emission region (one-zone scenario). The resulting energy distribution in  $\log(\nu F(\nu))$  vs.  $\log(\nu)$  representation has two peaks: the synchrotron and the inverse Compton (IC) peak. There are no obvious arguments against scenarios with several emission regions. Then, the measured spectrum of a VHE  $\gamma$ -ray emitting source will be a superposition of several one-zone emission regions. So far, there is no indication for this in the measured spectra. However, the attenuation of VHE  $\gamma$ -rays by EBL photons could hide such substructures.

In addition to assuming a certain minimum photon index for the intrinsic TeV blazar spectra, we also argue that an exponentially (or stronger) rising energy spectrum with increasing energy is not realistic (*pile-up*). Such a rise towards high energies was first noticed by Protheroe & Meyer (2000) for the Mkn 501 spectrum and early attempts to avoid it invoked violation of the Lorentz invariance (Kifune 1999; Protheroe & Meyer 2000). On the other hand, Stecker & Glashow (2001) argued that the same Mkn 501 spectrum data can be used to place constraints on the Lorentz invariance breaking parameter. Another possibility to explain pile-ups would require an ultra-relativistic jet with very high bulk motion Lorentz factor  $\Gamma_0 > 3 \times 10^7$  (Aharonian *et al.* 2001). The pile-ups, however, seem to arise at different energies for different sources, which is not expected by these models. Moreover, the pile-ups can be easily avoided by choosing a sufficiently low level of the EBL density and taking systematic error of the measurements into account.

Based on the arguments above and including possible multizone emission scenar-

ios, we assume that at least one of the following smooth analytical functions can describe the intrinsic spectrum satisfactorily: A simple power law (PL), a broken power law with a transition region (BPL), a broken power law with a transition region and a super-exponential pile-up (BPLSE), a double broken power law with two transition regions (DBPL), or a double broken power law with two transition regions and a super-exponential pile-up (DBPLSE). The functions are summarized in Table 3.2.

In our approach to examine intrinsic spectra of TeV blazars, we adopt the general assumption that one of the functions presented in the previous paragraph is a good analytical description of the intrinsic spectrum. In case we fail to find a function, a given EBL shape (realization) is not excluded. It is noteworthy that less than 0.06% of all intrinsic spectra of the TeV blazars could not be fitted well by the chosen functional forms.

In order to determine a good analytic description, we fit the intrinsic spectrum with the functions listed above, starting with the simplest one (PL). As “good description” we take a fit with a chance probability  $P_{\text{Fit}} > 5\%$  based on its  $\chi^2$  value. The determined fit parameters are examined to be physically meaningful for the intrinsic spectrum as described further below. If the fit has a smaller probability we take the next function from the list (Table 3.2). Also if the fit has a chance probability  $P_{\text{Fit}} > 5\%$  but the determined parameters do not lead to an exclusion of the corresponding EBL shape, we take the next function from the list. The reason is that a function with more free parameters can lead to a significantly better fit. In order to make sure that a more complicated function indeed describes the intrinsic shape better than a simpler one, we use the likelihood ratio test (Eadie *et al.* (1988), Appendix A). We require at least a 95% probability to prefer a function with a higher number of free parameters. Only if the function is preferred, we examine its fitted parameters and their errors. Spectra with  $n$  data points are only fitted with functions with up to  $n - 1$  parameters. In case of spectra with low statistics, we fix the softness of the break ( $f$ , see Table 3.2) between two spectral indices to an *a priori* chosen value of  $f = 4$  to allow for a fit by a higher order function (e.g. in case of the BPL for H 1426+428).

We finally define the following criteria to exclude an assumed EBL shape:

- At least one of the determined photon indices from the best hypothesis is outside of the allowed range, i.e.  $\Gamma^{i,\text{max}} < \Gamma^{\text{limit}}$ , where  $\Gamma^{\text{limit}} = 1.5$  or  $2/3$ , and  $\Gamma^{i,\text{max}} = \Gamma^i + \sigma_{\Gamma^i} + \sigma_{\text{sy}}$  with  $\Gamma^i$  and  $\sigma_{\Gamma^i}$  the fitted photon index and its error respectively, and  $\sigma_{\text{sy}}$  as the systematic error on the spectral slope (as given for the corresponding measurement).
- The best fit is obtained by one of the two shapes with an exponential pile-up (BPLSE or DBPLSE).

A single confidence level for the derived upper limits on the EBL density cannot easily be quoted: For the test on the photon index we use a  $1\sigma$  confidence level (as defined for two-sided distributions, including systematic errors). For the likelihood ratio test we use a  $2\sigma$  level (as defined for one-sided distributions). Thus, the confidence level for the upper limit ranges from 68% to 95%.

As discussed in this Section, the theoretical expectations on the smallest possible photon index  $\Gamma^{\text{limit}}$  have a certain spread. Thus, we perform two EBL scans, assuming for the first *realistic* case a limit of  $\Gamma^{\text{limit}} = 1.5$  and for the second *extreme* case a limit of  $\Gamma^{\text{limit}} = 2/3$ . We will further refer to *realistic* and *extreme* scan accordingly.

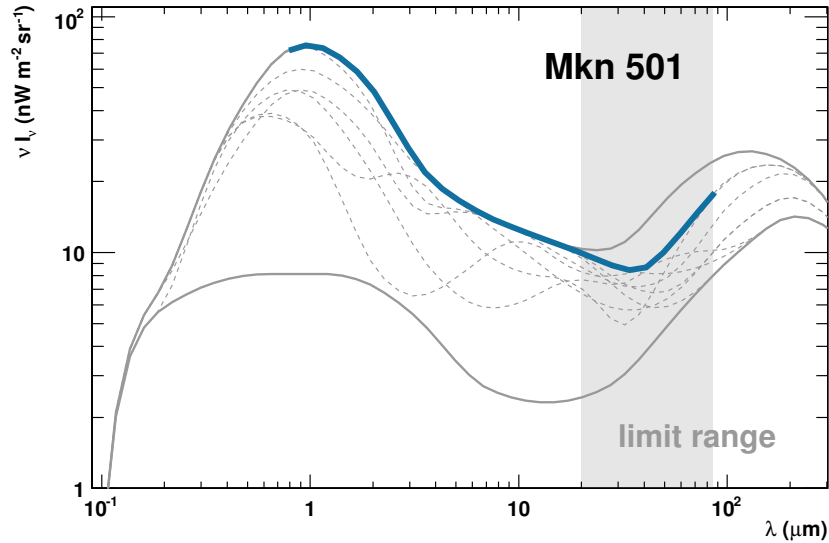


FIGURE 3.8: Limits on the EBL density from Mkn 501 ( $\Gamma_{\max} > 1.5$ ). Grey solid curves are the minimum and maximum shapes of the scan, grey dashed curves are all the highest allowed EBL shapes for Mkn 501, the thick colored curve is the corresponding envelope shape. The grey shaded area marks the wavelength region, in which the envelope shape is constraining the EBL density.

Since our exclusion criteria solely take into account the effect of an EBL shape on the hardness of the spectra of extragalactic VHE  $\gamma$ -ray sources, some shapes might be considered viable in our scan, even though other criteria for exclusion could be found (e.g. exclusion based on spectral shape of the EBL, related to the energy density of star and dust emission as discussed in Dwek & Krennrich (2005)). In this respect our approach is conservative.

### 3.8 Results for individual Spectra

To present the results for individual spectra in a compact and non-repetitive way, we sort our preselected spectra into three categories. For each category we select one prototype spectrum (following similar criteria as discussed in Section 3.6), for which we will give results. The categories considered are:

*"Close by and well measured"*. As prototype spectrum we select the Mkn 501 spectrum ( $z = 0.034$ ) recorded by HEGRA during a major TeV flare in 1997. The spectrum is a relatively hard and provides good statistics from 800 GeV up to 25 TeV. Other sources in this category are Mkn 421 and 1ES 1959+650. 1ES 2344+514 and Mkn 180 are at a comparable distance, but the spectra do not have such a high statistics. PKS 2005-489 lies somewhere between this and the following category. Spectra in this category mainly provide limits in the FIR due to a pile-up at high energies.

*"Intermediate distance, wide energy range"*. The prototype for this category is the spectrum from H 1426+428 at a redshift of  $z = 0.129$ , with energies ranging from

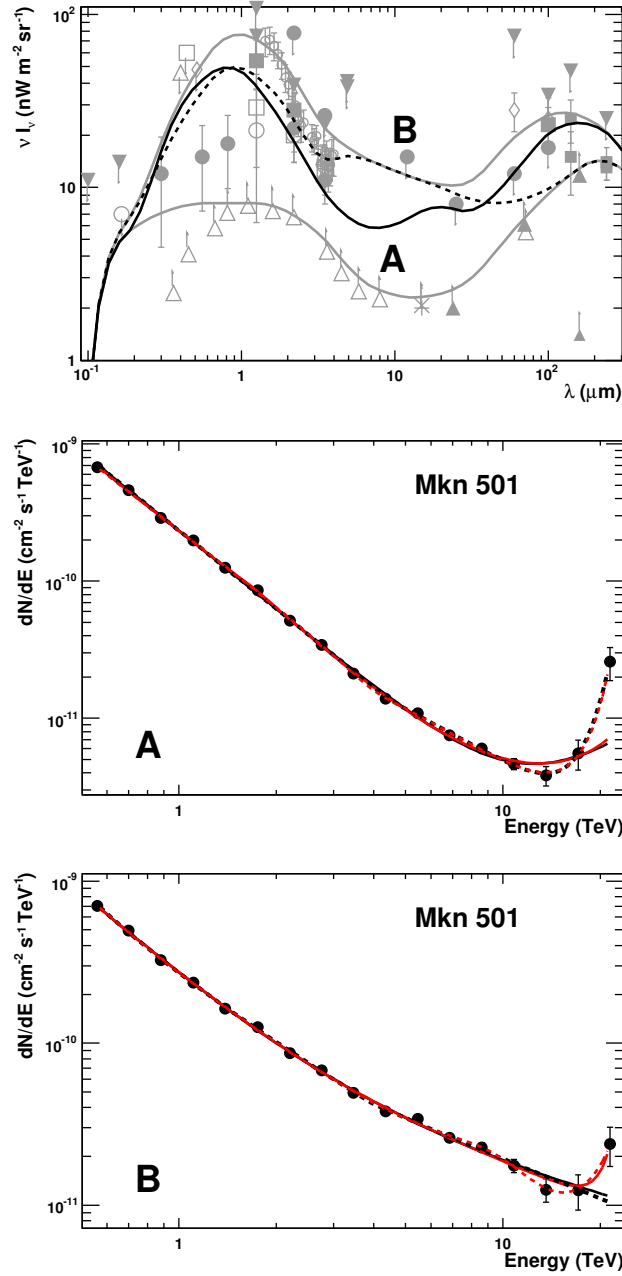


FIGURE 3.9: Mkn 501 individual results ( $\Gamma_{\max} > 1.5$ ). *Upper Panel*: Two example maximum allowed shapes A (solid line) and B (dashed line) overlaid on EBL measurements and minimum and maximum shape of the scan (grey). *Middle Panel*: Intrinsic spectrum for shape A and fit functions: BPL (solid black line), BPLSE (solid red line), DBPL (dashed black line) and DBPLSE (dashed red line). The fit parameters can be found in Table 3.3. The BPL and BPLSE are not good fits; The DBPL is a good fit and its parameters are within the allowed range; The DBPLSE is not preferred over the BPL and the DBPL. *Lower Panel*: Intrinsic spectrum for shape B and the same fit functions as in the Middle Panel. The fit parameters can be found in Table 3.3. All four functions are good fits. No function is preferred over the BPL.

TABLE 3.3: Fit results for the Mkn 501 spectrum using the functions from Fig. 3.9. Fit probabilities are given in the column “ $P_{\text{Fit}}$ ”. The parameters are put in parentheses if the corresponding fit has a low probability or is not preferred over a fit by a function with less free parameters. The latter is a result of the likelihood ratio test and is indicated in the column “Pref”.

	$P_{\text{Fit}}$	Pref.	$\Gamma_{1,\text{max}}$	$\Gamma_{2,\text{max}}$	$\Gamma_{3,\text{max}}$
<b>Shape A</b>					
BPL	0.00	—	(2.13)	(-0.47)	—
BPLSE	0.04	—	—	—	—
DBPL	0.19	yes	2.12	1.62	8.92
DBPLSE	0.40	no	—	—	—
<b>Shape B</b>					
BPL	0.16	yes	2.85	1.77	—
BPLSE	0.23	no	—	—	—
DBPL	0.12	no	(3.91)	(1.42)	(1.05)
DBPLSE	0.24	no	—	—	—

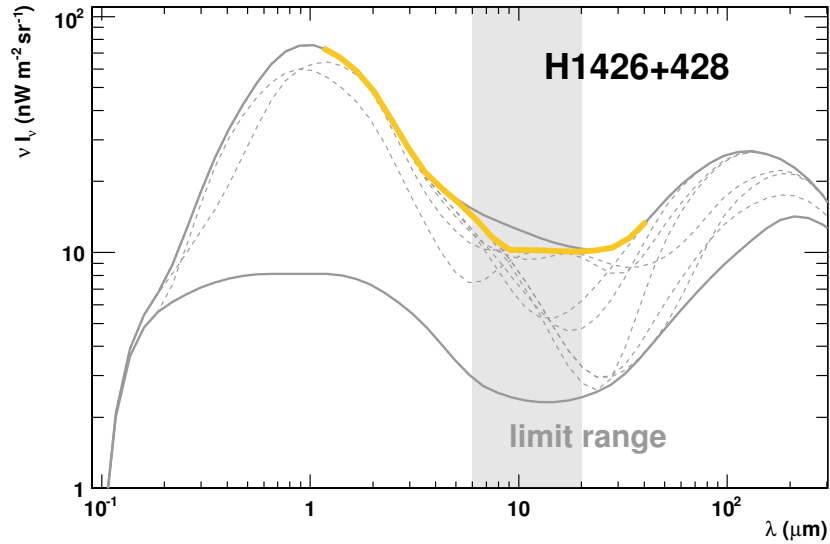


FIGURE 3.10: Limits on the EBL density from H1426+428 ( $\Gamma_{\text{max}} > 1.5$ ). Grey solid curves are the minimum and maximum shapes of the scan, grey dashed curves are all the highest allowed EBL shapes for H1426+428, the thick colored curve is the corresponding envelope shape. The grey shaded area marks the wavelength region, in which the envelope shape is constraining the EBL density.

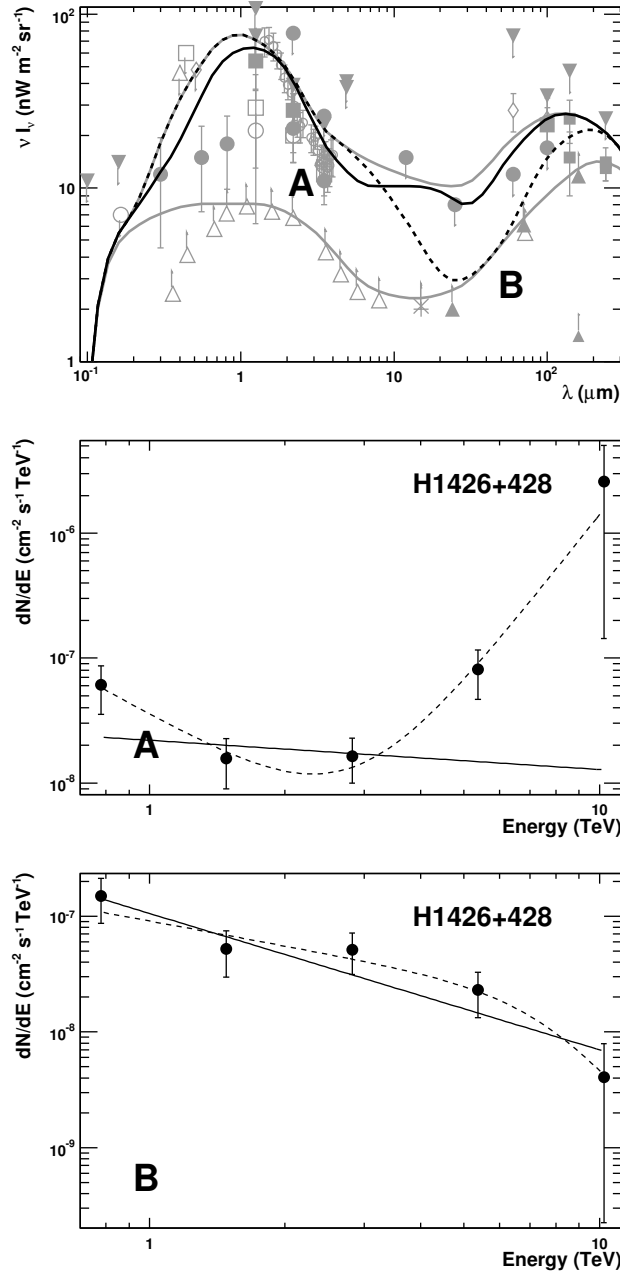


FIGURE 3.11: H1426+428 individual results ( $\Gamma_{\max} > 1.5$ ). *Upper Panel*: Two example maximum allowed shapes A (solid line) and B (dashed line) overlaid on EBL measurements and minimum and maximum shape of the scan (grey). *Middle Panel*: Intrinsic spectrum for shape A and fit functions. Both PL (solid line) and BPL (dashed line) are good fits;  $\Gamma_{\max}^{\text{PL}} = 0.23 + 1.18_{\text{stat}} + 0.2_{\text{sys}} = 1.61$  and the BPL fit is preferred over the PL fit ( $P_{(\text{BPL vs. PL})} = 0.97$ );  $\Gamma_{1,\max}^{\text{BPL}} = 2.01 + 1.94_{\text{stat}} + 0.2_{\text{sys}} = 4.15$  and  $\Gamma_{2,\max}^{\text{BPL}} = -4.59 + 6.67_{\text{stat}} + 0.2_{\text{sys}} = 2.28$ . *Lower Panel*: Intrinsic spectrum for shape B and fit functions. Both PL (solid line) and BPL (dashed line) are good fits;  $\Gamma_{\max}^{\text{PL}} = 1.18 + 0.24_{\text{stat}} + 0.2_{\text{sys}} = 1.63$  and the BPL fit is not preferred over the PL fit ( $P_{(\text{BPL vs. PL})} = 0.54$ );

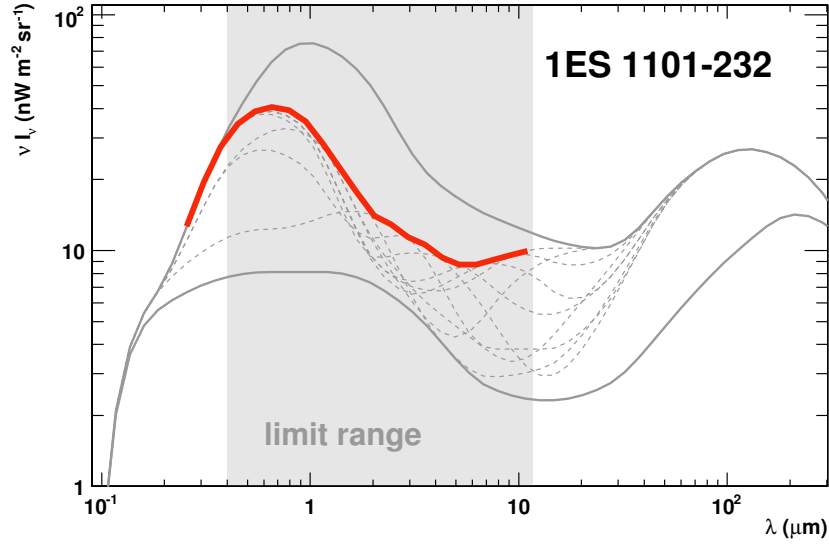


FIGURE 3.12: Limits on the EBL density from 1ES 1101-232 ( $\Gamma_{\max} > 1.5$ ). Grey solid curves are the minimum and maximum shapes of the scan, grey dashed curves are all the highest allowed EBL shapes for 1ES 1101-232, the thick colored curve is the corresponding envelope shape. The grey shaded area marks the wavelength region, in which the envelope shape is constraining the EBL density.

700 GeV up to 12 TeV. PKS 2155-304 is at a comparable distance and its measured spectrum has a better statistic, but the highest energy point is only at 2.5 TeV and the spectrum is much softer.

*"Distant source, hard spectrum"*. The most distant TeV blazar discovered so far with a published energy spectrum is 1ES 1101-232 at a redshift of  $z = 0.186$ . Its spectrum is hard and ranges from 160 GeV to 3.3 TeV. H 2356-309 and 1ES 1218+304 are at similar distances, but the statistics are not as good and/or the spectrum is softer. This makes 1ES 1101-232 the natural choice for a prototype spectrum in this category.

As limit on the EBL for the individual spectra (and for the combined results in Section 3.9 as well) we indicate the envelope shape of all allowed EBL shapes. In most cases a single EBL shape represents the maximum allowed shape (the highest allowed shape at a certain wavelength range) only for a small wavelength interval. Consequently the envelope shape consists of a number of segments from different EBL shapes (which we will label highest allowed shapes). One exception occurs, if the maximum shape tested in the scan is allowed. In this case the spectrum does not constrain the EBL density. In general, a spectrum constrains the EBL density when the envelope shape lies below the maximum shape tested in the scan.

Given the energy range of the spectra, the limit is only valid for wavelengths  $\lambda_{\text{Lim}}$ :

$$\lambda^{\max}(E_{\min}) < \lambda_{\text{Lim}} < \lambda^{\text{thresh}}(E_{\max}) \quad (3.11)$$

where  $\lambda^{\max}(E_{\min})$  is the wavelength for which the cross section for pair production with the lowest energy point of the VHE spectrum  $E_{\min}$  is maximized (following Eqn. (3.10)).

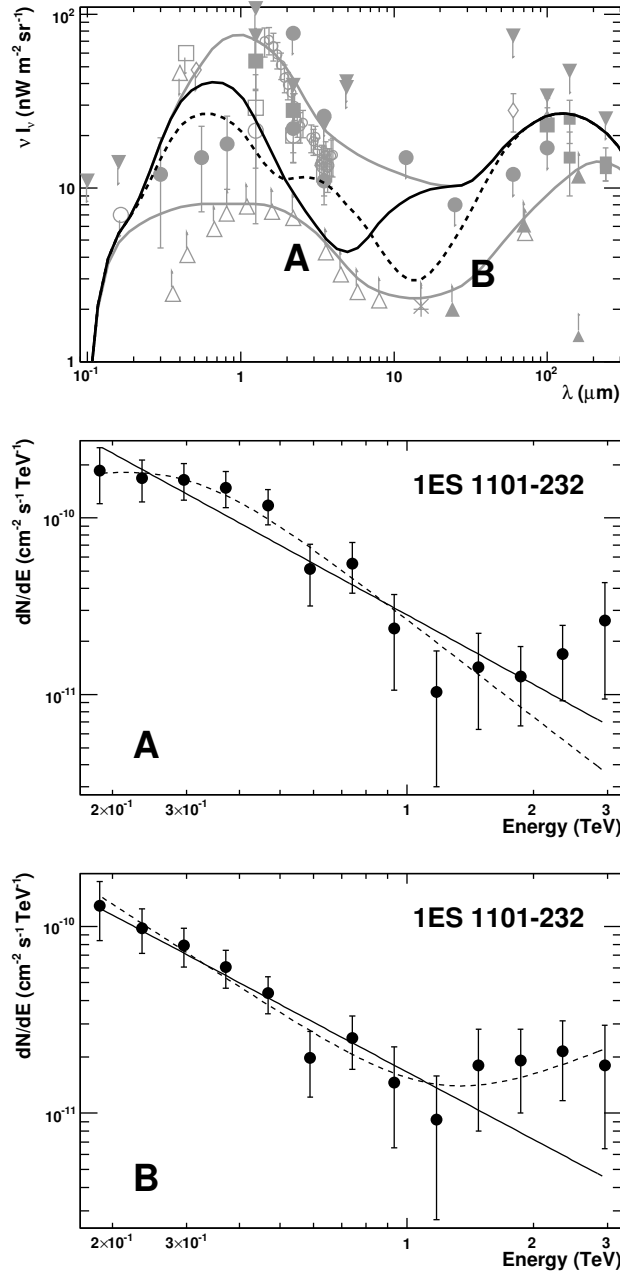


FIGURE 3.13: 1ES 1101-232 individual results ( $\Gamma_{\max} > 1.5$ ). *Upper Panel:* Two example maximum allowed shapes A (solid line) and B (dashed line) overlaid on EBL measurements and minimum and maximum shape of the scan (grey). *Middle Panel:* Intrinsic spectrum for shape A and fit functions. Both PL (solid line) and BPL (dashed line) are good fits;  $\Gamma_{\max}^{\text{PL}} = 1.31 + 0.13_{\text{stat}} + 0.1_{\text{sys}} = 1.53$  and the BPL fit is not preferred over the PL fit ( $P_{(\text{BPL vs. PL})} = 0.87$ ). *Lower Panel:* Intrinsic spectrum for shape B and fit functions. Both PL (solid line) and BPL (dashed line) are good fits;  $\Gamma_{\max}^{\text{PL}} = 1.21 + 0.21_{\text{stat}} + 0.1_{\text{sys}} = 1.52$  and the BPL fit is not preferred over the PL fit ( $P_{(\text{BPL vs. PL})} = 0.9488$ ).

$\lambda^{\text{thresh}}(E_{\text{max}})$  is the threshold wavelength for pair production with the highest energy point of the VHE spectrum  $E_{\text{max}}$ . This wavelength range roughly reflects the sensitivity of the exclusion criteria. There is of course some freedom of choice for the wavelength range, given the complexity of the criteria.

In the following three Subsections the results for the individual prototype spectra for the *realistic* scan with  $\Gamma_{\text{max}} > 1.5$  are summarized. The results for the *extreme* scan with  $\Gamma_{\text{max}} > 2/3$  for all prototype spectra are presented in Subsection 3.8.4.

### 3.8.1 Close by and well measured: Mkn 501 (HEGRA)

The envelope shape derived for the Mkn 501 spectrum is shown in Fig. 3.8 in comparison with the maximum and minimum EBL shapes tested in the scan. Though 7766674 out of 8064000 EBL shapes (96.3%) can be excluded, the effective limit is only constraining in the 20 to 80  $\mu\text{m}$  wavelength region, where it lies below the maximum tested shape. Note that our method is not only testing the overall level of the EBL density but is also sensitive to its structures. Despite the fact that for the Mkn 501 spectrum almost all of the tested EBL shapes are excluded, certain types of shapes are allowed, independent of their respective EBL density level. This can be illustrated with an EBL shape, which has a power law dependency  $n(\epsilon) \sim \epsilon^{-1}$  or  $\nu I_{\nu} \sim \lambda^{-1}$ . Then the optical depth is independent of the energy of VHE photons and the intrinsic TeV blazar spectrum has the same shape as the observed one (Aharonian 2001). With such a type of shape, an allowed high EBL density level in the MIR can be constructed by choosing a corresponding high density level in the optical/NIR.

The rejection power in the FIR results mainly from the hard intrinsic Mkn 501 spectrum above  $\sim 5$  TeV that often can only be described by an exponential or super exponential rise. Two of the limiting shapes together with the resulting intrinsic spectra and fit functions are shown in Fig. 3.9, the corresponding fit results can be found in Table 3.3. The fit with a PL function did not meet our acceptance criteria and the function is omitted from the Figure for the sake of legibility. For the two shapes displayed here, the pile up at high energies is already visible but not yet significant.

### 3.8.2 Intermediate distance, wide energy range: H1426+428

Using the H 1426+428 energy spectrum 5571772 EBL shapes (corresponding to 69.09% of all shapes) are excluded. The resulting envelope shape is displayed in Fig. 3.10 together with all maximum allowed shapes. The limit is constraining from  $\sim 6$  to  $\sim 20$   $\mu\text{m}$  and the constraints are not very strong. This is illustrated in Fig. 3.11, where two representative maximum allowed EBL shapes and the resulting intrinsic spectra are shown together with relevant fit functions. Shape A is almost as high as the maximum shape of the scan. Although the intrinsic spectrum is already convex, the relative low statistics of the spectrum even allows for an acceptable fit by a simple PL and results in large errors on the fit parameters for the BPL. Consequently the EBL shape cannot be excluded. Shape B has a high peak in the O/IR wavelength region but lies below all upper limits in the FIR. The resulting intrinsic spectrum is best described with a simple PL with a maximum slope  $\Gamma_{\text{max}}^{\text{PL}} = 1.63 > 1.5$  and is therefore allowed.

### 3.8.3 Distant source, hard spectrum: 1ES 1101-232

The spectrum from 1ES 1101-232 gives the strongest constraints for all individual spectra, even though slightly less EBL shapes (7706625, 95.57% of all shapes) are excluded than in the case of Mkn 501 (this is due to the different sensitivities in EBL wavelength; the 1ES 1101-232 spectrum is only sensitive up to  $10 \mu\text{m}$ ). The resulting maximum shapes and the envelope shape are shown in Fig. 3.12. The envelope shape constraints the EBL density in the wavelength range from  $\sim 0.4$  to  $\sim 10 \mu\text{m}$  and clearly excludes the NIR excess claimed by Matsumoto *et al.* (2005). At EBL wavelengths of  $\sim 2 \mu\text{m}$  the limit is consistent with the limit derived by Aharonian *et al.* (2006b) for the same source with a different technique (this is further discussed in Section 3.9). Two representative maximum allowed shapes and the corresponding intrinsic spectra are shown in Fig. 3.13. Shape A illustrates the intrinsic spectrum for a high EBL density in the UV/O, while shape B is the maximum shape for wavelengths around  $3 \mu\text{m}$ . For both shapes the examined fit parameters are close to the allowed limits (see caption for values), as expected for maximum allowed shapes.

### 3.8.4 Extreme Case: $\Gamma_{\text{max}} > 2/3$

The upper limits for Mkn 501, H1426+428 and 1ES 1101-232 for the *extreme* case with  $\Gamma_{\text{max}} > 2/3$  are shown in Fig. 3.14 (thick colored dashed line) in comparison to the limits derived for the *realistic* case (thick colored solid line). In the case of Mkn 501, a similar number of EBL shapes (94.13%) as in the *realistic* scan are excluded but the effective limit is less constraining (Fig. 3.14, Upper Left Panel). For H1426+428 the limit almost remains at the same level, still close to the maximum shape tested in the scan (Fig. 3.14, Upper Right Panel). For 1ES 1101-232 the limit in the UV/O lies a factor of 1.2 to 1.8 higher than the limit in the *realistic* case (Fig. 3.14, Lower Left Panel). In the wavelength region from 2 to  $4 \mu\text{m}$  the NIR excess claimed by Matsumoto *et al.* (2005) is now compatible with the limit. In the 1 to  $2 \mu\text{m}$  region the limit still lies clearly below the claimed NIR excess.

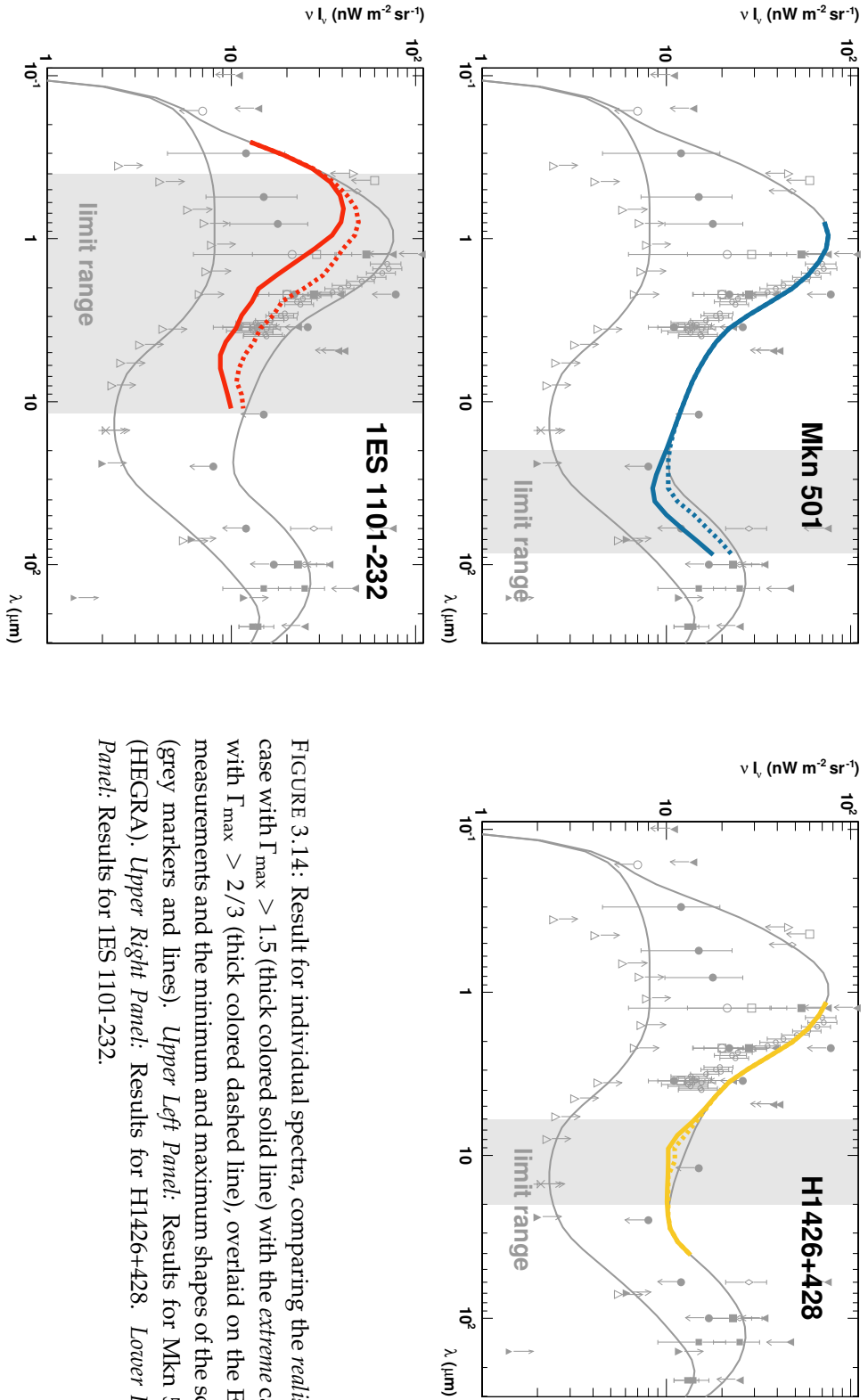


FIGURE 3.14: Result for individual spectra, comparing the *realistic* case with  $\Gamma_{\text{max}} > 1.5$  (thick colored solid line) with the *extreme* case with  $\Gamma_{\text{max}} > 2/3$  (thick colored dashed line), overlaid on the EBL measurements and the minimum and maximum shapes of the scan (grey markers and lines). *Upper Left Panel:* Results for Mkn 501 (HEGRA). *Upper Right Panel:* Results for H1426+428. *Lower Left Panel:* Results for 1ES 1101-232.

TABLE 3.4: Number of excluded EBL shapes for the *realistic* scan for individual spectra (column two) as well as the number of the intrinsic spectra, which could not be fitted satisfactorily (column three). The percentage of these numbers to the number of all shapes (8 064 000) for column two and to the number of the allowed shapes for this spectrum for column three is also quoted. If the number of shapes is zero, the percentage is omitted.

Spectrum	#Shapes Excluded	#Shapes No Fit
Mkn 421 (MAGIC)	1 756 869 (21.79%)	59 258 (0.94%)
Mkn 421 (HEGRA)	888 575 (11.02%)	0
Mkn 421 (Whipple)	2 287 059 (28.36%)	0
Mkn 501	7 760 733 (96.24%)	1296 (0.43%)
1ES 2344+514	0	0
Mkn 180	0	0
1ES 1959+650	1 086 314 (13.47%)	423 (0.01%)
PKS 2005-489	0	0
PKS 2155-304	4 248 872 (52.69%)	0
H 1426+428	5 571 771 (69.09%)	2 (0.00%)
H 2356-309	4 657 817 (57.76%)	0
1ES 1218+304	19 540 (0.24%)	0
1ES 1101-232	7 706 624 (95.57%)	0

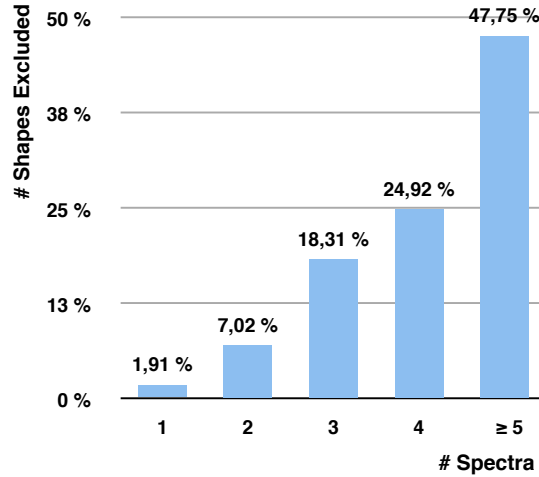


FIGURE 3.15: Number of excluded shapes as percentage of the total number of shapes vs. the number of spectra, that excluded the shape. A large fraction of shapes (98.08%) is excluded by more than one spectra.

### 3.9 Combined Results

The number of excluded shapes for all individual spectra for the *realistic* scan are summarized in Table 3.4. One finds that some spectra (namely 1ES 2344+514, Mkn 180 and PKS 2005-489) excluded none of the EBL shapes of the scan. This is mainly a result of

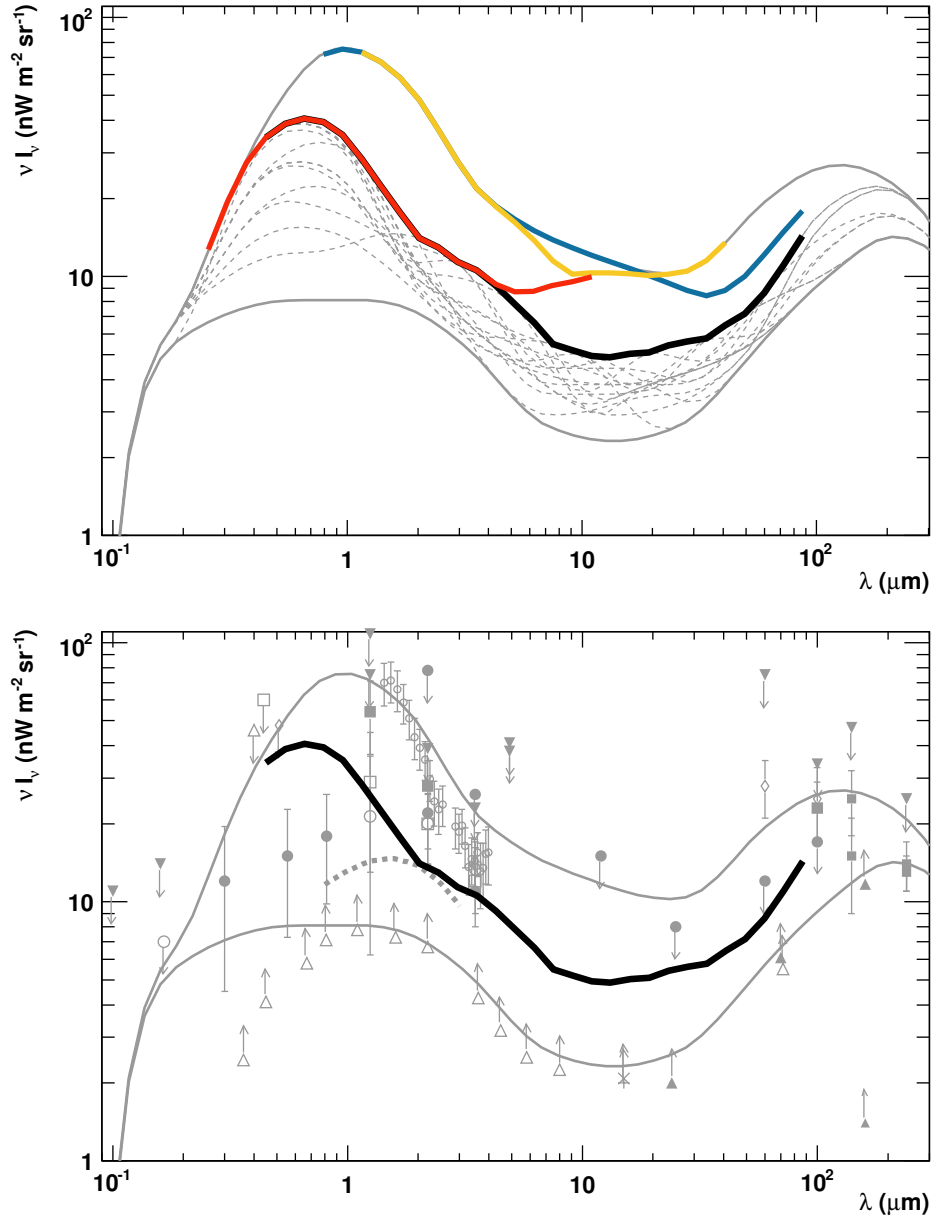


FIGURE 3.16: Combined results for the *realistic* scan. *Upper Panel:* All maximum allowed shapes of the combined scan (dashed grey lines) and the corresponding envelope shape (solid black line) in comparison to the limits for individual spectra: Mkn 501 (solid blue line), H 1426+428 (solid yellow line) and 1ES 1101-232 (solid red line). The minimum and maximum shapes of the scan are also shown (grey lines). *Lower Panel:* The combined limit from the *realistic* scan (solid black line) in comparison to direct measurements and limits (grey markers). The grey dashed curve around  $2 \mu\text{m}$  is the limit derived by Aharonian *et al.* (2006b) for the 1ES 1101-232 spectrum.

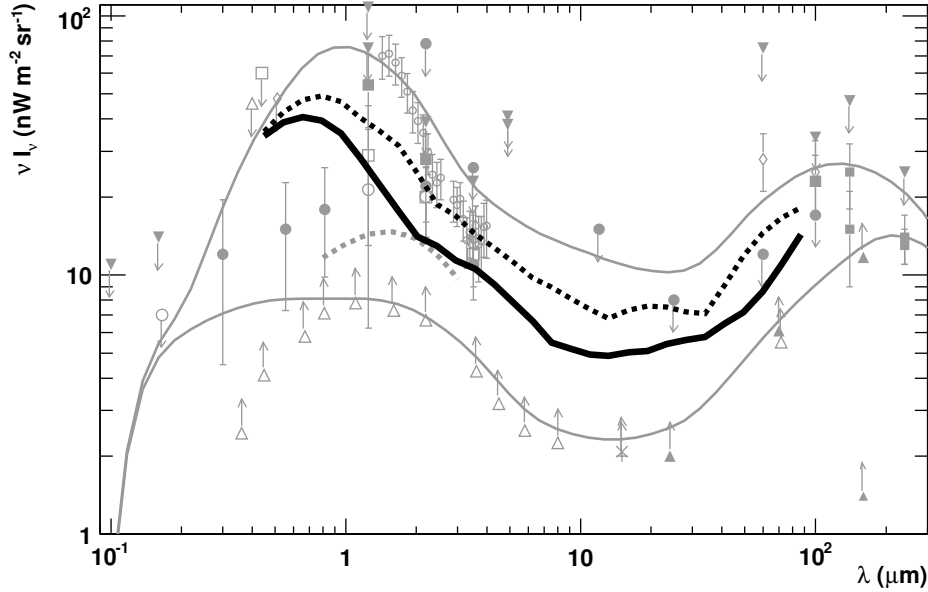


FIGURE 3.17: Combined results from the *extreme* scan (dashed black line) in comparison to the result from the *realistic* scan (solid black line). Grey lines are the minimum and the maximum shapes tested in the scan. Grey markers are direct measurements and limits.

the low statistics in the spectra and hence the large errors on the fit parameters. The highest number of excluded shapes and the strongest constraint in the scan result from the previously presented prototype spectra Mkn 501, H 1426+428 and 1ES 1101-232.

We now combine the results from all spectra by excluding all shapes of the scan, that are excluded by at least one of the spectra. First we present results for the *realistic* scan. A large fraction of the shapes (98.08%) are excluded by more than one spectrum (see Fig. 3.15), which strengthens our results. In total, we exclude 8 056 718 shapes, which leaves us with only 7 282 (0.01%) allowed shapes. The resulting maximum shapes (dashed lines) and the envelope shape for the combined results (solid black line) are shown in Fig. 3.16 Upper Panel in comparison to the results from the individual prototype spectra (colored solid lines). In the optical to near infrared the combined limit follows exactly the limit derived from the 1ES 1101-232 spectrum (red solid line). For larger wavelengths, however, the combined limit lies significantly below the limits derived from individual spectra. This is particularly striking in the MIR, where the H 1426+428 spectrum provided only weak limits (solid yellow line) and the combined limit now gives considerable constraints. This can be understood from the fact that for a high EBL density in the MIR a high density in the optical to NIR is needed, in order for the spectra (Mkn 501, H 1426+428) not to get too hard. These high densities in the optical to NIR are now however excluded by the 1ES 1110-232 spectrum, which therefore results in stronger constraints in the MIR.

The combined limit for the *realistic* scan in comparison to the direct measurements and limits is shown in Fig. 3.16 Lower Panel. In the optical to NIR one finds that the combined limit lies significantly below the claimed NIR excess by Matsumoto *et al.* (2005). It is compatible with the detections reported by Dwek & Arendt (1998), Gorjian *et al.* (2000), Wright & Reese (2000) and Cambrésy *et al.* (2001). In the same figure

the limit reported by the H.E.S.S. collaboration for 1ES 1101-232 derived with a different technique (Aharonian *et al.* 2006b) is shown as dashed grey line around  $2 \mu\text{m}$ . At wavelengths around  $2 - 3 \mu\text{m}$  it is in good agreement with the limit derived here, but for smaller wavelengths our limit lies significantly higher. While for the H.E.S.S. limit comparable exclusion criteria for the intrinsic spectra were used, a fixed reference shape scaled in the overall EBL density was used to calculate the EBL limit<sup>7</sup>, which presumably causes the differences at smaller wavelengths. In the MIR to FIR our combined limit lies below all previously reported upper limits from direct measurements and fluctuation analysis. For EBL wavelengths greater than  $2 \mu\text{m}$  it is only about a factor of 2 to 2.5 higher than the absolute lower limit from source counts, leaving very little room for additional contributions to the EBL in this wavelength region. In the FIR it lies more than a factor of  $\sim 2$  below the claimed detection by Finkbeiner *et al.* (2000).

In the *realistic* scan, after combining the results from Mkn 501, H 1426+428, and 1ES 1110-232, adding more spectra does not further strengthen the limit (though marginally more shapes are excluded). Hence, for the *extreme* scan, we will only combine the results from these three spectra. The limit for the *extreme* scan (dashed line) is shown in Fig. 3.17 in comparison to the limit from the *realistic* scan (solid line) and the limits and direct measurements. The limit from the *extreme* scan lies for all EBL wavelengths above the limits from the realistic scan and is a factor of 2.5 to 3.5 higher than the lower limits from source counts. In the optical to NIR the combined limit follows again the limit derived from the 1ES 1101-232 spectrum. As stated for the individual spectrum the NIR excess claimed by Matsumoto *et al.* (2005) for wavelengths above  $2 \mu\text{m}$  is now compatible with the limit, but for smaller wavelengths it is still clearly excluded.

In Fig. 3.18 the limits derived in this paper are shown in comparison to predictions from EBL models by Kneiske *et al.* (2002), Stecker *et al.* (2006) and Primack *et al.* (2005) (at  $z = 0$ ). Most models lie significantly below our *realistic* limits, only the high model of Kneiske *et al.* (2002) is slightly higher in the NIR and the fast evolution model of Stecker *et al.* (2006) is marginally higher in the MIR. All models lie below the *extreme* limit. Noteworthy the Primack *et al.* (2005) and the low model from Kneiske *et al.* (2002) are below the lower limits derived from galaxy counts in the MIR and FIR.

### 3.10 Estimation of Systematic Errors

We identified three major contributions to the systematic error of the upper limit on the EBL:

**Choice of the Scan Grid** We estimate that the main contribution to the systematic errors arises from the minimum width of the EBL structures that can be resolved by the scan. Although the choice of the grid spacing, which defines the minimum width of the EBL structures, is well physically motivated, there are arguments that even thinner structures could be realized in nature due to e.g. absorption effects. We tested two different grid setups with 13% and 20% smaller grid spacing (labeled n18 and n20, the original setup is n16), resulting in much less realistic but still possible EBL structures, with the 1ES 1101-232 spectrum. The resulting limits on the EBL and the deviation

<sup>7</sup>In addition to the fixed shape several other possible EBL components like a bump in the UV were examined (Aharonian *et al.* 2006b).

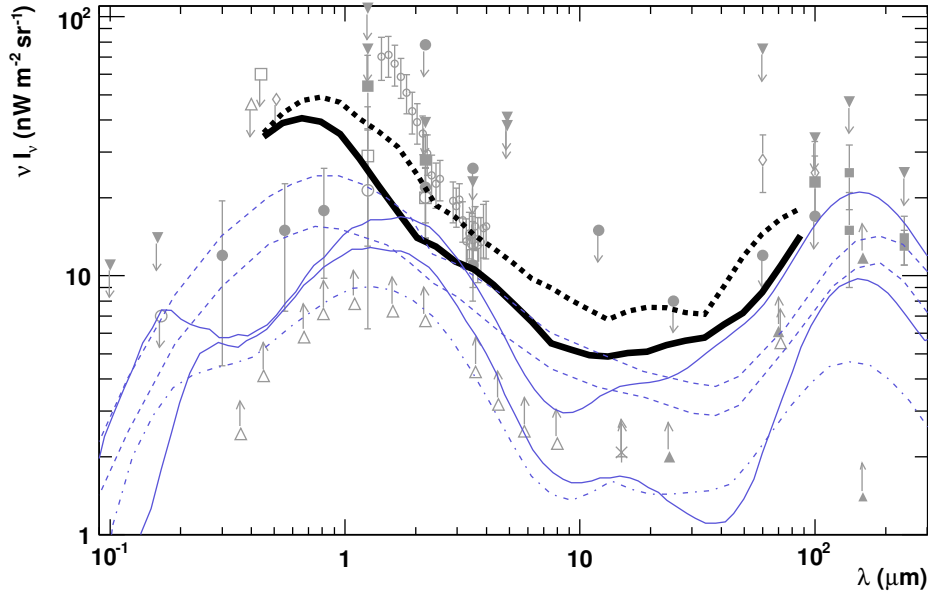


FIGURE 3.18: EBL limits from the *realistic* (thick solid black curve) and the *extreme* scan (thick dashed black curve) in comparison to different EBL models at  $z = 0$  (blue curves): updated version of Kneiske *et al.* (2002) high and low models (solid), Stecker *et al.* (2006) fast and baseline evolution models (dashed), Primack *et al.* (2005) (dashed dotted).

from the original limit are shown in Fig. 3.19. For n20 the limits are 20 to 30% higher than the ones presented in Section 3.9, but the shapes are already "unphysical". This is illustrated in Fig. 3.20, where the highest allowed shapes for the n20 grid setup are shown. Many of the shapes have more than one peak in the UV to MIR, which cannot be accommodated in standard EBL models. The grid setup n20 therefore has to be considered an extreme case. We conclude that the overall contribution from the grid setup to the systematic error is at the most 30%.

**EBL Evolution** Another contribution to the systematic error originates from the fact that we do not consider the evolution of the EBL in our method. In order to estimate the effect of the evolution of the EBL for the most distant sources, we calculate the late contribution to the EBL in the redshift interval between  $z = 0$  and  $z = 0.2$ . Hereby, we utilize the EBL model by Kneiske *et al.* (2002) (updated version is used, Kneiske private communication, Fig. 3.21). We obtain a wavelength dependent contribution, which has a maximum value of 3-4  $\text{nW m}^{-2}\text{sr}^{-1}$  in the optical to NIR (the relevant wavelength region for the distant sources in our scan, Fig. 3.22). Given that these values are derived with the extreme assumption that all late emission occurred instantaneously at  $z=0$ , we estimate the systematic error arising from the EBL evolution to 10% of the derived limits. Note that Aharonian *et al.* (2006b) estimated an error of  $<10\%$  for 1ES 1101-232, the most distant TeV blazar in our study.

**Uncertainty in the Absolute Energy Scale of IACT Measurements** To study the effect of the uncertainties in the absolute energy scale of IACT measurements, we calculate a limit on the EBL utilizing the energy spectra from Mkn 501, H 1426+428 and

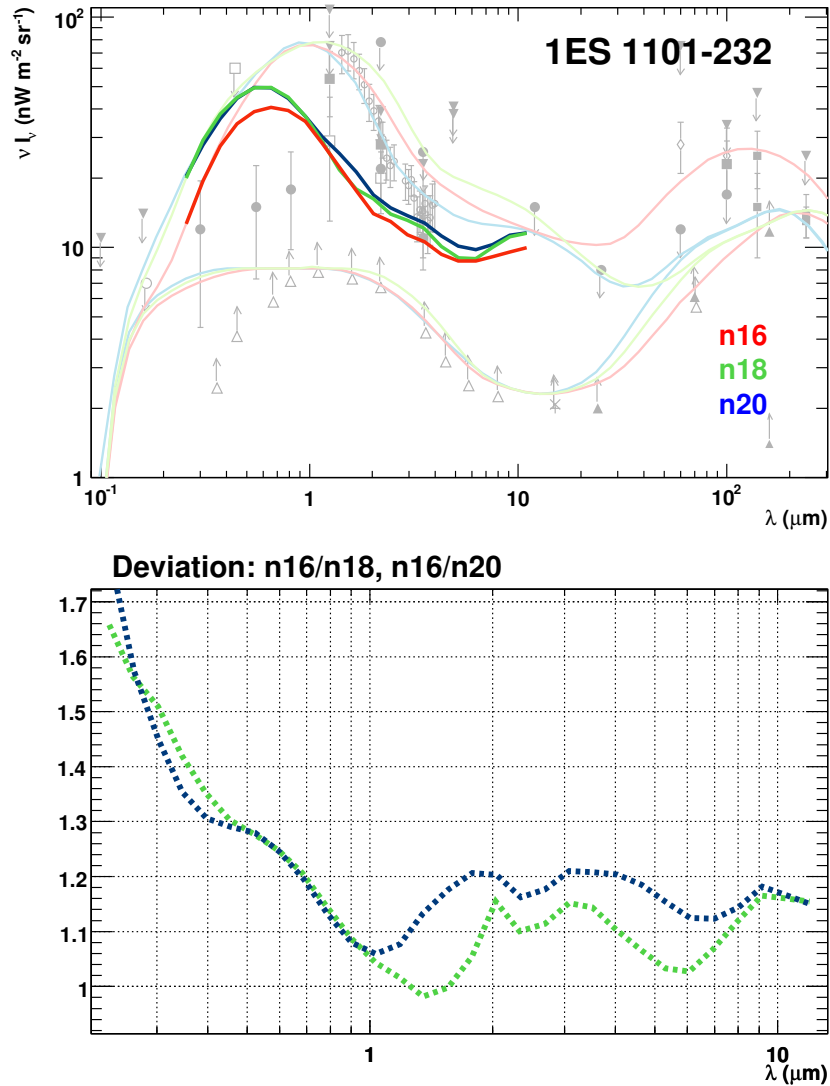


FIGURE 3.19: Comparison of the limits derived for different grid configurations (n16, n18, n20) for the 1ES 1101-232 spectrum. *Upper Panel:* Spectral energy distribution with envelope shapes for n16 (red), n18 (green) and n20 (blue). The light colored curves indicate the minimum and maximum shapes of the respective scan grid. *Lower Panel:* Relative deviation of the envelope curve n18/n16 (green dashed curve) and n20/n16 (blue dashed curve).

1ES 1101-232 shifted by 15% to lower energies (for  $\Gamma > 1.5$ , *realistic* scan). Since the optical depth is increasing with energy, the energy shift reduces the attenuation of the spectra, especially reducing the effect of a possible pile-up at the highest energies. The corresponding limit is shown in Fig. 3.23. The difference between the limit derived from the energy shifted spectra and the *realistic* limit is negligible in the optical to NIR ( $< 6 \mu\text{m}$ ), while there is a moderate effect in the MIR to FIR on the level of  $1 - 4.5 \text{ nW m}^{-2} \text{sr}^{-1}$ . We therefore conclude, that the systematic error in the MIR to FIR ( $\lambda > 6 \mu\text{m}$ ) introduced by the uncertainties in the absolute energy scale of IACT measurements is in the order of 10–45% of our *realistic* limit.

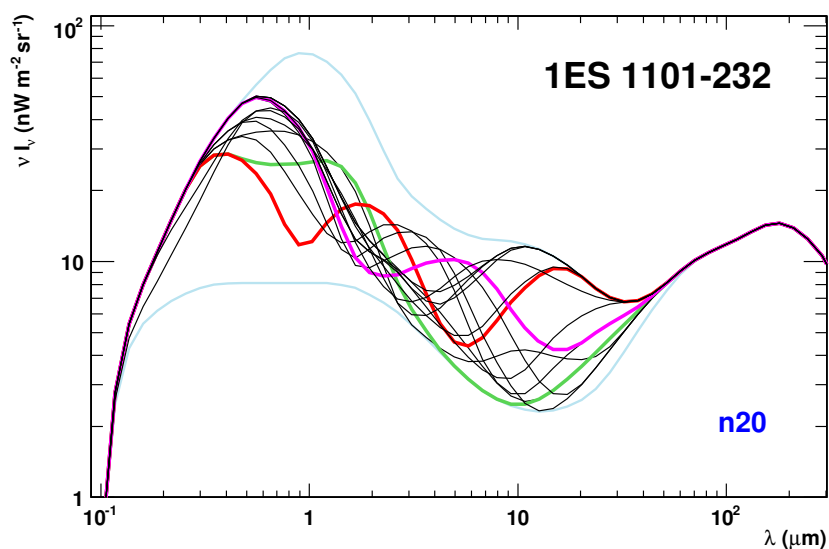


FIGURE 3.20: Highest allowed shapes for 1ES 1101-232 with scan setup n20 (20 steps from 0.1 to  $1000\mu\text{m}$ ). To increase readability, three example shapes are marked with different colors (green, red, pink). The light colored lines give the minimum and maximum shape.

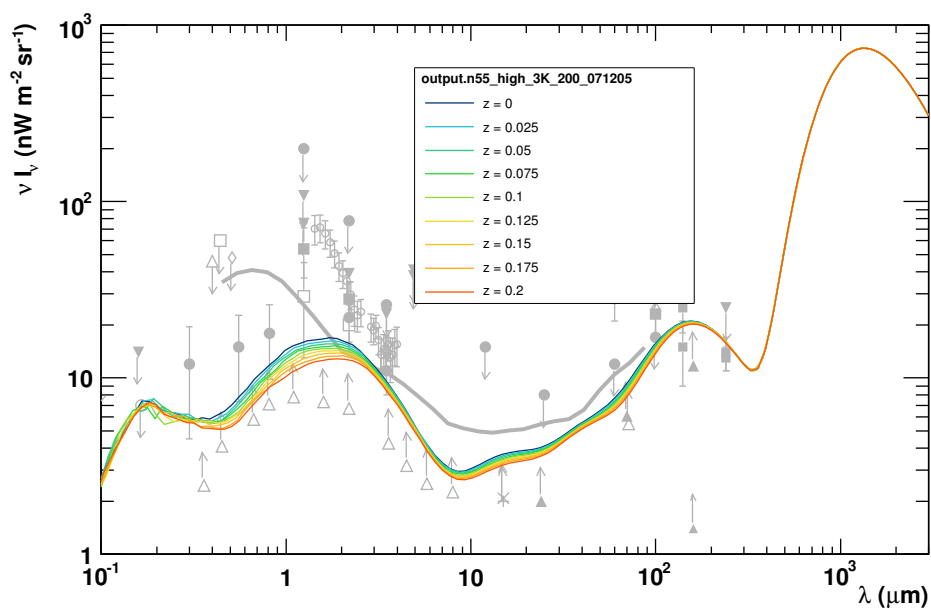


FIGURE 3.21: EBL model from Kneiske (2002, 2004) *high* (updated) for different redshifts propagated to  $z=0$ .

To quote an overall systematic error, we add the individual errors quadratically, resulting in a (very conservative) systematic error on the upper limit of about 32% in the optical to NIR and 33–55% in MIR to FIR.

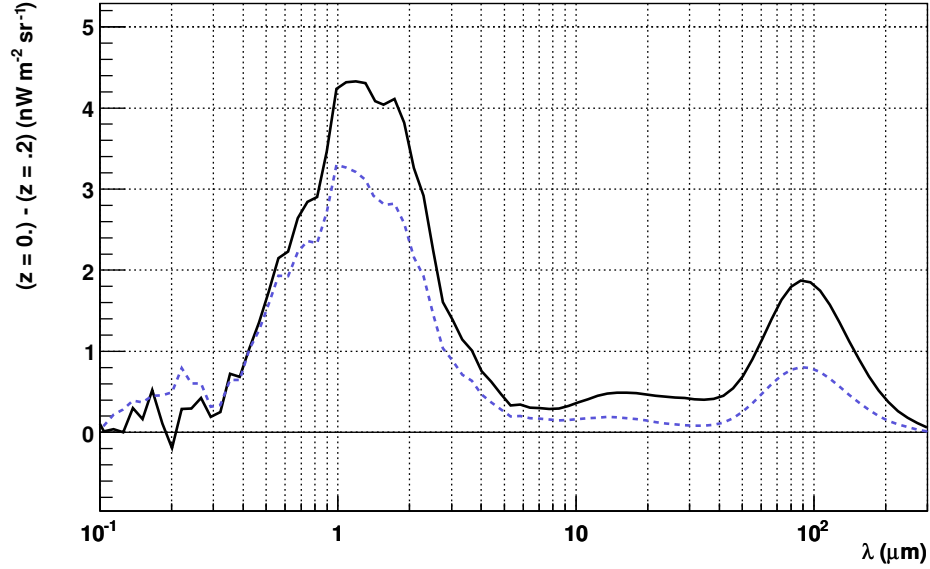


FIGURE 3.22: Difference in the EBL density between  $z = 0$  and  $z = 0.2$  for the Kneiske *high* (solid, black curve) and *low* (dashed, blue curve) model.

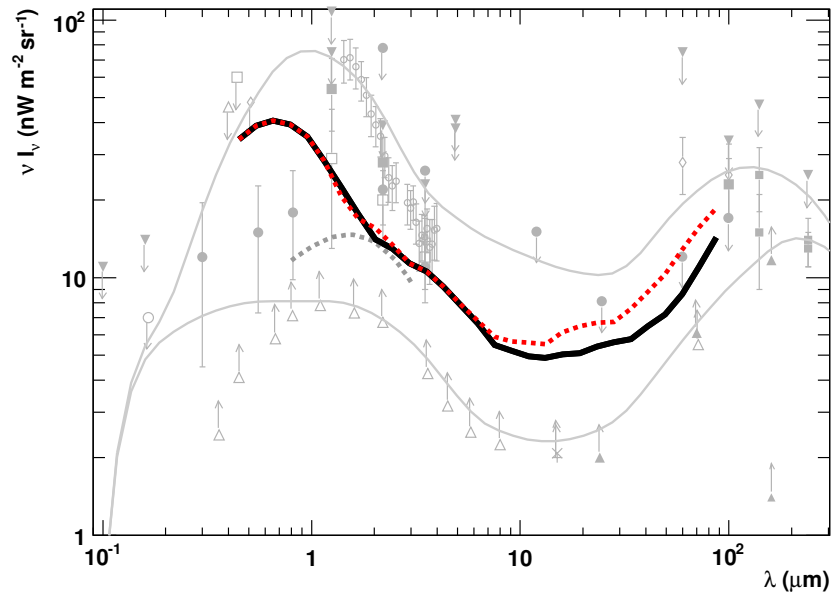


FIGURE 3.23: EBL limit derived from the *realistic* scan (black solid curve) in comparison to the EBL limit derived for a *realistic* scan utilizing the energy spectra from Mkn 501, H 1426+428 and 1ES 1101-232 shifted by 15% to lower energies (red dashed curve) to account for uncertainties in the energy scale of IACTs.

### 3.11 Summary and Conclusions

In this Paper we present a new method to constrain the density of the extragalactic background light (EBL) in the optical to far-infrared wavelength regime using VHE spectra of TeV blazars. We derive strong upper limits, which are only a factor 2 to 3 higher than the lower limits determined from source counts. Unlike many previous studies of this kind, we do not use one or a few pre-defined EBL shapes or models, but rather utilize a scan on a grid in EBL density vs. wavelength. This grid covers wavelengths from  $0.1 \mu\text{m}$  to  $1000 \mu\text{m}$  and spans in EBL density from the lower limits from source counts to the upper limits determined by direct measurements and fluctuation analyses. By iterating over all scan points we test a large set of different EBL shapes (8064000 in total). Each EBL shape is described by a spline function, which allows us to calculate the optical depth of VHE  $\gamma$ -rays for this shape via a simple summation instead of solving three integrals numerically. The resolution of the scan for sharp bumps or dips in the EBL is limited by the choice of the grid and the order of the spline.

To test these EBL shapes, we use the measured VHE  $\gamma$ -ray spectra from distant sources, which carry an imprint of the EBL from attenuation via pair production. We included spectra from all known TeV blazars (13 in total), making this the most complete study of this type to this date. All spectra are scrutinized with the same robust algorithm: For each spectrum and each EBL shape the intrinsic spectrum is calculated and an analytical description of the intrinsic spectrum is determined by fitting several functions. The fit parameters and errors of the functions are subsequently used to evaluate whether the intrinsic spectrum is physically feasible. We use two conservative criteria from the theory of VHE  $\gamma$ -ray emission in TeV blazars: The EBL shape is excluded if (i) a part of the intrinsic spectrum is harder than a theoretical limit or (ii) the intrinsic spectrum shows a significant pile-up at high energies. Since there is some spread in the predictions from theory, we included two independent scans for two theoretical limits on the hardness of the spectrum: (1) the *realistic* case for a photon index of  $\Gamma > 1.5$  and (2) the *extreme* case with  $\Gamma > 2/3$ .

We present limits derived from individual VHE  $\gamma$ -ray spectra. The strongest constraint results from the 1ES 1101-232 spectrum in the wavelength range from  $0.8$  and  $10 \mu\text{m}$ , mainly due to the hard spectrum and its large distance to Earth. An extragalactic origin of the claimed excess in the NIR between  $1$  and  $2 \mu\text{m}$  (Matsumoto *et al.* 2005) can be excluded even by the *extreme* scan. This result confirms the results from the recent publication of Aharonian *et al.* (2006b). In the FIR ( $20$  and  $80 \mu\text{m}$ ), strong upper limits are provided by the nearby TeV blazar Mkn 501. H 1426+428, situated at an intermediate distance, provides some constraints on the EBL density in the MIR (between  $1$  and  $15 \mu\text{m}$ ), connecting the upper limits derived from 1ES 1101-232 and Mkn 501. Most of the other spectra provide constraints in certain wavelength ranges, but they are not as strong as the limits from the previously described sources.

By combining the results from all spectra, we find that the upper limits become much stronger compared to the limits derived for individual spectra, especially in the wavelength range between  $4$  and  $60 \mu\text{m}$ . In the wavelength region from  $2$  to  $80 \mu\text{m}$  the combined limit for the *realistic* case lies below the upper limits derived from fluctuation analyses of the direct measurements (Kashlinsky & Odenwald 2000) and is just a factor of 2 to 2.5 above the absolute lower limits from source counts. This makes it the most constraining limit in the MIR to FIR region so far. As expected, the upper limits from the *extreme* scan are less constraining (factor of 2.5 to 3.5 above the lower limit from

source counts), but still constraining over this wide wavelength range.

The derived upper limits can be interpreted in two different ways:

1. The EBL density in the optical to FIR is significantly lower than suggested by direct measurements and the actual EBL level seems to be close to the existing lower limits. It can be hence concluded that experiments like HST, ISO, and Spitzer resolve most of the sources in the universe. This would indicate that there is very little room left for a significant contribution of heavy and bright Population III stars to the EBL density in this wavelength region.
2. The assumptions used for this study are not correct. This would require a revision of the current understanding of TeV blazar physics and models, which has been fairly successful in modeling multi-wavelength data from the radio to the VHE for all detected sources so far.

The strong constraints derived in this paper only allow for a low level of the EBL in the optical to the far-infrared, suggesting that the universe is more transparent to VHE  $\gamma$ -rays than previously assumed. Hence, we expect detections of many new extragalactic VHE sources in the next few years. Further multi-wavelength studies of TeV blazars will improve the understanding of the underlying physics, which will help to refine the exclusion criteria for the VHE spectra in these kinds of studies. The upcoming GLAST satellite experiment, operating in an energy range from 0.1 up to  $\sim 100$  GeV, will allow to extend such studies of the EBL to the ultraviolet to optical wavelength region.

## Chapter 4

# Discovery of VHE $\gamma$ -rays from the distant High Frequency Peaked BL Lac 1ES 0347-121

### 4.1 Introduction

Active galactic nuclei (AGN) are extreme environments: They are very luminous over a broad wavelength range from radio to very high energies (VHE). Some AGN show outbursts with large flux variations on time-scales down to a few minutes linked to relativistic processes connected with very high energy particles. So far, AGN are the only extragalactic objects, which have been detected in VHE  $\gamma$ -rays.

In this Chapter the discovery of VHE  $\gamma$ -ray emission from the BL Lac 1ES 0347-121 with the H.E.S.S. Cherenkov telescopes is reported and its implication for the extragalactic background light (EBL) are discussed. The X-ray data from the SWIFT satellite utilized in this Chapter has been analyzed by Dieter Horns<sup>1</sup> (Horns 2007).

### 4.2 Active Galactic Nuclei (AGN)

Historically, the celestial objects now grouped under the label active galactic nuclei (AGN) have been detected and classified into many different source types, depending on the wavelength band they have been discovered in or on spectral (and sometimes temporal) features. Today, AGN are characterized as the compact cores of a galaxy showing extremely bright emission over a broad wavelength range, often outshining the underlying host galaxy.<sup>2</sup>

In the current standard paradigm for AGN (Urry & Padovani (1995), illustrated in Fig. 4.1), the intense electro-magnetic emission from AGN is powered by a super-massive black hole (SMBH) with masses ranging from  $\sim 10^6$  to  $\sim 10^{10} M_{\odot}$  situated in the center of a galaxy.<sup>3</sup> The SMBH is surrounded by an accretion disk, which feeds new material to the SMBH. A dust torus encloses the inner system, which emits radi-

---

<sup>1</sup>Institut für Astronomie und Astrophysik, Universität Tübingen, Sand 1, D 72076 Tübingen, Germany

<sup>2</sup>There is some discussion, whether most galaxies harbor super-massive black holes (also our own galaxy) which go through a phase of activity, resulting in an AGN.

<sup>3</sup> $M_{\odot}$  denoted the mass of our sun =  $1.98844 \times 10^{30}$  kg.

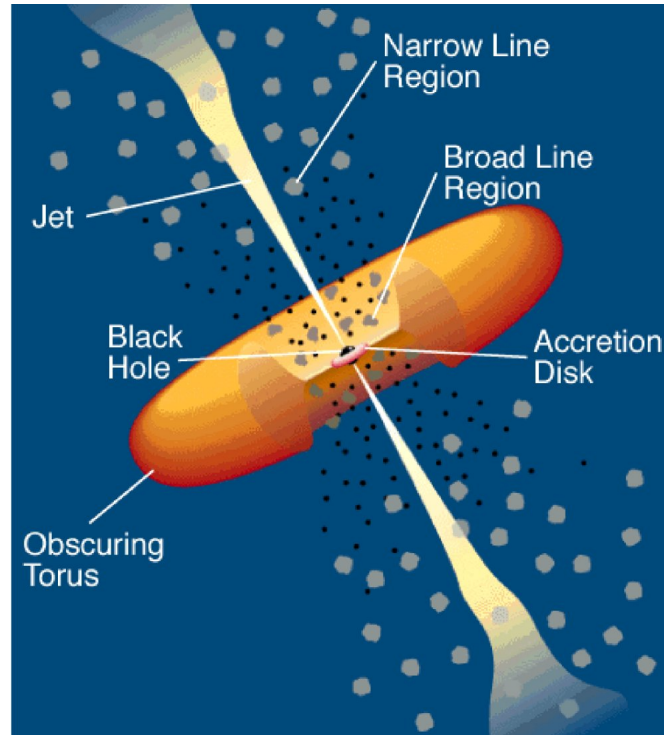


FIGURE 4.1: Schematic view of an active galactic nucleus (AGN) in the standard model (Urry & Padovani 1995).

ation in the infrared and can obscure the view on the central engine (depending on the observation angle). From the vicinity of the SMBH relativistic particle streams (jets) can emerge perpendicular to the accretion disk, reaching out to wide distances (up to several Mpc). Broad and narrow emission lines have been observed, which are attributed to emission regions close and far from the SMBH.

The jets emit polarized radio emission, which is commonly interpreted as synchrotron radiation from relativistic electrons. Moreover, apparent super-luminal motion (faster-than-light) of substructures (compact emission regions in the jet, knots) has been observed in several resolved jets (e.g. Pohl *et al.* (1995); Barthel *et al.* (1995); Piner & Kingham (1997)), which is direct evidence for the relativistic bulk motion in the jets. X-ray emission from the accretion disk and from the jet is frequently observed.

Depending on the relative orientation of the system with respect to the observer, different emission regions dominate the energy spectrum. For example, an AGN with a dust torus and jets viewed sideways will mainly radiate in the infrared, but the jets will be visible (depending on the energetics and the surrounding) in many wavelength bands from the radio to X-rays.

For VHE  $\gamma$ -ray astronomy the AGN sub-class of BL Lac objects is especially important: BL Lac objects, named after the first source of this type that has been discovered *BL Lacertae*<sup>4</sup>, are AGN with the jet pointing close to the line of sight of the observer. They show extremely variable emission in most wavelength bands and on short times-scales, which is attributed to emission processes connected to the relativistic jets. Depending

<sup>4</sup>Recently also discovered in VHE  $\gamma$ -rays (Albert *et al.* 2007b).

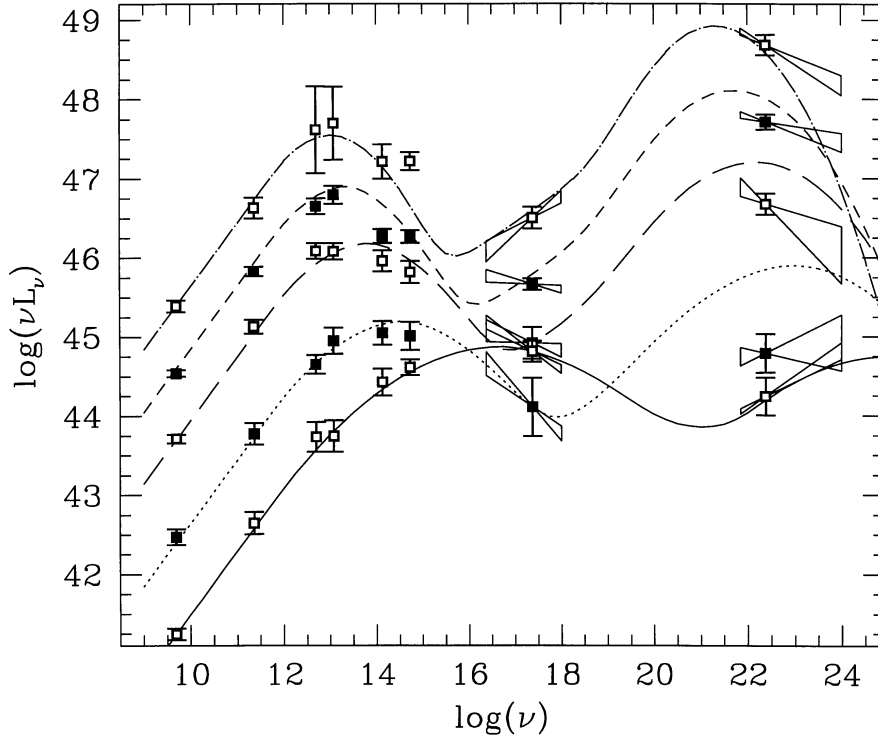


FIGURE 4.2: Average spectral energy distributions (SED) for different types of BL Lacs (binned according to the radio luminosity) from radio to GeV energies. The position of the first peak in the SED (synchrotron) shifts from UV to X-rays, the second peak (inverse Compton) from sub-GeV to VHE (from top to bottom). (Fossati *et al.* 1998)

on the position of the first peak of the broadband spectral energy distribution (SED) they are classified as either low frequency peaked BL Lac (peak in the UV/optical, LBL Lac) or high-frequency peaked BL Lac (peak in the X-rays, HBL Lac). This classification is more historic, since there is a smooth transition between the two classes. In Fig. 4.2 several averaged BL Lac SEDs are shown, binned according to their radio luminosity. One can see the smooth transition from LBL Lac (top) to HBL Lac (bottom) (Fossati *et al.* 1998; Costamante *et al.* 2001).

All known extragalactic sources of VHE  $\gamma$ -ray emission, with the exception of the radio galaxy M87, belong to the class of BL Lac, which are then called TeV blazars. The importance of the jets for VHE  $\gamma$ -ray emission is discussed in the following Section.

### 4.3 Models for VHE $\gamma$ -ray emission in TeV blazars

A key ingredient for VHE  $\gamma$ -ray emission models in TeV blazars is the relativistic movement of the emission region in the jet, measured by the Lorentz factor of the bulk motion  $\Gamma = (1 - \beta^2)^{-1/2}$ , with  $\beta = v/c$ ,  $v$  the bulk velocity of the emission region and  $c$  the speed of light. If the jet has an angle  $\theta$  to the line of sight of the observer, the relativistic motion towards the observer can be expressed by the Doppler factor  $\delta = 1/(\Gamma \cdot (1 - \beta \cos \theta))$ . The bulk motion Doppler-boosts the emitted photons to higher energies and thereby dramatically enhances the observed flux ( $\propto \delta^4$ , relativis-

tic beaming). Furthermore the constraint on the size of the emission region  $R$  from measurements of the characteristic time-scale  $t_{var}$  are relaxed:  $R = \delta c \cdot t_{var}$ .

As for most sources of VHE  $\gamma$ -rays, the models for VHE  $\gamma$ -ray production in AGN can broadly be divided into two categories: leptonic and hadronic models (see Sect. 2.3). So far the most popular, very simple and very successful model is the synchrotron self-Compton (SSC) leptonic model (Jones *et al.* 1974; Konigl 1981). While a large part of the available TeV blazar data is still well explained by such a simple SSC model, there is a growing amount of observational evidence, that a more complex model is needed.

### 4.3.1 Leptonic Models (EC, SSC)

In leptonic models a highly relativistic and compact electron population accelerated in the inner parts of the jet is considered, moving down the jet with bulk Lorentz factor  $\Gamma$ . These electrons can interact with different photon fields via inverse Compton (IC) scattering producing VHE  $\gamma$ -rays. In principle, different acceleration mechanisms for the electrons are possible, but mostly acceleration in shock fronts (Fermi I) is assumed.

In the external Compton (EC) model, the electrons interact with photons from the accretion disk (Dermer *et al.* 1992), re-scattered accretion disk photons (Sikora *et al.* 1994) or photons from the cosmic microwave background (CMB). In the synchrotron self Compton (SSC) model the electrons produce synchrotron radiation in a random magnetic field and then IC up-scatter the synchrotron photons to very high energies (Jones *et al.* 1974; Konigl 1981; Maraschi *et al.* 1992; Bloom & Marscher 1996). The result is a double humped spectral energy distribution with a synchrotron bump in the optical to X-ray region and an IC bump in the hard X-ray to VHE region. The peak positions are coupled and depend mainly on the properties of the underlying electron population, the Doppler factor and the magnetic field. If only one emission region is assumed and the electron population is homogeneous the model is called *homogeneous one-zone SSC* model. If several emission regions are considered, usually assumed to be independent from each other, the model is labeled *multi-zone SSC* model. One can combine the EC and SSC model by adding external photon fields to the SSC model.

The *homogeneous one-zone SSC* model has been very successfully utilized to describe the multi-wavelength data from different TeV blazars (e.g. Krawczynski *et al.* 2000, 2001; Aharonian *et al.* 2005d; Albert *et al.* 2006c). Due to the close coupling of the synchrotron and the inverse Compton photons through the same electron population, a close correlation between the two emission components is expected.<sup>5</sup> Such a correlation has been detected for the source Mkn 421 and Mkn 501 (Buckley *et al.* 1996; Aharonian *et al.* 1999a; Błażejowski *et al.* 2005; Albert *et al.* 2006c, 2007c).

In general, leptonic models naturally provide many of the features observed in TeV blazars. A few observations challenge the leptonic models, like the *orphan* VHE  $\gamma$ -ray flare observed with the Whipple telescope from 1ES 1959+650 (Krawczynski *et al.* 2004), which was not accompanied by a X-ray flare, and the unusually hard spectra of distant TeV blazars discovered with the H.E.S.S. instrument (Aharonian *et al.* 2006b,c).

More complex leptonic models have already been envisaged to account for some of these difficulties (e.g. Georganopoulos & Kazanas (2003); Katarzyński *et al.* (2006); Kusunose & Takahara (2006)).

<sup>5</sup>The need for correlation can be relaxed by invoking several independent emission regions responsible for the different parts of the energy spectrum.

### 4.3.2 Hadronic Models

In hadronic models a relativistic proton population in the jets is considered. In proton-photon interactions (photo-meson production) secondary electrons and positrons are produced from pion decays (e.g.  $\pi^- \rightarrow \mu^- \bar{\nu}_\mu$ ,  $\mu^- \rightarrow e^- \bar{\nu}_e \nu_\mu$ ,  $\pi^0 \rightarrow \gamma\gamma \rightarrow e^+e^- \dots$ ) (Mannheim & Biermann 1989). These electrons and positrons can initiate further electro-magnetic cascades (Mannheim 1993). The electro-magnetic emission is produced by the secondary particles via synchrotron radiation and inverse Compton scattering of the synchrotron radiation. Another possibility are proton-proton interactions of a proton beam moving through compact matter clouds, producing  $\pi^0$ s and VHE  $\gamma$ -rays via  $\pi^0 \rightarrow \gamma\gamma$  decay (Dar & Laor 1997; Beall & Bednarek 1999; Pohl & Schlickeiser 2000). Furthermore, VHE  $\gamma$ -rays can directly be produced through synchrotron radiation of very high energy protons (Aharonian 2000). In the proton synchrotron blazar model (Mücke & Protheroe 2001) components of several different models are combined: a co-acceleration of protons and electrons is assumed, the low energy radiation is produced by synchrotron emission of the electrons, the high energy part comes from direct synchrotron emission from high energy protons or from synchrotron radiation of secondary particles ( $\mu$ s,  $\pi$ s, etc.). Of course, such a complex model has more free parameters than the simple SSC model and gives some flexibility to describe the spectral energy distribution sufficiently.

The more complex hadronic models are able to reproduce the observed properties of TeV blazars, though generally more fine tuning of the parameters is needed than in the simple SSC model (high magnetic fields, very high energy protons, high Doppler factors, etc.).

One key to differentiate between hadronic and leptonic TeV blazar models lies in the neutrino component, which can only arise in hadronic models. Future observations with neutrino telescopes like ICECUBE (Karle *et al.* 2003) or KM3NET (Katz 2006) will help to constrain or, in case of a positive detection, confirm the hadronic models. Another way to differentiate between leptonic and hadronic models is the spectral shape and intensity of the  $\gamma$ -ray radiation in the GeV region, which will be probed by the upcoming GLAST satellite with high sensitivity.

## 4.4 Extragalactic VHE $\gamma$ -ray Sources: Status of Observation

Since the discovery of the first TeV blazar Mkn 421 in 1992 (Punch *et al.* 1992) the number of detected extragalactic VHE  $\gamma$ -ray sources has steadily grown. With the new generation of IACT experiments H.E.S.S. and MAGIC, the number of known TeV blazars has more than doubled over the last three years. More distant objects have been discovered, pushing the maximum distance to a redshift of  $z \sim 0.2$ . A list of all known TeV blazars is shown in Table 4.1, spectral properties (VHE) of most sources can be found in Table 3.1 and Fig. 3.7 in Chapter 3.

For the understanding of the physics of TeV blazars, multi-wavelength (MWL) observations during states of high flux and strong variability (*flares*) are of great importance. Such MWL observations allow to thoroughly test the correlations between the different wavelength regions and help to disentangle the different emission components. Especially simultaneous X-ray observations allow for a more direct measurement of the particle population producing the photon emission. Very successful MWL

Source	Redshift	Experiment	Flare	Reference
Mkn 421	0.030	Whipple	X	Punch <i>et al.</i> (1992)
Mkn 501	0.034	Whipple	X	Quinn <i>et al.</i> (1996)
1ES 2344+514	0.044	Whipple	X	Catanese <i>et al.</i> (1998)
Mkn 180	0.045	MAGIC		Albert <i>et al.</i> (2006b)
1ES 1959+650	0.047	HEGRA	X	Aharonian <i>et al.</i> (2003a); Götting (2007)
PKS 0548-322	0.069	H.E.S.S.		Aharonian <i>et al.</i> , in prep.
BL Lacertae	0.069	MAGIC		Albert <i>et al.</i> (2007b)
PKS 2005-489	0.071	H.E.S.S.		Aharonian <i>et al.</i> (2005c)
PKS 2155-304	0.116	Mark IV	X	Chadwick <i>et al.</i> (1999)
H 1426+428	0.129	Whipple		Horan & The VERITAS Col- laboration (2001)
1ES 0229+200	0.140	H.E.S.S.		Aharonian <i>et al.</i> , in prep.
H 2356-309	0.165	H.E.S.S.		Aharonian <i>et al.</i> (2006c)
1ES 1218+304	0.182	MAGIC		Albert <i>et al.</i> (2006a)
1ES 1101-232	0.186	H.E.S.S.		Aharonian <i>et al.</i> (2006b)
1ES 0347-121	0.188	H.E.S.S.		this work
PG 1553+113	?	H.E.S.S. MAGIC		Aharonian <i>et al.</i> (2006d), Albert <i>et al.</i> (2007a)

TABLE 4.1: Catalogue of known TeV blazars ordered by redshift. The discovery experiment and the corresponding reference are given. Sources with detected VHE  $\gamma$ -ray flaring states are also indicated.

campaigns have been conducted for Mkn 421 (Krawczynski *et al.* 2001; Błażejowski *et al.* 2005), Mkn 501 (Sambruna *et al.* 2000; Krawczynski *et al.* 2000; Kataoka *et al.* 1999), 1ES 1959+650 (Krawczynski *et al.* 2004), and PKS 2155-304 (Aharonian *et al.* 2005e). In 2006 PKS 2155-304 showed a strong VHE  $\gamma$ -ray flare (Benbow *et al.* 2006), with peak flux levels exceeding 10 times the flux of the Crab Nebula in the same energy range (the strongest constant VHE  $\gamma$ -ray source).

The radio galaxy M 87, discovered with the HEGRA experiment (Aharonian *et al.* 2003b) and confirmed by H.E.S.S. (Beilicke 2005; Aharonian *et al.* 2006e), is the first extragalactic VHE  $\gamma$ -ray source, which does not belong to the class of TeV blazars. M 87 is an AGN, but the jets are inclined to the line of sight of the observer with an angle  $\sim 30^\circ$ , so the Doppler boosting is presumably weaker than in TeV blazars. Surprisingly, VHE  $\gamma$ -ray variability on short time-scales in the order of days have been detected (Beilicke 2005; Aharonian *et al.* 2006e).

## 4.5 Discovery of VHE $\gamma$ -rays from 1ES 0347-121

### 4.5.1 The High Frequency Peaked BL Lac 1ES 0347-121

1ES 0347-121 was discovered in the Einstein Slew X-ray survey and was consecutively classified as an HB BL Lac object (Elvis *et al.* 1992; Schachter *et al.* 1993). Located at a redshift of  $z = 0.1880 \pm 0.0001$  it harbors a super massive black hole of mass  $10^{8.02 \pm 0.11} M_\odot$

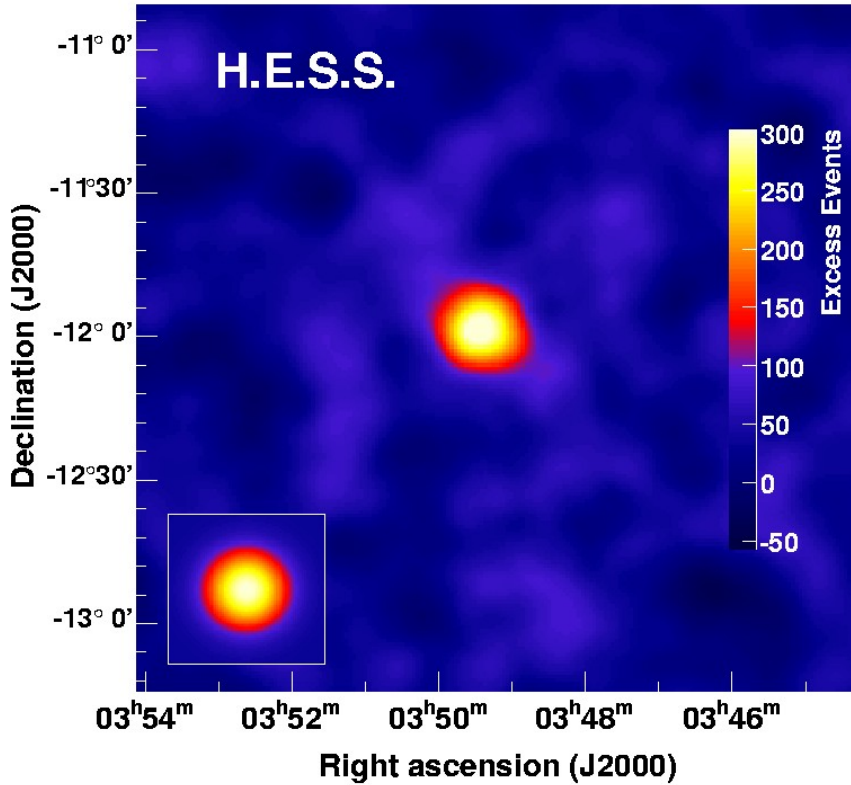


FIGURE 4.3: Correlated sky-plot of VHE  $\gamma$ -ray excess events centered on the position of 1ES 0347-121 (oversampling radius =  $0.122^\circ$ , smoothed). A clear excess is visible. The inlay in the lower left corner shows the excess distribution for a point-source derived from Monte Carlo data with the same zenith-angle and pointing offset distribution as the data.

(Woo *et al.* 2005).

An upper limit on the integral flux above an energy threshold of 1.46 TeV of  $5.14 \times 10^{-12} \text{ cm}^{-2} \text{ s}^{-1}$  (0.56 Crab) has been reported by the HEGRA collaboration (Tluczykont 2003; Aharonian *et al.* 2004b). Stecker *et al.* (1996) used simple physical considerations about the synchrotron and inverse compton component of the spectrum to calculate a prediction for the flux above 0.3 TeV of  $0.38 \times 10^{-11} \text{ cm}^{-2} \text{ s}^{-1}$ , which lies clearly below the upper limit reported by the HEGRA collaboration.

Here the discovery of VHE  $\gamma$ -rays with energies above 250 GeV from 1ES 0347-121 with the H.E.S.S. Cherenkov telescopes is reported.

#### 4.5.2 H.E.S.S. Dataset and Analysis Results

The H.E.S.S. observations of 1ES 0347-121 were carried out between August and December 2006. 25.4 h (corrected for the detector deadtime) of high quality data was recorded at zenith angles ranging from 12 to  $40^\circ$ , with a mean zenith angle of  $\sim 19^\circ$ . The analysis energy threshold for the observation is  $\sim 250$  GeV. The data was recorded in *wobble mode* with a pointing offset of  $0.5^\circ$  to the nominal source position to allow for simultaneous background estimation. The data has been analyzed with a standard

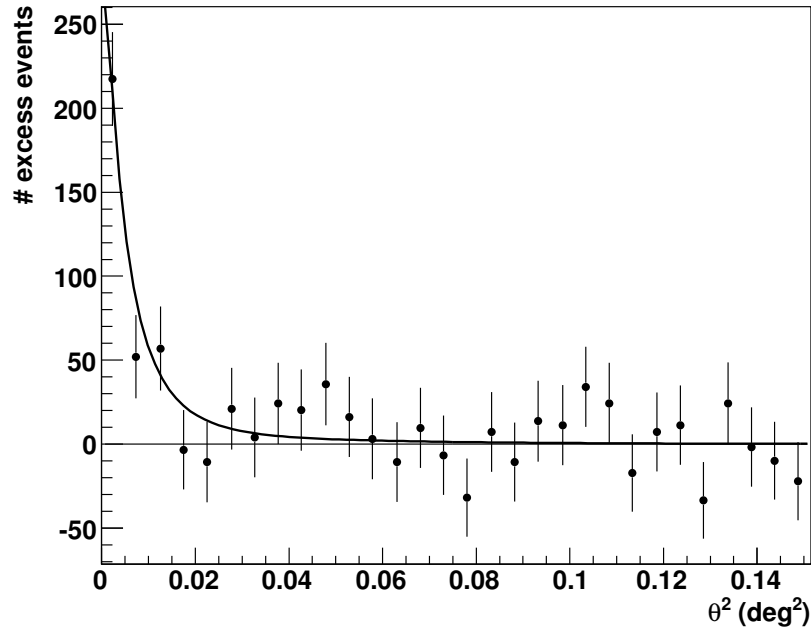


FIGURE 4.4: Number of excess events versus squared angular distance  $\theta^2$  to the nominal source position of 1ES 0347-121. A clear excess at the source position of 327  $\gamma$ -ray candidates ( $10.1\sigma$ ) has been detected. The solid line shows the expectation for a point source from Monte Carlo simulations for the same offsets and zenith angles, which is in very good agreement with the data.

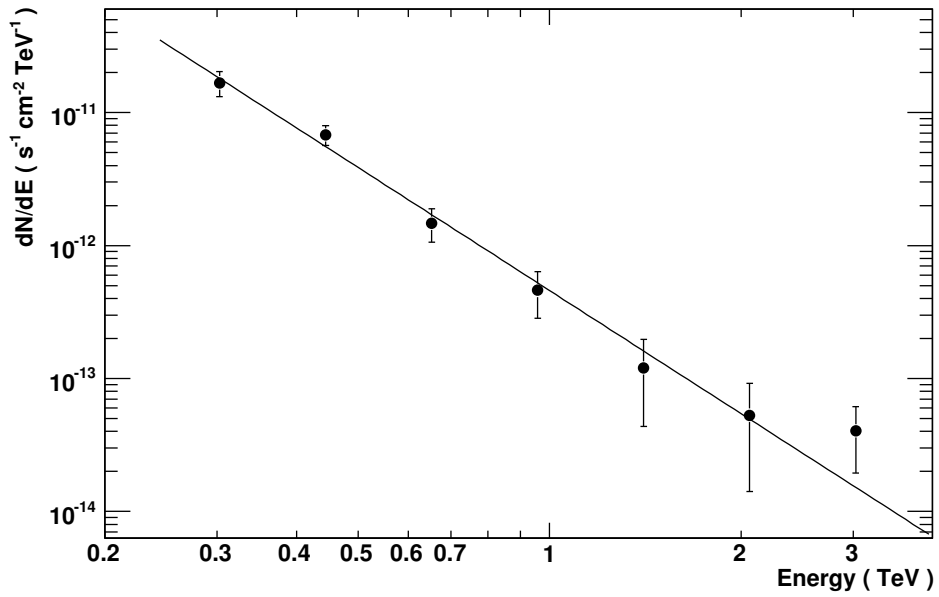


FIGURE 4.5: Differential energy spectrum of 1ES 0347-121. The spectrum is well described by a power law with a photon index of  $\Gamma = 3.08 \pm 0.23_{\text{stat}} \pm 0.1_{\text{sys}}$  (black line).

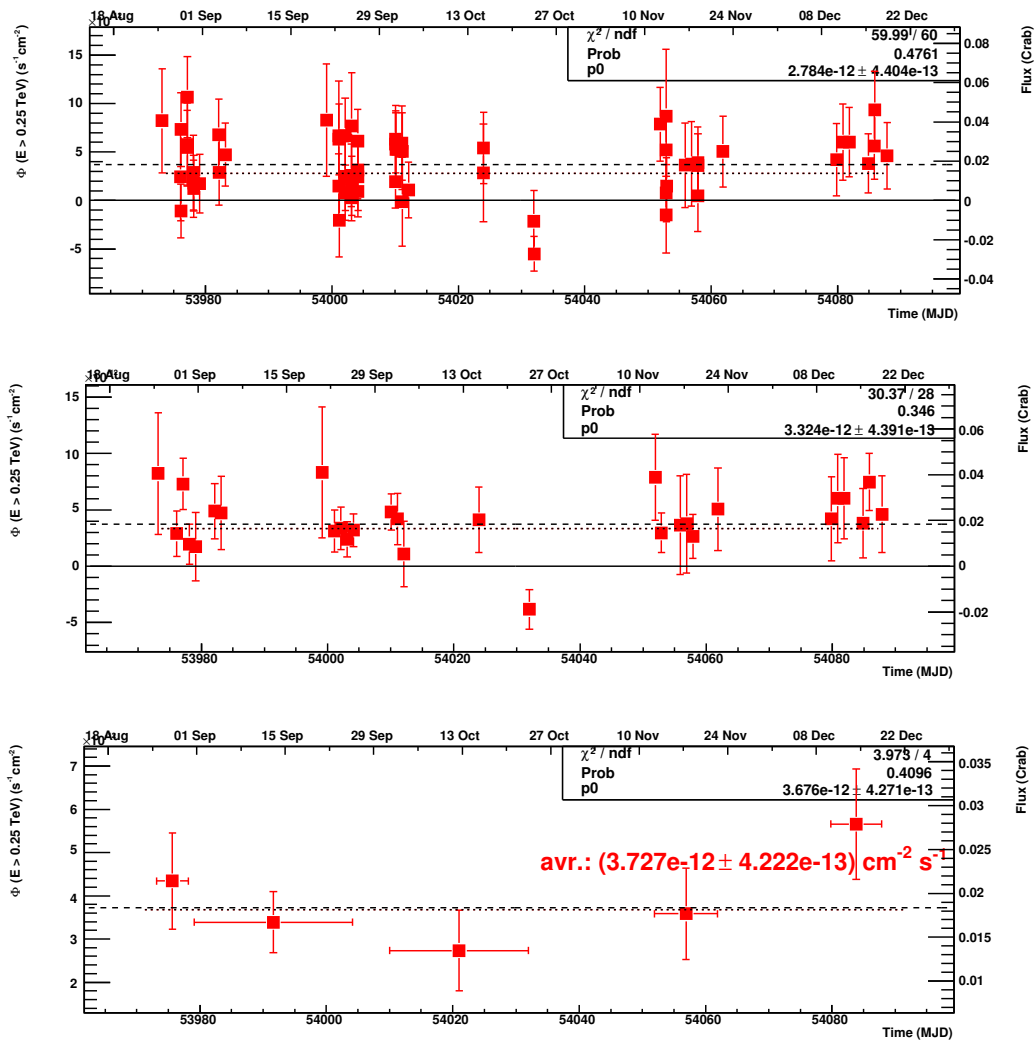


FIGURE 4.6: Integral flux of 1ES 0347-121 above an energy of 250 GeV versus time (lightcurve) for different time-scales. The dashed line marks the average integral flux (the value is given in the lower panel). The dotted line is a fit of constant flux to the data. The corresponding fit parameters are given in the box in upper right corner of each plot. The fit is good for all time-scales. *Upper Panel*: 28 min/run. *Middle Panel*: Nightly averaged. *Lower Panel*: Monthly averaged.

Hillas analysis as described in Aharonian *et al.* (2006h).

An excess of 327  $\gamma$ -ray candidates was found corresponding to a statistical significance of 10 standard deviations (Fig. 4.3 and 4.4). The extension of the excess is compatible with a point-source and the position of the excess coincides with the position reported for 1ES 0347-121. The differential energy spectrum of the source derived with the method described in Appendix A is shown in Fig. 4.5. It is well described ( $\chi^2/\text{d.o.f.} = 4.8/6$ ) by a power law  $dN/dE = \Phi_0 (E/1 \text{ TeV})^{-\Gamma}$  with a normalization  $\Phi_0 = (4.59 \pm 0.86_{\text{stat}} \pm 1.0_{\text{sys}}) \times 10^{-13} \text{ s}^{-1} \text{ cm}^{-2} \text{ TeV}^{-1}$  and a photon index  $\Gamma = 3.08 \pm 0.23_{\text{stat}} \pm 0.1_{\text{sys}}$ . The integral flux above 250 GeV taken from the spectral fit is  $\Phi(E > 250 \text{ GeV}) = (3.9 \pm 1.1) \times 10^{-12} \text{ s}^{-1} \text{ cm}^{-2}$ , which corresponds to  $\sim 2\%$  of the flux of the Crab Nebula above the same threshold (Aharonian *et al.* 2006h). A search for flux variability on different time-scales (run, night, month) has been performed, but no significant variability has been detected (Fig. 4.6).

### 4.5.3 SWIFT X-Ray and UV/O Data

The SWIFT satellite (Gehrels *et al.* 2004) carries three instruments for observations in different wavelength bands: The main instrument is the Burst Alert Telescope (BAT). It covers energies in the range from 15 – 150 keV and has a wide field of view for the discovery of gamma ray bursts (GRB). It is accompanied by the X-Ray Telescope (XRT) for energies in the range from 0.3 to 8 keV and the UltraViolet/Optical Telescope (UVOT) for wavelengths from 170 to 650 nm. In this analysis data from the XRT and the UVOT instrument are used (there was no positive detection in the BAT instrument).

SWIFT observation of 1ES 0347-121 were carried out on October 3rd, 2006, roughly in the middle of the H.E.S.S. observation period. 3.2 ksec of screened data in photon counting mode have been analyzed (Horns 2007). For the analysis of Swift XRT and UVOT data the HEASOFT 6.2<sup>6</sup> package with xspec11 and the latest calibration (XRT: 2007-03-30, UVOT: 2006-11-16) were used.

The XRT data were reprocessed with the updated calibration tables including new bad pixel tables. In order to avoid pile-up in the energy spectrum, the extraction region was chosen to be an annulus with an inner radius of 5 pixel and an outer radius of 30 pixels (pixel width/height corresponds to 2.3"). The background spectrum was accumulated in a wider annulus (inner radius of 45 pixels, outer radius of 90 pixels). The auxiliary response file was created with the standard tool `xrtmkarf` including pointspread function correction. Together with the canned response matrix `swxpc0to12_20010101v008.rmf`, two different spectral models including photoelectric absorption fixed to the Galactic value of  $n_H = 3.6 \times 10^{20} \text{ cm}^{-2}$  have been forward folded and fit to the data between 0.3 and 8 keV: a pure power law model results in an acceptable  $\chi^2/\text{d.o.f.} = 109.5/107 = 1.02$  fit with  $\Gamma = 1.98 \pm 0.06$  at 90% c.l. However, the residuals indicate a spectral break with a softening above  $\approx 2$  keV. Fitting a broken power law results in a marginal but negligible improvement of the fit with  $\chi^2/\text{d.o.f.} = 98.4/105 = 0.94$  with  $\Gamma_1 = 1.71_{-0.62}^{+0.17}$ ,  $\Gamma_2 = 2.19_{-0.15}^{+0.21}$ , and  $E_{\text{br}} = 1.2_{-0.5}^{+0.8}$  keV. For the broken power law model, the unabsorbed integrated energy flux between 2 and 10 keV is  $f_{2-10} = 2.2 \times 10^{-11} \text{ ergs cm}^{-2} \text{ s}^{-1}$ .

The UVOT observations covered 6 filter settings. Since the light curves indicate no variability for the different exposures, the exposures for the individual filter wheel

<sup>6</sup><http://heasarc.nasa.gov/lheasoft/>

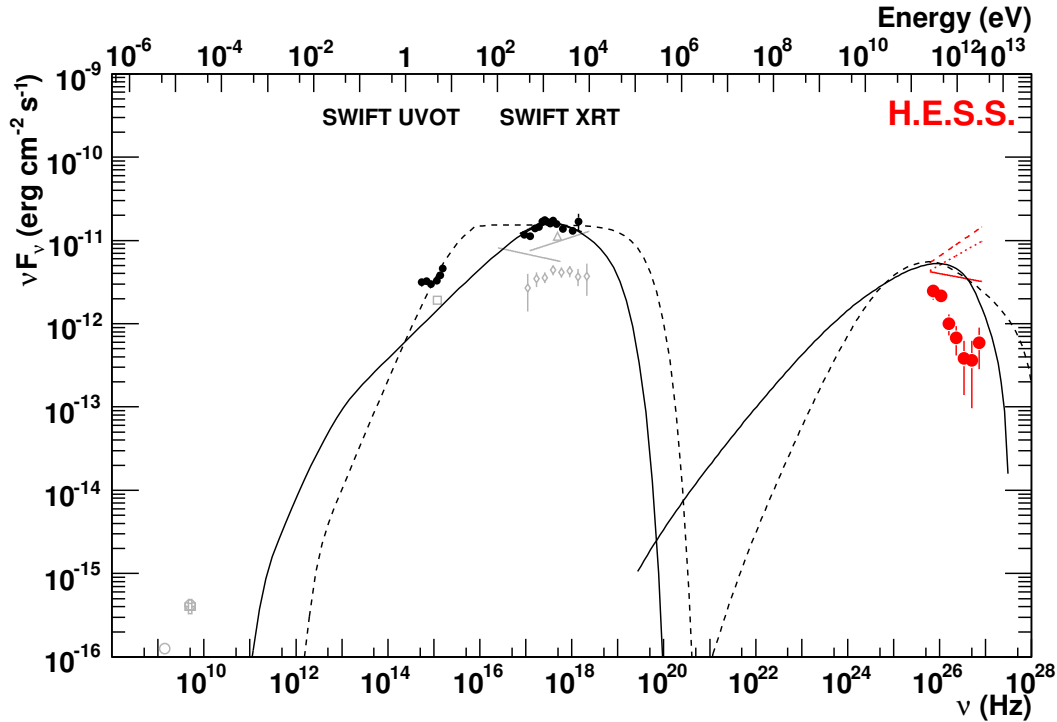


FIGURE 4.7: Broadband spectral energy distribution (SED) of 1ES 0347-121 ranging from radio to VHE. H.E.S.S. (red markers, left) and SWIFT (black markers, center) data are shown. Red lines denote the intrinsic VHE  $\gamma$ -ray spectrum after correction for attenuation by the extragalactic background light (see text for details). Grey markers and lines in the background are archival data (Elvis *et al.* 1992; Schachter *et al.* 1993; Perlman *et al.* 1996; Lamer *et al.* 1996; Wolter *et al.* 1998; Giroletti *et al.* 2004; Perlman *et al.* 2005). The curves (solid/dashed) are simple synchrotron self Compton (SSC) models calculated with the code from Krawczynski *et al.* (2004).

settings have been co-added. The aperture was chosen to be 12 pixels for the optical filters while it was increased to 24 pixels for the UV filters. For the UV filter images, a 6 pixel radius region centered on a faint stellar source 12 arc sec north of 1ES 0347-121 was excluded, falling into the wider 24 pixel aperture. The aperture photometry includes pile up correction and a flux obtained using the zero point values quoted in the calibration notes of the Swift UVOT team. Finally, the observed flux values were corrected for galactic absorption using a reddening of  $E(B - V) = 0.047$  which is then scaled to obtain  $A_\lambda$  for the Swift filters following the recipe given by Giommi *et al.* (2006). The resulting data points are shown in Fig. 4.7 as black markers.

#### 4.5.4 Spectral Energy Distribution and Modeling

The spectral energy distribution (SED) of 1ES 0347-121 ranging from radio to VHE is shown in Fig. 4.7. VHE  $\gamma$ -rays are attenuated by the extragalactic background light (EBL), which has to be taken into account when modeling the intrinsic spectrum. To calculate the intrinsic VHE spectrum the following EBL models or shapes have been utilized: Primack *et al.* (2005), Kneiske *et al.* (2002) low model, and P0.45 shape from

	Model A	Model B
$K$ ( $\text{cm}^{-3}$ )	$5.5 \times 10^2$	$4.5 \times 10^7$
$R$ (cm)	$1. \times 10^{16}$	$1 \times 10^{16}$
$B$ (G)	$7. \times 10^{-2}$	$3. \times 10^{-2}$
$\gamma_{\min}$	$1 \times 10^3$	$2.05 \times 10^4$
$\gamma_{\max}$	$1 \times 10^8$	$2 \times 10^6$
$\gamma_{\text{break}}$	$2 \times 10^5$	–
$\delta$	25	60
$n_1$	1.9	3.
$n_2$	3.5	–

TABLE 4.2: Parameters of the synchrotron self Compton (SSC) models shown in Fig. 4.7. Model A: solid curves; Model B: dashed curves.

Aharonian *et al.* (2006b). All three models have a rather low EBL density in the optical to NIR. Fits of a power-law function to the resulting intrinsic VHE photon spectra are shown in Fig. 4.7 as red lines above the H.E.S.S. measured spectrum (from bottom to top): solid line - Primack *et al.* (2005), dotted line - Kneiske *et al.* (2002) low model, and dashed line - P0.45 shape from Aharonian *et al.* (2006b). Because the exact EBL shape is not known, the intrinsic spectra have a rather wide spread, but the overall flux level at VHE energies and the spectral forms are constraint.

A simple homogeneous one-zone synchrotron self Compton (SSC) model (code from Krawczynski *et al.* (2004)) is used to describe the X-ray and the intrinsic VHE data. The model is determined by a set of 9 parameters: A spherical emission region with radius  $R$  moving towards the observer with a Doppler factor  $\delta$  is assumed. The emission region is filled with (1) a homogeneous random magnetic field with strength  $B$  and (2) an electron population with  $\gamma = E/(m_e c^2)$  ( $E$  the electron energy,  $m_e$  the electron mass, and  $c$  the speed of light) following an energy density distribution  $N(\gamma)$ . The energy density distribution of the electron population follows a broken power law from  $\gamma_{\min}$  to  $\gamma_{\max}$  with index  $n_1$  ( $N(\gamma) = K\gamma^{-n_1}$ ) below and  $n_2$  ( $N(\gamma) = K\gamma_{\text{break}}^{n_2-n_1}\gamma^{-n_2}$ ) above the break  $\gamma_{\text{break}}$  with an overall normalization  $K$ .

Parameter-sets describing the overall intrinsic spectral shape can be found (Tab. 4.2, fitted to X-ray and intrinsic VHE data), but some problems remain: fixing the electron population with the X-ray (synchrotron) peak at  $\sim 1$  keV (Model A, solid curve) makes it hard to construct an inverse Compton peak with peak energy  $> 3$  TeV, which is implied by two of the EBL models utilized. Taking the X-ray data as a simple power law requires a rather high low energy cut-off  $\gamma_{\min}$  in the electron population to not overproduce the UV/optical flux (Model B, dashed curve) and with an X-ray slope  $n_1 \sim 2$  it is again difficult to shift the IC peak to high enough energies. One way to overcome this problem is to assume a non-standard mono-energetic (or narrow banded) electron distribution and use the low energy cut-off of the electron distribution to create a pile-up at TeV energies (Katarzyński *et al.* 2006). Furthermore, the measured X-ray and VHE data have not such high statistics and are therefore not overly constraining. It is possible to e.g. construct models, which do not follow the derived spectral form in the X-ray band, but still result in a statistical good fit ( $\chi_{\text{red}}^2 \sim 1$ ). Deeper simultaneous X-ray and VHE observations (preferably in a even higher flux state) are needed to derive stronger constraints on the model parameters.

### 4.5.5 Constraints on the EBL from the energy spectrum of 1ES 0347-121

As discussed extensively in Chapter 3, the VHE  $\gamma$ -ray spectra of distant objects can be used to set upper limits on the density of the extragalactic background light (EBL). 1ES 0347-121 is the most distant VHE  $\gamma$ -ray emitter discovered up to now and has a fairly hard energy spectrum, which makes it a good candidate to provide limits in the optical to near-infrared (NIR) wavelengths of the EBL.

Two methods will be used to derive limits on the EBL: (I) the method presented in the paper by Aharonian *et al.* (2006b) for the energy spectra of the HBL Lacs 1ES 1101-232 and H 2356-309 and (II) the method described in this work in Chapter 3.

#### 4.5.5.1 Limits on the EBL I - H.E.S.S. Nature paper technique

Aharonian *et al.* (2006b) used the VHE spectra of the recently discovered TeV Blazars 1ES 1101-232 and H 2356-309 to set very strong upper limits on the density of the EBL in the optical to NIR. For the derivation of the limit, a fixed *reference shape* for the EBL  $n_\epsilon(\epsilon)$  is assumed (Aharonian *et al.* 2003c). This shape is scaled in the overall EBL density with different scaling factors  $n'_\epsilon(\epsilon) = f \cdot n_\epsilon(\epsilon)$  (Fig. 4.8 top panel). For each scaled shape, the corresponding intrinsic energy spectrum is calculated and fitted by a power law  $dN/dE = \Phi_0 \cdot (E/1 \text{ TeV})^{-\Gamma}$ . As discussed in Sect. 3.7, intrinsic spectra exceeding a certain hardness are difficult to accommodate in the current standard paradigm for TeV blazars. In Aharonian *et al.* (2006b) EBL shapes resulting in intrinsic spectra with photon index  $\Gamma < 1.5$  are considered unrealistic, and the EBL shape corresponding to  $\Gamma = 1.5$  is taken as the limit. Since the evolution of the EBL is not considered in the calculation of the limit, the limit is relaxed by 0.1 in the scaling factor  $f$  to account for the effect of late emission (see Aharonian *et al.* (2006b) and Sect. 3.10 for details).

The intrinsic spectra of 1ES 0347-121 resulting from the scaled EBL shapes shown in Fig. 4.8 top panel are displayed in Fig. 4.8 middle panel. The shape has been scaled in 10 steps from  $f = 0.3$  to  $f = 1$ . The correlation between the scaling factor of the EBL shape  $f$  and the photon index of the intrinsic spectrum  $\Gamma$  is shown in Fig. 4.8 bottom panel. For the scale factors considered here (0.3 – 1), the correlation is well described by a linear function. The limiting value on the photon index  $\Gamma = 1.5$  is reached for a scaling factor of 0.51. Allowing for evolution of the EBL (as discussed above) this results in a limiting shape with scaling factor 0.61.

The limit derived on the EBL density from the energy spectrum of 1ES 0347-121 (labeled  $\text{Lim}_{\text{NEW}}$ ) in comparison to the limit derived in Aharonian *et al.* (2006b) for the energy spectrum of 1ES 1101-232 (scaling factor 0.45, resulting in a limit of 0.55 accounting for EBL evolution, labeled  $\text{Lim}_{\text{HESS}}$ ) is shown in Fig. 4.9. The  $\text{Lim}_{\text{NEW}}$  lies  $\sim 10\%$  higher than the  $\text{Lim}_{\text{HESS}}$ . The claimed excess of the EBL in near-infrared over the EBL level derived from source counts (Matsumoto *et al.* (2005), see Sect. 3.2 for a detailed discussion) is, as in the case of  $\text{Lim}_{\text{HESS}}$ , clearly excluded. The energy spectrum of 1ES 0347-121 therefore confirms the finding from Aharonian *et al.* (2006b).

To derive the limit on the EBL with this method, a fixed reference shape is used. Since more complex EBL shapes are possible, we will explore a larger set of EBL shapes with the EBL Scan method as presented in Chapter 3 in the following paragraph.

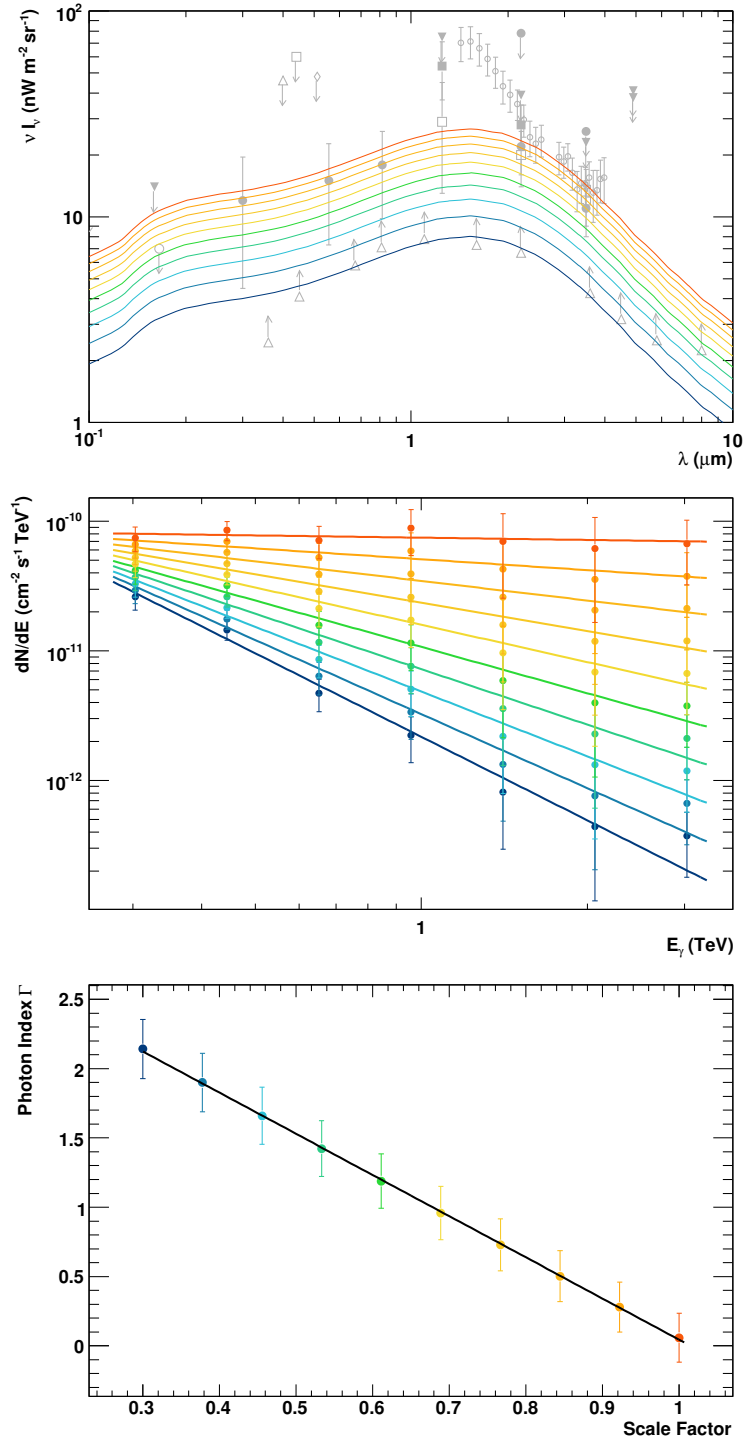


FIGURE 4.8: *Top Panel*: EBL shape AH03 scaled in 10 linear steps from  $f = 0.3$  to  $f = 1$  (lowest to highest shape, colored curves) overlaid on measurements and limits on the EBL (grey markers, Fig. 3.3). *Middle Panel*: Intrinsic differential energy spectra of 1ES 0347-121 after the correction for EBL attenuation from the scaled EBL shapes. The lines are fits of a power law  $dN/dE \sim E^{-\Gamma}$  to the spectra. The colors correspond to the colors of the EBL shapes in the top panel. *Bottom Panel*: Photon index  $\Gamma$  from a fit of a power law to the intrinsic spectra of 1ES 0347-121 versus the scaling factor of the EBL shape. The limiting value for the photon index of  $\Gamma = 1.5$  is reached for a scaling factor of 0.51.

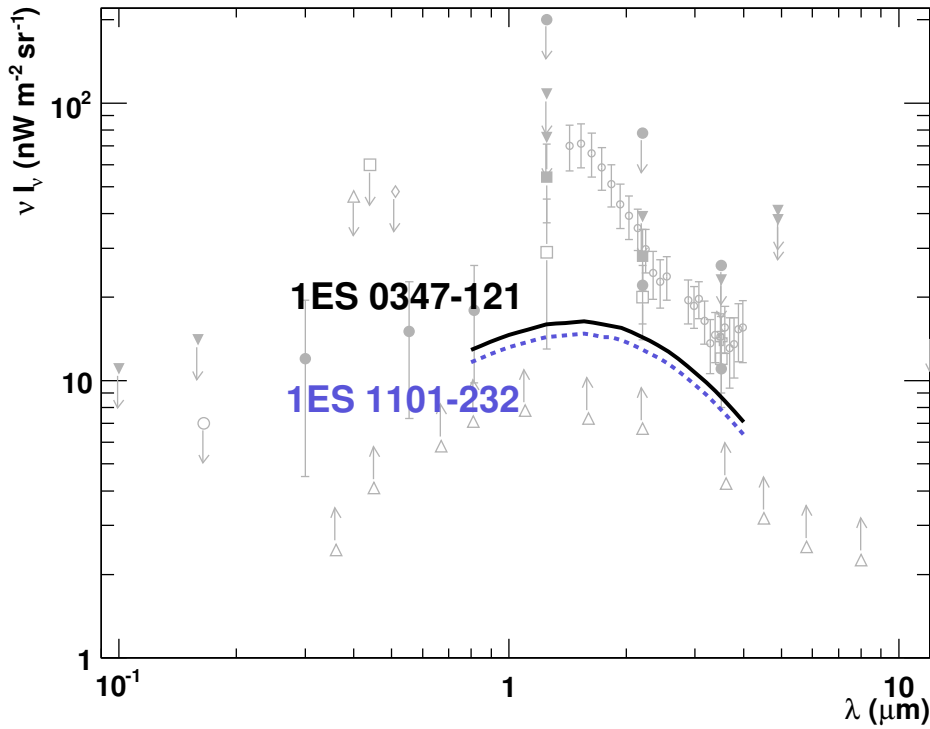


FIGURE 4.9: Limit on the EBL density derived with the method from Aharonian *et al.* (2006b) for the energy spectrum of 1ES 0347-121 (black curve, scaling factor 0.61) in comparison with the limit derived for the energy spectrum of 1ES 1101-232 (blue dashed curve, scaling factor 0.55). Grey markers are the limits and measurements from Fig. 3.3.

#### 4.5.5.2 Limits on the EBL II - EBL Scan method

In the EBL Scan method a large set of EBL shapes ( $> 8 \times 10^6$  different shapes) with different spectral features is tested if they result in a physical allowed intrinsic TeV blazar spectrum. The details of the method are described in Chapter 3.

For the realistic scan ( $\Gamma > 1.5$ ) with the 1ES 0347-121 spectrum 79.22% (6 388 278) off all shapes tested have been excluded. The limit on the EBL density is shown in Fig. 4.10 in comparison to the limit derived for the spectrum of 1ES 1101-232. For EBL wavelengths  $\lambda < 2 \mu\text{m}$  the two limits are comparable, with the 1ES 0347-121 limit being only a little less constraining. For  $\lambda > 2 \mu\text{m}$  the difference between the two limits widens. While the 1ES 0347-121 limit is only constraining up to  $\lambda \sim 6 \mu\text{m}$ , the 1ES 1101-232 limit reaches to wavelengths  $\lambda > 10 \mu\text{m}$ .

The distances of the two sources are very similar, but the energy spectra and especially the energy ranges of the measured spectra are different. While the 1ES 0347-121 spectrum is only slightly softer, its first flux point is at  $\sim 300 \text{ GeV}$  where the 1ES 1101-232 spectrum starts at  $\sim 180 \text{ GeV}$ . This results in a larger leverage between the lowest and the highest energies for the 1ES 1101-232 spectrum. In the wavelength range  $\lambda > 2 \mu\text{m}$  the EBL only affects the highest energies of the spectrum. The stronger leverage in the case of 1ES 1101-232 therefore results in harder intrinsic spectra and stronger limits.

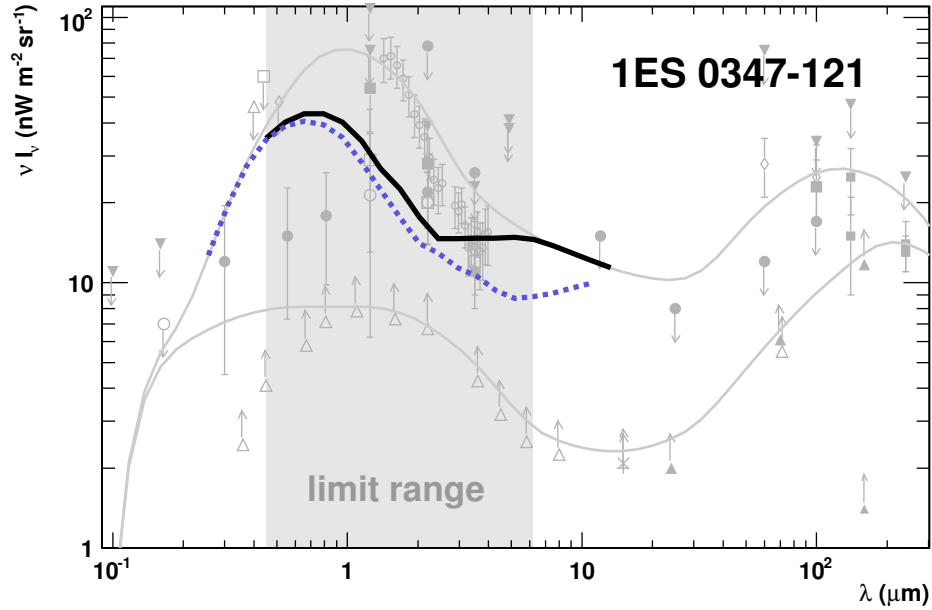


FIGURE 4.10: Limit on the EBL density derived with the method from Mazin & Raue (2007) *realistic* scan for the energy spectrum of 1ES 0347-121 (black curve) in comparison with the limit derived for the energy spectrum of 1ES 1101-232 (blue dashed curve). The length of the curves give the approximate sensitivity range of the spectra, the grey area marks the limit range of the limit derived from the 1ES 0347-121 spectrum. Grey markers are the limits and measurements from Fig. 3.3, grey curves mark the lowest and the highest shape tested in the scan.

Given that the individual limit from the 1ES 0347-121 energy spectrum is higher than the limit derived from the 1ES 1101-232 energy spectrum, the overall combined EBL limit will not improve by the inclusion of the 1ES 0347-121 spectrum.

## 4.6 Summary and Conclusions

In this Chapter the discovery of a new extragalactic source of VHE  $\gamma$ -rays, the BL Lac object 1ES 0347-121, was presented. With a redshift of  $z = 0.1880$  it is the farthest source of VHE  $\gamma$ -rays today. The energy spectrum was measured in the range from 250 GeV up to 3 TeV and is well described by a power law with photon index  $\Gamma \sim 3.1$ . A search for variability on different time-scales did not yield a positive result. Contemporary X-ray measurements by the SWIFT satellite were used to construct the broadband spectral energy distribution (SED). It is possible to describe the SED of 1ES 0347-121 with a simple synchrotron self Compton model, though the possible feature of an inverse Compton (IC) peak at energies  $> 3$  TeV, as implied by the intrinsic spectra derived for some models of the extragalactic background light, is somewhat challenging. The large distance of the source makes it an ideal target for studies of the EBL, which leaves an attenuation signature in the measured VHE spectra. Two different methods were used to derive constraints on the EBL: (1) The method presented in Aharonian *et al.* (2006b), which yielded a similar limit for the energy spectrum of 1ES 0347-121 as the strongest limit derived so far from the energy spectrum of 1ES 1101-232 and (2) the EBL Scan

method presented in Chapter 3. Overall the previously derived limits on the EBL in the optical to near-infrared could be confirmed, although the new limits are a little less constraining.

Since TeV blazars are source with highly variable emission, further continuous monitoring of 1ES 0347-121 in VHE  $\gamma$ -rays is highly desirable, to catch possible flaring states. Furthermore, a simultaneous multi-wavelength campaign with observations in radio, UV-optical and especially X-rays to record a high quality simultaneous SED would help to further constrain the models.

The growing sample of TeV blazars and will help to disentangle the intrinsic physics of the sources from the effects of the extragalactic background light and improve the understanding of very high energetic relativistic processes in the particle jets.



## Chapter 5

# Discovery of extended VHE $\gamma$ -ray Emission from the Direction of the Young Open Star Cluster Westerlund 2

### 5.1 Introduction

Young open star clusters have long been discussed as a possible contributor to the cosmic ray flux (Jokipii 1968; Casse & Paul 1980). The energetic winds of massive young stars can result in shock fronts (e.g. between winds from different stars or stellar wind and the surrounding material), which can produce relativistic particle populations and consequently VHE  $\gamma$ -rays as secondaries.

In this chapter the detection of extended VHE  $\gamma$ -ray emission from the direction of the young stellar cluster Westerlund 2 is reported. This work has been done in collaboration with Olaf Reimer<sup>1</sup> and has been partially published in Aharonian *et al.* (2007). Recently the paper and its implications have been discussed in Nature (Butt 2007).

### 5.2 VHE $\gamma$ -rays from Young Open Stellar Clusters

#### 5.2.1 Young Massive Stars and Stellar Winds

Stars come in a great variety of different types, mainly distinct by their spectral features. The most luminous and massive stars belong to the spectral classes O and B, with masses ranging from 10 to 100  $M_{\odot}$  and temperatures from 25 000 K to 45 000 K. Due to their massive nature they are short-lived. They can often be found in loose associations along the galactic plane (OB association, young open stellar clusters) frequently associated with giant gas or dust clouds, which are presumably left over material from a star formation cloud. Luminous stars usually ionize the surrounding medium and form H II regions (also called Strömgren spheres). (Maran 1992)

---

<sup>1</sup>Stanford University, HEPL & KIPAC, Stanford, CA 94305-4085, USA, olr@stanford.edu

**Stellar Winds** Stellar wind describes the phenomenon of a constantly expanding outer atmosphere of a star. It is common for many types of stars, e.g. for our Sun the mass loss rate from stellar winds is in the order of  $10^{-14} M_{\odot} \text{yr}^{-1}$ . For hot and luminous stars the mass loss rate can reach  $10^{-5} M_{\odot} \text{yr}^{-1}$ . The physics behind these winds is not yet fully understood, but it is believed that the wind is driven by radiation pressure amplified by resonance photon scattering at emission lines (e.g.  $\text{C}^{+3}$  at  $1550 \text{\AA}$ ). Other explanations for winds of cold stars include radiative forces on dust. (Maran 1992)

**Wolf-Rayet Stars** Wolf-Rayet (WR) stars are commonly thought to represent an evolved phase for the most massive stars in our Galaxy, however the most luminous hydrogen-rich WR stars may still be thought of as the most massive, main-sequence stars (Moffat *et al.* 2006), showing strong, broad emission lines at optical wavelengths. WR stars exhibit strong stellar winds and some WR stars are already established as non-thermal radio emitters, whereas claimed associations with  $\gamma$ -ray emission remain to be confirmed. It has been suggested that non-thermal radio emission observed in a significant fraction of the massive stars could be related to shocks in colliding winds in binaries (Dougherty & Williams 2000). An important question is therefore whether all massive stars which produce non-thermal radio emission are indeed binaries. Another relevant issue is whether the relativistic electrons which produce the observed non-thermal (synchrotron) radio emission also produce detectable (inverse Compton) high-energy  $\gamma$ -ray emission.

### 5.2.2 Stellar Winds and VHE $\gamma$ -rays

Several theoretical scenarios for VHE  $\gamma$ -ray production in connection with strong stellar winds exist, but so far no conclusive VHE  $\gamma$ -ray detection has been made.

**Internal and Termination Shocks** Early on, the termination shock of strong stellar winds in the surrounding medium has been discussed as a source of CRs and  $\gamma$ -rays. Völk & Forman (1982) pointed out, that particles only initially accelerated near the surface of a star e.g. by outbursts, would lose too much energy in the expanding wind to be relevant for the production of high energy photons or CRs in the termination shock. Cesarsky & Montmerle (1983) (and references therein) discussed the possibility of re-acceleration of particles in the wind cavities via internal shock fronts in turbulent plasma. This could lead to energetic particles at the termination shock and to production of VHE  $\gamma$ -rays inside the wind cavities. Turbulent winds with internal shocks could lead to VHE  $\gamma$ -rays from inverse Compton processes (White 1985; Chen & White 1991) or through  $\pi^0$  decays from hadronic interactions of high energetic ions with thermal ions (White & Chen 1992).

**Colliding Winds in Binaries** It has been suggested that in massive binary systems high-energy  $\gamma$ -rays are produced in the shock from the colliding winds either in hadronic emission scenarios, or by inverse Compton scattering of relativistic electrons with the dense photospheric stellar radiation fields (Eichler & Usov 1993; White & Chen 1995; Benaglia & Romero 2003; Reimer *et al.* 2006; Pittard & Dougherty 2006). In the former scenario,  $\gamma$ -rays are either directly produced in neutral pion decays, with the

mesons produced by inelastic interactions of relativistic nucleons with the wind material (White & Chen 1992; Benaglia & Romero 2003; Torres *et al.* 2004; Reimer *et al.* 2006; Pittard & Dougherty 2006), or alternatively are produced in cascade models (Bednarek 2005). Another possibility for  $\gamma$ -ray production comes from inverse-Compton pair cascades, which are initiated by high-energy neutral pion decay photons (from nucleon-nucleon interactions in the stellar winds). The VHE  $\gamma$ -ray flux from a colliding wind scenario could be modulated by wind instabilities and outbursts or with the orbital period of the system, if it involves geometric effects like varying distance between the companions or line of sight issues (e.g. absorption).

**Collective Wind Phenomena** The collective winds of all member stars of a young stellar cluster could give rise to shock fronts e.g. when the winds collide with each other or when the collective wind-driven *super bubble* interacts with the surrounding medium. Klepach *et al.* (2000) discuss the CR production from colliding multiple spherical shocks, which could give rise to VHE  $\gamma$ -rays from  $\pi^0$  decays. A collective wind scenario proposed by Domingo-Santamaría & Torres (2006) predicts that the extension of a  $\gamma$ -ray source corresponds to the volume filled by the hot, shocked stellar winds. Variability is generally not expected since flux modulation of the winds of individual stars or binaries is believed to average out in a collective wind. Interestingly, a putative VHE  $\gamma$ -ray source may not possess a non-thermal counterpart at MeV/GeV energies in such a scenario, since convection will prevent low-energy particles from entering the wind. In both colliding wind zone and collective wind models, one would expect sub-TeV spectra that resemble those of Supernova remnants.

Other possible production mechanisms are connected to shocks resulting from magnetic fields, turbulences and inhomogenities in the plasma from wind blown bubbles and are further discussed in Sect. 5.5.

### 5.3 The Westerlund 2 Region

The stellar cluster Westerlund 2 (Westerlund 1960), is located towards the outer edge of the Carina spiral arm of our Milky Way. It contains an extraordinary ensemble of hot and massive stars, presumably at least a dozen early-type O-stars, and two remarkable WR stars. The stars from Westerlund 2 ionize the luminous giant HII region RCW 49 (also NGC 3247). Two Wolf-Rayet (WR) stars have been found within the vicinity of Westerlund 2: (1) WR 20b at  $\alpha_{2000} = 10^{\text{h}}24^{\text{m}}18.^{\text{s}}4$ ,  $\delta_{2000} = -57^{\circ}48'30''$ , and (2) WR 20a at  $\alpha_{2000} = 10^{\text{h}}23^{\text{m}}58.^{\text{s}}0$ ,  $\delta_{2000} = -57^{\circ}45'49''$  (van der Hucht 2001), both first reported as WR stars by Shara *et al.* (1991), the latter is believed to be a member of the stellar cluster Westerlund 2.

Only recently WR20a was established to be a binary system: optical spectroscopy of WR20a revealed two superimposed spectra, with their emission and absorption lines shifting relatively to each other in time. By measuring the relative radial velocity of the two superimposed spectra both Rauw *et al.* (2004) and Bonanos *et al.* (2004) presented solutions for a circular orbit with a period of 3.675, and 3.686 days, respectively. Based on the the orbital period, the minimum masses have been found to be  $(83 \pm 5) M_{\odot}$  and  $(82 \pm 5) M_{\odot}$  for the primary and secondary components, respectively (Rauw *et al.* 2005). This classifies the WR binary WR 20a as the most massive of all confidently

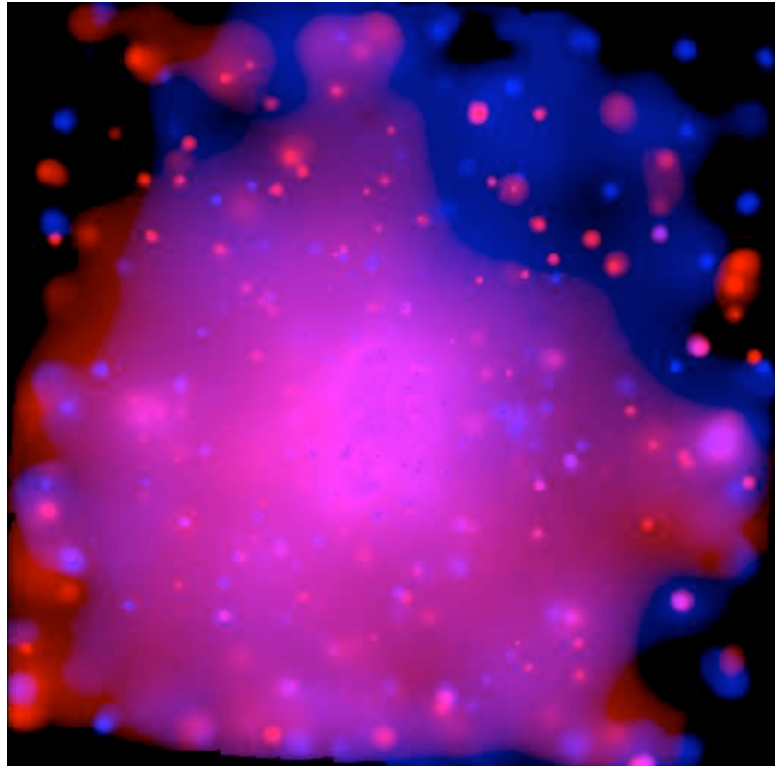


FIGURE 5.1: X-ray observations of the Westerlund 2 region with the CHANDRA satellite (exposure: 36 ks). The image size is  $17' \times 17'$ . The image is smoothed and the colors encode different x-ray bands: red = (0.5–2 keV), blue = (2–8 keV). (Townesley *et al.* 2005)

measured binary systems in our Galaxy. An orbital inclination of  $\sim 75^\circ$  was inferred from photospheric eclipses (Bonanos *et al.* 2004).

It is expected that the supersonic stellar winds of the two WR stars from the WR20a binary system collide, and a wind-wind interaction zone forms at the stagnation point with a reverse and forward shock (Rauw *et al.* 2005). In a detached binary system like WR 20a, the colliding wind zone lies between the two stars, and is heavily skewed by Coriolis forces. The wind velocity at the stagnation point is likely lower than in other positions due to the *radiative inhibition mechanism* (Stevens & Pollock 1994) caused by the companion's stellar photon field. In a close binary system the winds can only be radiatively accelerated to a fraction of their expected terminal velocity  $v_\infty \sim 2800$  km/s, and a comparatively low pre-shock wind velocity of  $\sim 500$  km/s follows (Rauw *et al.* 2005).

Radio synchrotron emission has not been detected from the WR 20a system, presumably because of free-free-absorption in the optically thick stellar winds along the line of sight. However, WR 20a has been detected in X-rays (Mereghetti & Belloni 1996). With a flux of the order of  $10^{-12}$  erg cm $^{-2}$  s $^{-1}$ , the soft X-ray emission is consistent with the predicted intensity for the thermal radiation from the shock-heated material in the stellar wind (Pittard & Stevens 2002). However, non-thermal and thermal components of the X-ray emission are currently indistinguishable.

The ionized HII region RCW 49 is a luminous, massive star formation region, and has been extensively studied at various wavelengths. After the initial report based

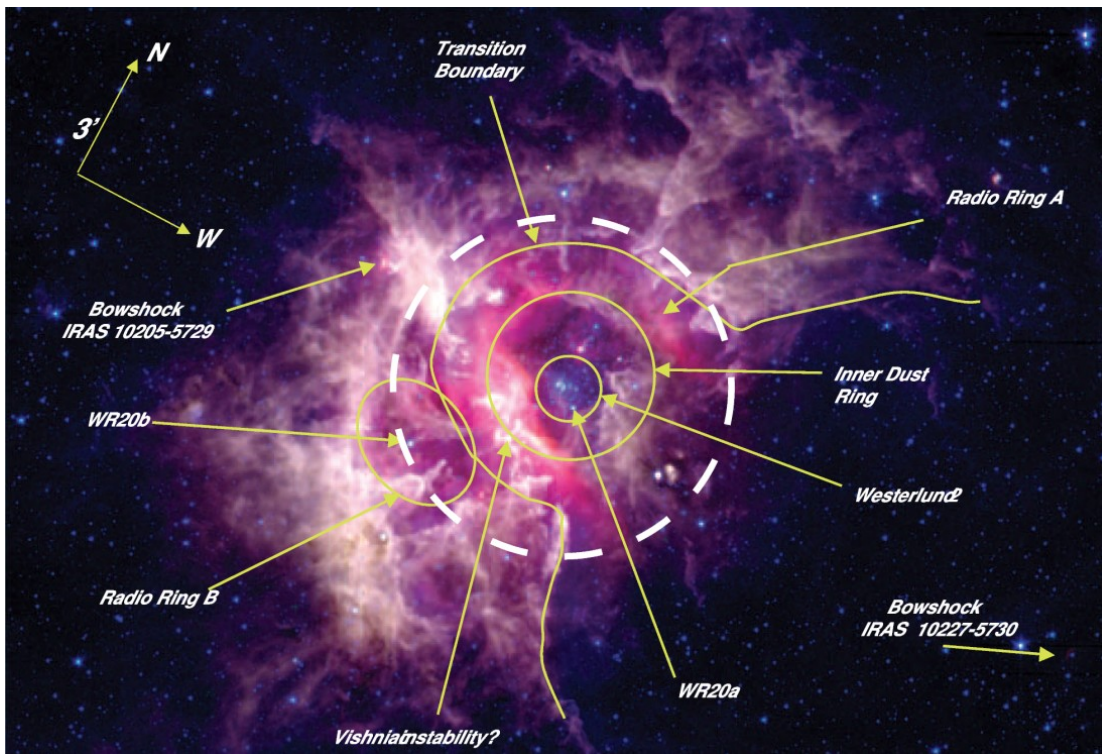


FIGURE 5.2: Westerlund 2 star cluster and surrounding in the infrared; SPITZER telescope composite image using the wavelength bands: 3.6, 5.8 and 8  $\mu\text{m}$ ; Dimensions:  $\sim 0.3^\circ \times 0.5^\circ$ . The white dashed circle gives the approximate extension of the Westerlund 2 cluster and will be used in further skymaps to indicate the location and extension of Westerlund 2. (adapted from Churchwell *et al.* (2004))

on photographic images by Rodgers *et al.* (1960), the region was observed at X-ray energies with *Einstein* (Hertz & Grindlay 1984; Goldwurm *et al.* 1987), ROSAT (Belloni & Mereghetti 1994), and recently *Chandra*, which discovered  $\sim 500$  point sources in the vicinity of RCW 49 (Tsujimoto *et al.* 2004), with  $\sim 100$  of them spatially coincident with the central open stellar cluster Westerlund 2 and extended diffuse emission (Fig. 5.1) (Townsend *et al.* 2005).

Mid-infrared measurements with *Spitzer* (Fig. 5.2) revealed still ongoing massive star formation in RCW 49 (Whitney *et al.* 2004). The regions surrounding Westerlund 2 appear evacuated by stellar winds and radiation. The surrounding dust is distributed in fine filaments, knots, pillars, bubbles, and bow shocks throughout the rest of the HII complex (Churchwell *et al.* 2004; Conti & Crowther 2004). Radio continuum observations by ATCA at 1.38 and 2.38 GHz indicate two wind-blown shells in the core of RCW 49 (Whiteoak & Uchida 1997): one surrounding the central region of Westerlund 2, the other the prominent WR star WR 20b. In high-energy  $\gamma$ -rays, three unidentified EGRET sources have been found in the wider vicinity of RCW 49, 3EG J1013-5915, 3EG J1014-5705, and 3EG J1027-5817 (Hartman *et al.* 1999). These EGRET sources are characterized by both source confusion, and indication of extended emission, therefore viable counterparts are not established readily.

The distance to RCW 49 is still uncertain and values range between  $\sim 2.2$  kpc (Brand

& Blitz 1993) up to 7.9 kpc (Moffat *et al.* 1991), whereas intermediate values of 4.2 kpc from 21 cm absorption line profile measurements (McClure-Griffiths *et al.* 2001), 5.75 kpc from the distance estimate towards the prominent WR star WR 20a (van der Hucht 2001), and 6.4 kpc from photometric measurements (Carraro & Munari 2004) represents a more recent refinements. Finally, Rauw *et al.* (2007) presented a compelling re-determination of the distance to Westerlund 2 by spectro-photometric measurements of 12 cluster member O-type stars of  $(8.3 \pm 1.6)$  kpc. This value is in very good agreement with the  $(7.9 \pm 0.6)$  kpc as determined by Rauw *et al.* (2005), derived from a model of the absolute luminosity based on the light curve of the eclipsing binary WR 20a. In summary, we adopt the distance value of the weighted mean of  $(8.0 \pm 1.4)$  kpc (Rauw *et al.* 2007) throughout this chapter, thereby associating WR 20a as a cluster member of Westerlund 2.

## 5.4 H.E.S.S. Observations of the Westerlund 2 Region

The dataset described here consists of 14 h (12.9 h live time) of data taken between March and July 2006, either on the nominal source location of WR 20a or overlapping data from the ongoing Galactic plane survey. Quality selections were imposed on the data, excluding those taken during bad weather or with hardware irregularities. The data have been obtained in wobble-mode observations, where the telescopes are pointed offset from the nominal source location to allow a simultaneous background estimation. The wobble offsets for these observations range from  $0.5^\circ$  to  $2^\circ$ , with the majority of data taken with wobble offset less than  $0.8^\circ$ . The zenith angles range between  $36^\circ$  and  $53^\circ$ , resulting in an energy threshold of 380 GeV for the analysis.

The data have been analyzed using the H.E.S.S. standard Hillas analysis with standard cuts (image amplitude  $> 80$  p.e.). Optical efficiency corrections have been applied as described in Aharonian *et al.* (2006h). A point source analysis on the nominal position of WR 20a resulted in a clear signal with a significance of 6.8 standard deviations. Further investigations of the skymap of this region revealed an extended excess with a peak significance exceeding 9 standard deviations (Fig. 5.3). The position of the center of the excess was derived by fitting the two-dimensional point spread function (PSF) of the instrument folded with a Gaussian to the uncorrelated excess map:  $\alpha_{2000} = 10^{\text{h}}23^{\text{m}}18^{\text{s}} \pm 12^{\text{s}}$ ,  $\delta_{2000} = -57^\circ45'50'' \pm 1'30''$ , therefore the source is labeled HESS J1023-577. The systematic error (pointing uncertainty) in the source location is  $20''$  in both coordinates.

The number of excess events versus the squared angular distance to this position in comparison to the expectation for a point source (dashed line) is shown in Fig. 5.4. The excess is clearly extended beyond the nominal extension of the PSF. A fit of a Gaussian folded with the PSF of the H.E.S.S. instrument gives an extension of  $\sigma = 0.18^\circ \pm 0.02^\circ$  (assuming radial symmetry).

The differential energy spectrum for photons derived with the method described in Appendix A inside the corresponding 85% containment radius of  $0.39^\circ$  is shown in Fig. 5.5. It can be described by a power law ( $dN/dE = \Phi_0 \cdot (E/1 \text{ TeV})^{-\Gamma}$ ) with a photon index of  $\Gamma = 2.53 \pm 0.16_{\text{stat}} \pm 0.1_{\text{syst}}$  and a normalization at 1 TeV of  $\Phi_0 = (4.50 \pm 0.56_{\text{stat}} \pm 0.90_{\text{syst}}) \times 10^{-12} \text{ cm}^{-2} \text{ s}^{-1} \text{ TeV}^{-1}$ . The integral flux for the excess above the energy threshold of 380 GeV derived from the spectrum is  $(1.3 \pm 0.3) \times 10^{-11} \text{ cm}^{-2} \text{ s}^{-1}$ . No significant flux variability could be detected in the data set (Fig. 5.6). The fit of a

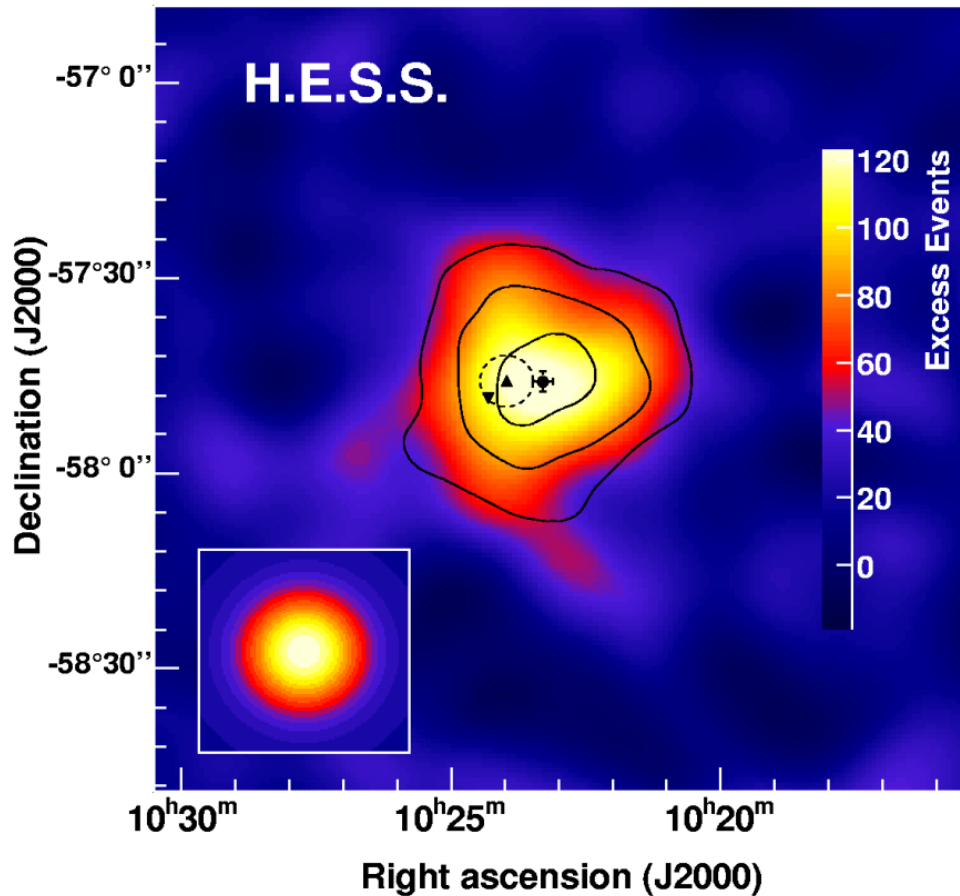


FIGURE 5.3: Correlated excess sky map with an oversampling radius of  $0.12^\circ$  of the Westerlund 2/RCW 49 region. The background in each bin is estimated using a ring around the test position. The map has been smoothed with a two-dimensional Gaussian of radius  $0.04^\circ$  to reduce the effect of statistical fluctuations. Overlaid contours correspond to statistical significances of  $5$ ,  $7$ , and  $9\sigma$ , respectively, determined using the nominal oversampling radius for extended sources of  $0.2^\circ$ . The inlay in the lower left corner shows the excess distribution for a point-source derived from Monte Carlo data with the same zenith-angle and pointing offset distribution as the data. The cross denotes the best fit position of the gamma-ray data with  $1\sigma$  statistical uncertainties. The WR binary WR 20a is indicated by an upright filled triangle in the Westerlund 2 stellar cluster (dashed circle, corresponding to the white dashed circle in Fig. 5.2), the reversed filled triangle denotes the location of WR 20b.

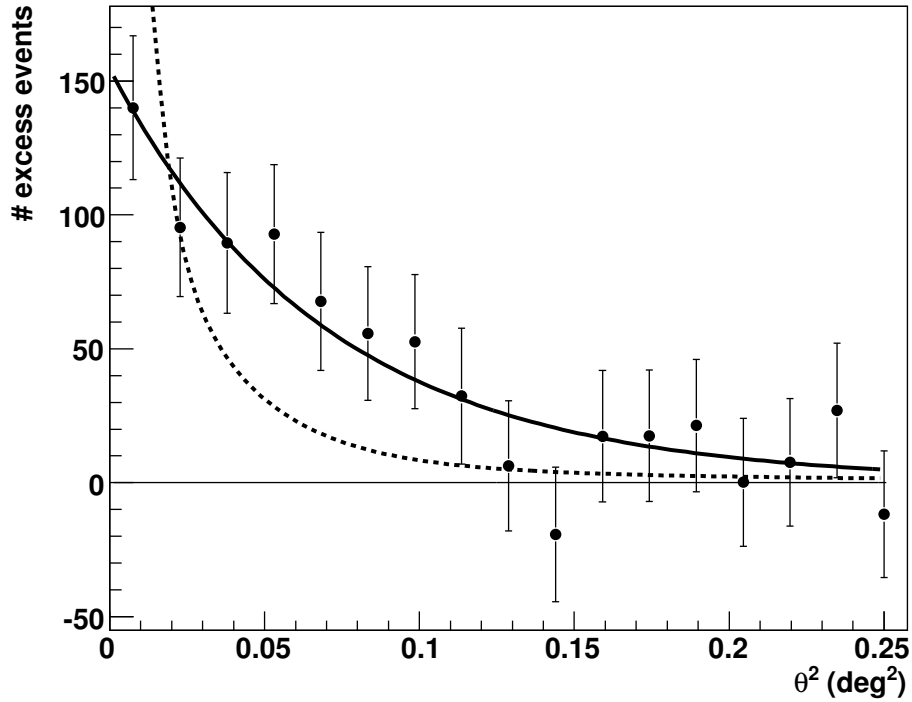


FIGURE 5.4: Number of excess events versus the squared angular distance ( $\theta^2$ ) with respect to the best fit position of the excess. The dashed line shows the expectation for a point source derived from Monte Carlo data. The solid line is a fit of the PSF folded with a Gaussian ( $\sigma = 0.18^\circ \pm 0.02^\circ$ ) (assuming radial symmetry).

constant function to the lightcurve binned in data segments of 28 minutes has a chance probability of 0.11. The results were checked with independent analyses and were found to be in good agreement.

## 5.5 Interpretation of the extended VHE $\gamma$ -ray Signal from Westerlund 2

The detection of VHE photons from the region RCW 49/Westerlund 2, characterized by a moderately hard power-law spectrum with an index  $\Gamma \sim 2.5$  is indicative of the existence of extreme high-energy particle acceleration processes in this young ( $\sim 2$ -3 Myrs; Piatti *et al.* (1998)) star forming region. Assuming a distance of 8 kpc, the luminosity above 380 GeV for the VHE  $\gamma$ -ray source is  $\sim 1.5 \times 10^{35}$  erg/s.

**WR20a** One possible source of the VHE  $\gamma$ -rays are colliding winds in stellar binary systems, with WR20a being an obvious candidate. Detectable VHE  $\gamma$ -radiation from WR 20a is so far only predicted in the pair cascade model, although detailed modeling of the WR 20a system in the other scenarios is still pending. Due to the dense radiation field at the wind collision zone in the close binary, VHE  $\gamma$ -rays are efficiently

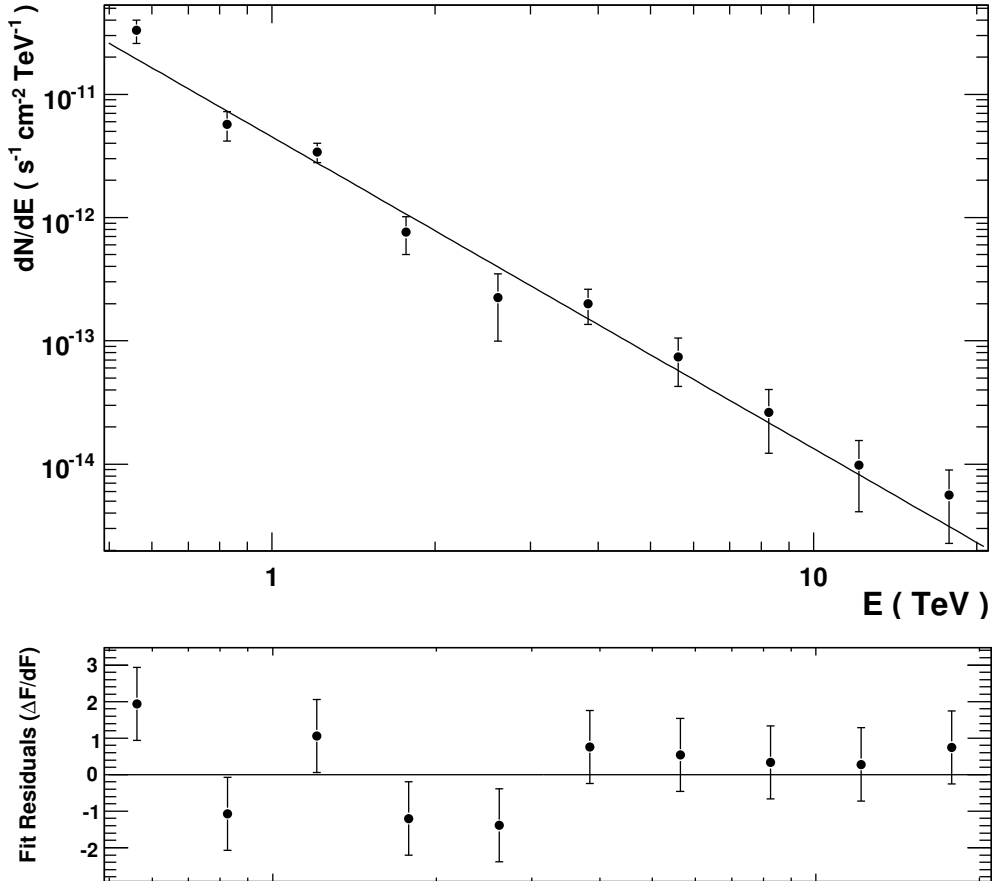


FIGURE 5.5: Differential energy spectrum and fit residuals to a single power-law fit of HESS J1023–575 from photons inside the 85% containment radius ( $0.39^\circ$ ) around the best fit position. The background is estimated with background regions of the same size and distance from the camera center as the signal region. The spectrum can be described by a power law with a photon index of  $\Gamma = 2.53 \pm 0.16_{\text{stat}} \pm 0.1_{\text{syst}}$  and a normalization at 1 TeV  $\Phi_0 = (4.50 \pm 0.56_{\text{stat}} \pm 0.90_{\text{syst}}) \times 10^{-12} \text{ TeV}^{-1} \text{ cm}^{-2} \text{ s}^{-1}$ . The integral flux for the excess as derived from the spectrum is  $F(E > 380 \text{ GeV}) = (1.3 \pm 0.3) \times 10^{-11} \text{ cm}^{-2} \text{ s}^{-1}$ .

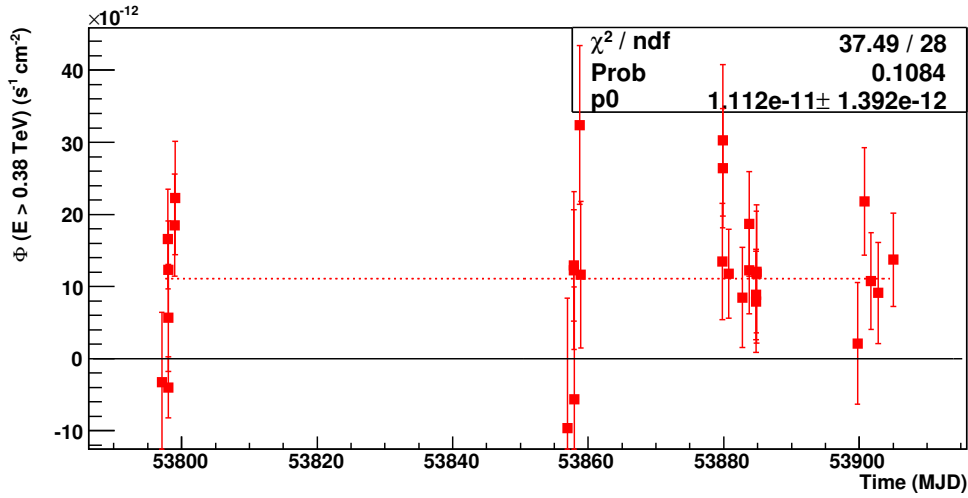


FIGURE 5.6: Integral flux above 380 GeV of HESS J1023-575 for data segments of length 28 min versus time. The red dotted line is the fit of a constant function to the data yielding a chance probability of 0.11 for the fit. The fit parameters are given in the box.

absorbed by photon-photon reactions, and pair cascades are unavoidable. If the nuclei accelerated in the colliding wind shock reach sufficiently high energies (despite the expected weak shock in the extremely dense radiative environment), the projectile nucleons themselves are produced by photodisintegration of heavy nuclei in the radiation fields of the massive WR-stars (Bednarek 2005). For a high magnetic field of the order  $10^3$  G, particles could be energized up to  $\sim 10^{15}$  eV (adopting typical WR-wind parameters) in the magnetic field reconnection scenario, and up to  $10^{12}$  eV if first-order Fermi acceleration takes place there. The maximum power extractable from WR 20a must be a fraction of the kinetic wind energy provided by the system, estimated to be  $\sim 10^{37}$  erg/s. For VHE  $\gamma$ -rays, photon-photon absorption will diminish the observable flux from a close binary system such as WR 20a (Bednarek 2005; Dubus 2006). Taking the above derived luminosity of  $\sim 1.5 \times 10^{35}$  erg/s, this would correspond to 0.5% of the total kinetic energy available from the colliding winds of WR 20a, and  $\sim 1.6\%$  of the kinetic energy of WR 20b.

With a projected angular size of submilliarcsecond scale, the WR 20a binary system, including its colliding wind zone, would appear as a point source for observations with the H.E.S.S. telescope array. Unless there are extreme differences in the spatial extent of the particle distributions producing radio, X-ray, and VHE  $\gamma$ -ray emission, scenarios based on the colliding stellar winds in the WR 20a binary system face the severe problem of accounting for a source extension of  $0.18^\circ$  in the VHE waveband. If VHE  $\gamma$ -rays were indeed produced near the massive stars in the binary, a regular modulation of the  $\gamma$ -ray flux due to absorption would be expected Dubus (2006). Future observations of HESS J1023-575 will allow us to probe for such a pattern, which could discard or unambiguously label the origin of the VHE emission.

**Westerlund 2** The spatial extension found for HESS J1023-575 is much more extended than Westerlund 2, which contradicts emission scenarios where the bulk of the  $\gamma$ -rays

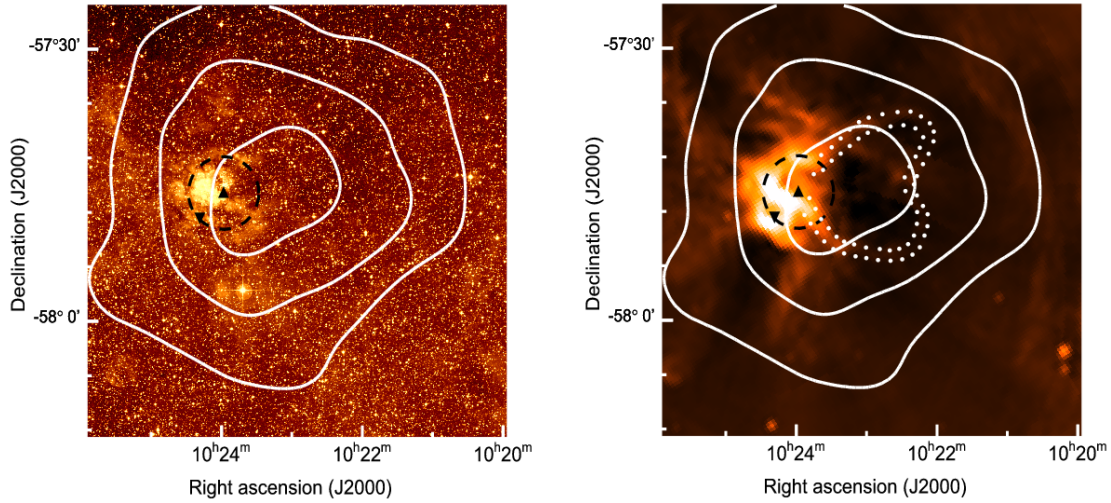


FIGURE 5.7: *Left Panel:* HESS J1023–575 significance contours (corresponding 5, 7 and 9  $\sigma$ ), overlaid on a B-band image from the Second Palomar Observatory Sky Survey (POSS-2). The WR binary WR 20a is indicated by an upright filled triangle in the Westerlund 2 stellar cluster (dashed circle), the reversed filled triangle denotes the location of WR 20b. *Right Panel:* HESS J1023–575 significance contours, overlaid on a 843 MHz image from the Molonglo Observatory Synthesis Telescope (MOST). Black symbols and dashed circle as in the left panel. The wind-blown bubble around WR 20a, and the blister to the west of it are seen as depressions in the radio continuum map. The blister is indicated by white dots as in Whiteoak & Uchida (1997), and appears to be compatible in direction and location with the center of gravity of HESS J1023–575.

are produced close to the massive stars. Assuming again 8.0 kpc as the distance of the source, the source extension is equivalent to a diameter of 28 pc for the emission region, which is consistent in size with theoretical predictions of bubbles blown from massive stars into the ISM (Castor *et al.* 1975).

The emission could arise from collective effects of stellar winds in the Westerlund 2 cluster. Diffusive shock acceleration in cases where energetic particles experience multiple shocks (Klepach *et al.* 2000) can be considered for Westerlund 2. The stellar winds may provide a sufficiently dense target for high-energy particles (accelerated to hundreds of TeV in internal shocks in the winds themselves or driven by supernova explosions), allowing the production of  $\pi^0$ -decay  $\gamma$ -rays via inelastic pp-interactions. According to Rauw *et al.* (2007) Westerlund 2 may host about 4500  $M_{\odot}$  in the form of stars with  $M > M_{\odot}$ . The mechanical energy injected through the stellar winds determines mainly the total energy available for collective wind effects, estimated to be about  $5.4 \times 10^{37}$  erg/s at most (Aharonian *et al.* 2007). Taking the VHE  $\gamma$ -ray luminosity derived above, at least 0.3% of the total mechanical energy would be needed to power the source in this scenario.

**Magneto-hydrodynamic (MHD) particle acceleration** Magneto-hydrodynamic (MHD) particle acceleration (e.g. by multiple shocks or turbulence produced by supersonic flows) in a magnetized plasma when particles penetrate into a dense medium may also be considered. In such a case, the massive stellar winds of Westerlund 2

could accomplish three tasks: they could ensure sufficient particle injection into the turbulent plasma, feed the magnetic turbulence with energy via wind-wind interactions in the massive star association, or provide copious photons and dense material to serve as target for TeV-photon production in particle-photon and photon-photon interactions. Supershells, molecular clouds, and inhomogeneities embedded in the dense hot medium may serve as the targets for  $\gamma$ -ray production in Cosmic Ray interactions. Such environments have been already studied in the nonlinear theory of particle acceleration by large-scale MHD turbulence (Bykov & Toptygin 1987). Shocks and MHD turbulent motion inside a stellar bubble or superbubble can efficiently transfer energy to cosmic rays if the particle acceleration time inside the hot bubble is much shorter than the bubble's expansion time.

X-ray observations of RCW 49 revealed, apart from point-like emission from individual stars, a diffuse component centered on the ionizing cluster, widely extending outside the core, with a soft component and a hard tail (Belloni & Mereghetti 1994; Townsley *et al.* 2005). This indicates the existence of a wind-blown shell from the stars at the cluster core, filled with a hot ( $\sim 0.1 - 3$  keV) tenuous plasma shocked by turbulence. Two wind-blown bubbles are revealed from continuum radio observations: one around WR 20b with a diameter of  $\sim 4.1'$  and an expansion velocity of 67 km/s (Shara *et al.* 1991), the other around the Westerlund 2 cluster center with a diameter of  $\sim 7.3'$  (Whiteoak & Uchida 1997). A ridge of enhanced GHz radio emission lies between these two shells, and it has been suggested that this may represent a site of collision between these two shells (Whiteoak & Uchida 1997).

**Radio Blister** Most interestingly, the extent of a radio blister (Whiteoak & Uchida 1997) on the western side of the Westerlund 2 bubble appears to be compatible in direction and location with the center of gravity of HESS J1023–575. Such a blister is indicative for rapid expansion into a low-density medium outside the wind-blown bubble. Fig. 5.7 shows overlays of the detection significance contours of HESS J1023–575 ( $E > 380$  GeV) on the B-band image of the region as obtained from the Second Palomar Observatory Sky Survey (POSS-2), and on the 843 MHz radio continuum image from the Molonglo Observatory Synthesis Telescope (MOST), respectively. Whereas the open cluster Westerlund 2 does not perfectly coincide with the peak of the emission seen at very high energy  $\gamma$ -rays (Fig. 5.7 left), the direction of the outbreak and spatial location of the blister is a better match (Fig. 5.7 right) and the extension fits well with the measured extension of the VHE  $\gamma$ -ray source.

Shock acceleration at the boundaries of the blister may enable particles to diffusively re-enter into the dense medium, thereby interacting in hadronic collisions and producing  $\gamma$ -rays. Consequently, a scenario as outlined in Völk (1983) for a supernova-driven expansion of particles into a low density medium may be applicable to the expanding stellar winds into the ambient medium. If one accepts such a scenario here, it might give the first observational support of  $\gamma$ -ray emission due to diffusive shock acceleration from supersonic winds in a wind-blown bubble around WR 20a, or the ensemble of hot and massive OB stars from a superbubble in Westerlund 2, breaking out beyond the edge of a molecular cloud (Tenorio-Tagle 1979; Völk & Forman 1982; Cesarsky & Montmerle 1983; Bykov 2001). Accordingly, one has to consider that such acceleration sites will also contribute to the observed flux of cosmic rays in our Galaxy (Casse & Paul 1980).

### 5.5.1 Summary & Outlook

Though a wealth of possible scenarios for VHE  $\gamma$ -ray production scenarios exists, none of them is compelling enough on its own to explain the VHE  $\gamma$ -ray source HESS J1023-577 (with one possible exception: particle acceleration connected to the radio blister). Further observation in VHE  $\gamma$ -rays with longer exposure may reveal further substructures and morphology, which could help disentangle the underlying physics. Another candidate for VHE  $\gamma$ -ray emission from stellar clusters is the unidentified TeV source TeV J2032+4130 (Aharonian *et al.* 2005f), where the Cygnus OB2 stellar association has been discussed as possible counterpart.

Other open star clusters hosting WR-stars are known to supersede the total injected mechanical energy from winds of massive stars as available in Westerlund 2: Westerlund 1, which is older than Westerlund 2 and lies at a recently revised distance of 5 kpc (Crowther *et al.* 2006), and NGC 3603, a very prominent galactic starburst region at a distance of 7 kpc. Both offer approximately  $10^{39}$  erg/s (Muno *et al.* 2006; Stevens & Hartwell 2003). Search for TeV-emission from open stellar clusters has been previously carried out for a list of northern clusters by HEGRA (Aharonian *et al.* 2006g), resulting in upper limits in the order of  $10^{-11}$  to  $10^{-13}$   $\text{cm}^{-2} \text{s}^{-1}$  at varying energy thresholds between 0.8 and 3 TeV. The southern hemisphere stellar cluster Westerlund 2 was not targeted by HEGRA. The detection of very-high-energy  $\gamma$ -rays associated with Westerlund 2 by H.E.S.S. clearly motivates systematic searches for TeV-emission from massive open stellar clusters.



## Chapter 6

# Summary and Outlook

In this work data obtained with the H.E.S.S. Cherenkov telescopes are analyzed, leading to the discovery of two new sources of very-high-energy ( $E > 100$  GeV; VHE)  $\gamma$ -rays. Furthermore, the VHE  $\gamma$ -rays from distant sources are used to probe the diffuse extragalactic photon fields in the ultraviolet to far-infrared wavelength regime, leading to strong constraints on the density of these photon fields.

### New Constraints on the Extragalactic Background Light (EBL)

The VHE  $\gamma$ -ray spectra from all known TeV blazars<sup>1</sup> are used to derive limits on the meta-galactic radiation field at ultraviolet to far-infrared wavelength (extragalactic background light; EBL) (Chapter 3). It is the most complete study of this type to date. Since the density of the EBL is only poorly constrained by direct measurements, a large set of different EBL shapes derived from a grid in EBL wavelength vs EBL density is tested. Limits derived from the individual spectra of Mkn 421, H1426+428 and 1ES 1101-232 are presented and discussed. The combined limit derived from all spectra ranges from optical ( $\sim 0.5\mu\text{m}$ ) to far-infrared wavelengths ( $\sim 90\mu\text{m}$ ) of the EBL and is only a factor of 2 to 3 higher than the lower limits derived from source counts. An excess in the near-infrared, claimed by direct detection experiments, which has been interpreted as a signature from the first stars (Population III Stars), is excluded by the limit. The limits can be interpreted in two ways: (1) The universe is much more transparent to VHE  $\gamma$ -rays than previously thought. (2) The assumptions about the VHE  $\gamma$ -ray emission processes in TeV blazars used to derive the limits are incorrect. This would require fundamental changes in current standard paradigm for TeV blazar emission processes.

The discovery of more extragalactic VHE  $\gamma$ -ray sources at different redshifts will help to disentangle the intrinsic emission from attenuation effects from the EBL and improve the constraints on the EBL.

### Discovery of two new sources of VHE $\gamma$ -rays

The BL Lac 1ES 0347-121, an active galactic nuclei (AGN) with the particle jet pointed towards the observer, has been discovered in a H.E.S.S. data-set from 2006 with high

---

<sup>1</sup>With a published spectrum.

significance of more than 10 standard deviations (Chapter 4). With a redshift of  $z = 0.1880$ , it is the farthest firmly established extragalactic source of VHE  $\gamma$ -rays today. The VHE energy spectrum has been measured from 250 GeV to  $\sim 3$  TeV and is well fitted by a power law function  $dN/dE \sim E^{-\Gamma}$  with  $\Gamma = 3.08 \pm 0.23_{\text{stat}} \pm 0.1_{\text{sys}}$ . The integral flux above a threshold of 250 GeV corresponds to  $\sim 2\%$  of the flux of the Crab Nebula above the same threshold. No significant VHE variability has been detected in the data-set. Contemporary optical/UV and x-ray data from the SWIFT satellite is used to construct the spectral energy distribution (SED) of the source. The SED can be described in terms of simple synchrotron-self-Compton model. An inverse Compton peak at energies beyond 3 TeV, which might be implied by two of the three EBL models used to calculate the intrinsic spectrum, is challenging the SSC model. The large distance and the relative hard VHE spectrum makes 1ES 0347-121 a good candidate for studies of the EBL. Limits on the EBL derived from the VHE spectrum of 1ES 0347-121 are found to be slightly less constraining than limits derived from the VHE spectrum of the BL Lac 1ES 1101-232, which is located at a similar distance ( $z = 0.186$ ) and currently provides the strongest constraints on the EBL in near-infrared wavelengths. Further monitoring of the source, which might result in the detection of a high flux state (flare), are highly desirable. If a flare is detected, simultaneous multi-wavelength observations, especially in x-rays, will help to further constraint the emission models.

The extended VHE  $\gamma$ -ray source HESS J1023-577, detected with a significance of more than 10 standard deviations, is associated with the young and massive stellar cluster Westerlund 2 and its surrounding (Chapter 5). The production of the VHE  $\gamma$ -rays is believed to be connected to the strong winds from hot massive stars and the interactions of the winds with each other and the surrounding. These wind interactions could also give a significant contribution to the cosmic ray density. HESS J1023-577 is the first VHE  $\gamma$ -ray source firmly associated with such phenomena. The extension of the source, taken as the width  $\sigma$  of a Gaussian function folded with the point-spread-function, has been derived to  $\sigma = 0.18^\circ \pm 0.02^\circ$ . The VHE energy spectrum ranging from  $\sim 400$  GeV to  $\sim 20$  TeV is well fitted by a power-law function with photon index  $\Gamma = 2.53 \pm 0.16_{\text{stat}} \pm 0.1_{\text{syst}}$ . Due to wealth of possible production mechanisms and sites in the vicinity of Westerlund 2 further observation are needed, especially to allow for more detailed studies of the morphology of the VHE  $\gamma$ -rays excess.

The H.E.S.S. experiment has demonstrated the power of the new generation of imaging atmospheric Cherenkov telescopes (IACT) for the discovery and detailed study of sources of VHE  $\gamma$ -rays. Especially the capability to resolve sources and to study morphology in great detail is a milestone in ground based VHE  $\gamma$ -ray observation. The discovery of dozens of new sources in our galaxy, which all have to be studied in detail, will surely keep astronomers busy for the coming years. In the near future the H.E.S.S. Phase 2<sup>2</sup> and the MAGIC 2<sup>3</sup> will come online, which will provide higher sensitivity and extend the accessible energy range to even lower energies, hopefully allowing for an overlap in energy with the GLAST satellite. On the horizon, the Cherenkov Telescope Array (CTA), a large array consisting of up to 100 IACTS of different sizes, is already on the way.

<sup>2</sup>A giant telescope with mirror diameter  $\sim 25$  m at the center of the existing H.E.S.S. telescope array.

<sup>3</sup>Extending the MAGIC telescope with a second similar telescope for stereoscopic observations.

# Appendix A

## Energy Estimation and Spectral Analysis

### A.1 Energy Estimation

The standard energy estimation for IACTs utilizes lookup-tables created from Monte Carlo data. These tables are produced for a set of zenith angles and pointing offset positions and are binned in impact parameter  $i$  and SIZE  $s$ . In this work, the height of the shower maximum  $h_{\max}$  is used as an additional parameter for the lookup-tables:

$$\frac{i}{h_{\max}} = \tan d \approx d \Rightarrow h_{\max} \approx \frac{i}{d} \quad (\text{A.1})$$

with distance (DIST)  $d$ .

For a given bin in zenith angle  $z$ , pointing offset  $o$ , impact parameter  $i$  and height of the shower-maximum  $h_{\max}$  the relation between energy  $E$  and SIZE  $s$  is assumed to be a linear function. The slope of this function is calculated by fitting a line to the SIZE vs energy distribution of a certain bin. The slope is stored in the lookup-tables. The energy of a certain event is then given by:

$$E_{\text{reco}}(z, o, i, h_{\max}, s) = L(z, o, i, h_{\max}) \cdot s \quad (\text{A.2})$$

where  $E_{\text{reco}}(z, o, i, h, s)$  is the reconstructed energy and  $L(z, o, i, h)$  is the slope from the corresponding lookup table. More details on the method are given in Raue (2003).

The use of a linear function for the dependency between energy and SIZE is not completely correct and results in a characteristic offset in the relative energy resolution  $(E_{\text{reco}} - E_{\text{true}})/E_{\text{true}}$  versus energy (see Fig. A.1). One way to overcome this problem is to use different functions with more parameters to describe the relation between energy and SIZE. A different solution is using a correction function on the reconstructed energy to compensate the offset. The offset of the relative energy resolution can be well described by the following empirical function (black curve in Fig. A.1):

$$O(E) = c_1 \cdot \log E + c_2 \cdot E^{c_3} + c_4/E^{c_5} + c_6 \quad (\text{A.3})$$

$c_1$  to  $c_6$  are free parameters that are calculated by fitting the function  $O(E)$  to the offset vs energy distribution. The basic dependency of the offset is the SIZE, so a function depending on the energy shifts with zenith angle. Consequently separate correction

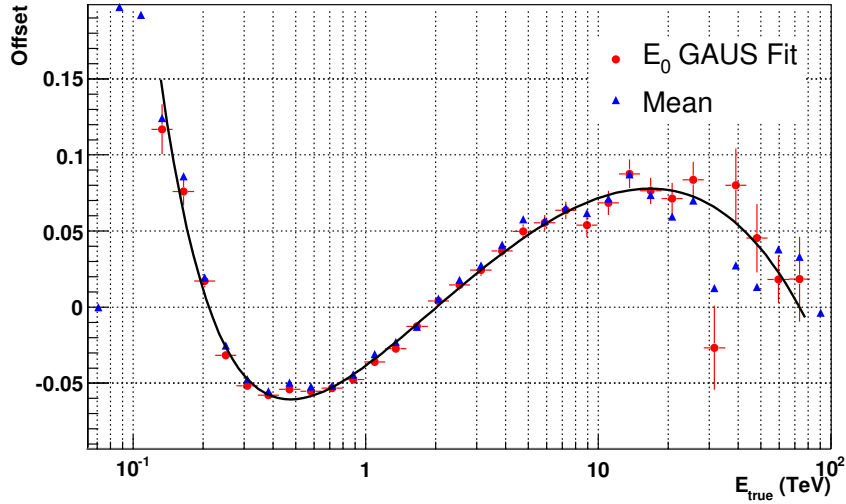


FIGURE A.1: Example for the offset of the relative energy resolution  $(E_{\text{reco}} - E_{\text{true}})/E_{\text{true}}$  for slices in energy (zenith angle =  $20^\circ$ ). The offset is shown for the mean of the distribution and the center of a gaussian fit. The energy dependency of the offset is well described by the fit function (black line) (see text for details).

functions are produced for different zenith angles (and set of cuts) and are linearly interpolated.

The resulting energy resolution and offset for zenith angle of  $20^\circ$  and  $45^\circ$  are shown in Fig. A.2 and A.3. The overall energy resolution is in the order of 12 to 14%. There is no significant offset, except for a small rise toward the energy threshold. For all steps in the production of the lookup-tables (creating the original lookup-table, fitting the offset, calculating the energy resolution) independent Monte Carlo data-sets have been used.

The use of the height of the shower maximum can in principle improve the energy resolution, since the amount of light reaching the camera depends on the height of the shower maximum (mainly determined by the height of the first interaction in the shower) (Hofmann *et al.* 2000). The gain in energy resolution with this method is found to be small ( $\sim 1\%$ ) compared to the energy resolution from the standard energy estimation.

The energy resolution is currently limited by the uncertainty in the reconstructed parameters used in the look-up tables. For the impact parameter the resolution is in the order of 10%, for the height of the shower maximum in the order of 10 to 15%. Other reconstruction techniques, which could improve the resolution, have already been envisaged (Hofmann *et al.* 1999) and used by the HEGRA experiment. Absolute limitations at low energies ( $< 100$  GeV) come from the shower inherent fluctuations.<sup>1</sup>

Systematic uncertainties in the reconstructed energy mainly arise from uncertainties in the Monte Carlo simulations. In the simulations, a single good weather atmosphere derived from measurements at the observation site is assumed, while the transmissivity of the real atmosphere is effected by e.g. clouds, haze, and smoke (Bernlöhner

<sup>1</sup>In addition, at energies  $< 100$  GeV the shower images of photon and proton induced showers are getting more and more similar, since the proton showers have often only one electro-magnetic sub-shower.

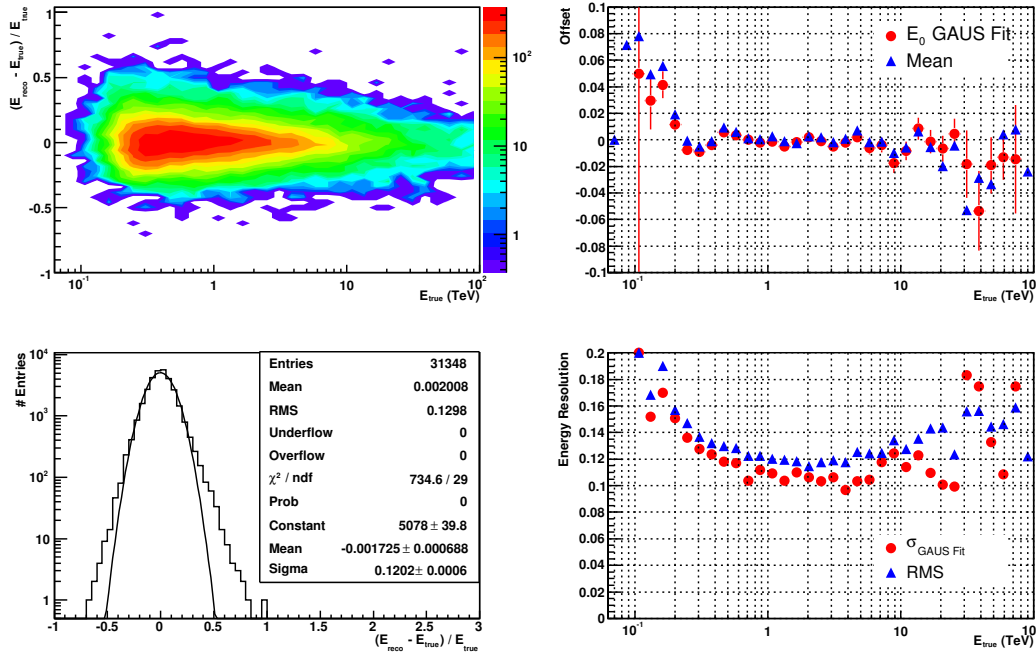


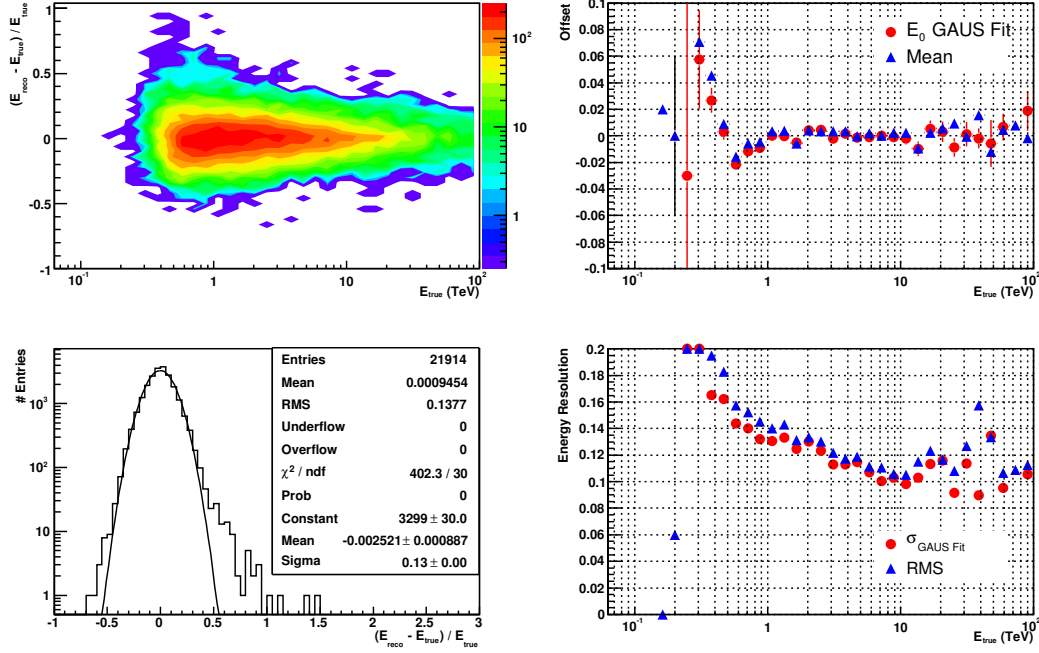
FIGURE A.2: Energy resolution  $((E_{\text{reco}} - E_{\text{true}})/E_{\text{true}})$  for Monte Carlo data with standard cuts at  $20^\circ$  zenith angle. *Top Left:* Relative energy resolution vs Monte Carlo energy  $E_{\text{true}}$ . The z-axis denotes the number of events and the colors scale is logarithmic to make the tails of the distribution visible. *Bottom Left:* Projection of the top left figure on the y-axis. The RMS of the energy resolution for all energies is  $\sim 13\%$ , the width of a Gaussian fit is  $\sim 12\%$  and the distribution is centered on zero. *Top Right:* Relative offset of the energy resolution for slices in energy. Shown are the mean of the distribution and the center of a gaussian fit. *Bottom Right:* Relative energy resolution for slices in energy. Shown is the RMS of the distribution and the width of a gaussian fit.

1999, 2000). To minimize the uncertainties from atmospheric effects, the atmospheric conditions are constantly monitored and only data taken under good conditions<sup>2</sup> is used. This leaves of course a certain spread in the quality of the data, which has to be taken into account as systematic uncertainty. The degradation of the reflectivity of the mirrors relative to the value used in the Monte Carlo is taken into account through the use of correction factors, which are derived from the images of single local muons (see Sect. 2.7 and Aharonian *et al.* (2006h)).

## A.2 Spectral Analysis

To derive fluxes and energy spectra from the measured VHE  $\gamma$ -ray rates, one needs to take into account the detector efficiency. This is done by calculating the effective detection area using Monte Carlo photon data. The effective area  $S_{\text{eff}}$  for a maximum impact parameter  $r_{\text{max}}$  is given by the number of Monte Carlo events remaining after

<sup>2</sup>Good atmospheric conditions are usually defined by the system trigger rate relative to a maximum system trigger rate (and some additional criteria like a maximum humidity)

FIGURE A.3: Same as Fig. A.2 but for  $45^\circ$  zenith angle.

analysis cuts  $N_{\text{post}}$  relative to the number of events simulated  $N_{\text{MC}}$  inside  $r_{\text{max}}$ :

$$S_{\text{eff}}(E, \theta, \beta, o, r_{\text{max}}, \text{Cuts}) = \pi \cdot r_{\text{max}}^2 \cdot \frac{N_{\text{post}}(E, \theta, \beta, o, r_{\text{max}}, \text{Cuts})}{N_{\text{MC}}(E, \theta, \beta, o, r_{\text{max}})} \quad (\text{A.4})$$

The effective area is calculated depending on the energy of the event  $E$ , the zenith angle  $\theta$ , the azimuth angle  $\beta$  (due to the different shower development depending on the orientation relative to the Earth's magnetic field; here only two settings are used: north and south), the camera offset  $o$ , and the analysis cuts. In Fig. A.4 the relative acceptance ( $S_{\text{eff}} / (\pi \cdot r_{\text{max}}^2)$ ) for the standard cuts (offset  $0.5^\circ$ , north) is shown depending on zenith angle and energy. The energy threshold rises with the zenith angle. For high zenith angles the relative acceptance at higher energies ( $E > 1$  TeV) increases, because shower more distant to the telescopes can be observed. More details on the method are presented in Raue (2003).

Systematic uncertainties in the reconstructed fluxes have similar dependencies on the Monte Carlo simulation as discussed in the previous section. The overall systematic uncertainty in the flux is estimated to be  $\sim 20\%$  (Aharonian *et al.* 2006h), mainly coming from the different atmospheric conditions and the uncertainties in the energy scale.

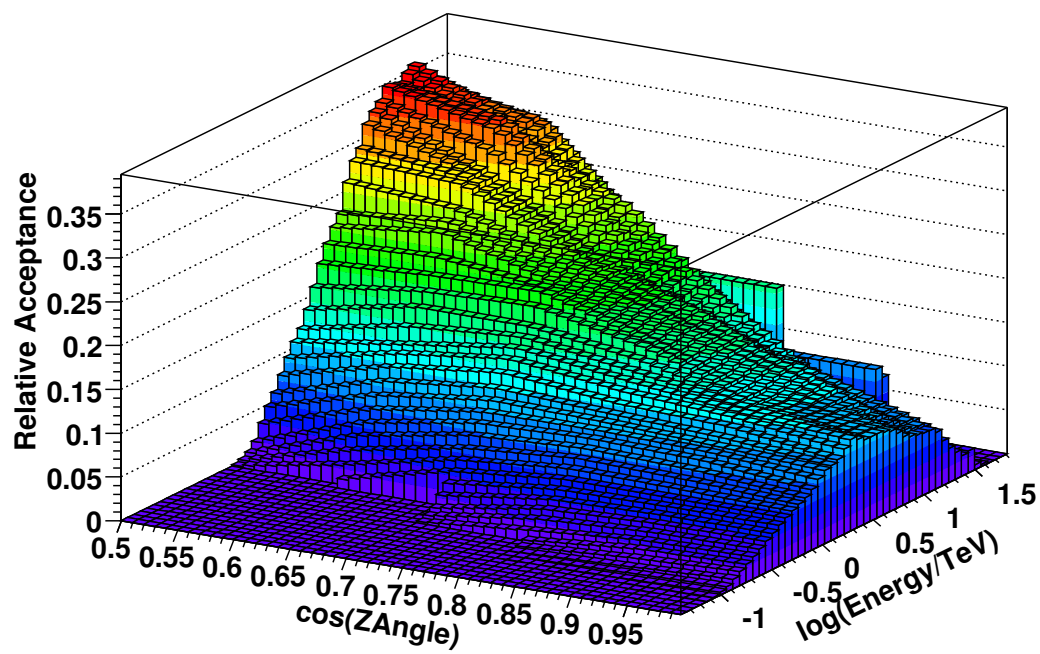


FIGURE A.4: Relative acceptance ( $S_{\text{eff}}/(\pi \cdot r_{\text{max}}^2)$ , see text for details) from Monte Carlo events versus zenith angle and energy for the standard cuts (offset  $0.5^\circ$ , north).



## Appendix B

# Likelihood Ratio Test

This section contains a brief discussion of the likelihood ratio test and has also been published in Mazin & Raue (2007).

The likelihood ratio test (Eadie *et al.* 1988) is a standard statistical tool to test between two hypotheses whether an improvement of a fit quality (quantified by corresponding  $\chi^2$  values) is expected from a normal distribution or it is significant. By fitting two functional forms to the intrinsic spectrum one obtains values of the likelihood functions  $L_A$  and  $L_B$ . If hypothesis A is true the likelihood ratio  $R = -\ln(L_A/L_B)$  is approximately  $\chi^2$  distributed with  $N$  degrees of freedom.  $N$  is the difference between numbers of degrees of freedom of hypothesis A and hypothesis B. One defines a probability

$$P = \int_0^{R_{meas}} p(\chi^2) d\chi^2 \quad (\text{B.1})$$

where  $p(\chi^2)$  is the  $\chi^2$  probability density function and  $R_{meas}$  is the measured value of  $R$ . Hypothesis A will be rejected (and hypothesis B will be accepted) if  $P$  is greater than the confidence level, which is set to 95%.



# Appendix C

## Collaboration Authors Lists

### C.1 H.E.S.S. Collaboration

Authors list of the H.E.S.S. collaboration as of May 2007:

Aharonian, F., Akhperjanian, A.G., Bazer-Bachi, A.R., Beilicke, M., Benbow, W., Berge, D., Bernlöhr, K., Boisson, C., Bolz, O., Borrel, V., Braun, I., Brion, E., Brown, A.M., Bühler, R., Büsching, I., Boutelier, T., Carrigan, S., Chadwick, P.M., Chounet, L.-M., Coignet, G., Cornils, R., Costamante, L., Degrange, B., Dickinson, H.J., Djannati-Ataï, A., O’C. Drury, L., Dubus, G., Egberts, K., Eifert, T., Emmanoulopoulos, D., Espigat, P., Farnier, C., Feinstein, F., Ferrero, E., Fiasson, A., Fontaine, G., Funk, S., Funk, S., Füßling, M., Gallant, Y.A., Giebels, B., Glicenstein, J.F., Glück, B., Goret, P., Hadjichristidis, C., Hauser, D., Hauser, M., Heinzlmann, G., Henri, G., Hermann, G., Hinton, J.A., Hoffmann, A., Hofmann, W., Holleran, M., Hoppe, S., Horns, D., Jacholkowska, A., de Jager, O.C., Kendziorra, E., Kerschhaggl, M., Khélifi, B., Komin, N., Kosack, K., Lamanna, G., Latham, I.J., Le Gallou, R., Lemièrre, A., Lemoine-Goumard, M., Lohse, T., Manchester, R.N., Martin, J.M., Martineau-Huynh, O., Marcowith, A., Masterson, C., Maurin, G., McComb, T.J.L., Moulin, E., de Naurois, M., Nedbal, D., Nolan, S.J., Noutsos, A., Olive, J.-P., Orford, K.J., Osborne, J.L., Panter, M., Pelletier, G., Petrucci, P.-O., Pita, S., Pühlhofer, G., Punch, M., Ranchon, S., Raubenheimer, B.C., Raue, M., Rayner, S.M., Reimer, O., Ripken, J., Rob, L., Rolland, L., Rosier-Lees, S., Rowell, G., Sahakian, V., Santangelo, A., Saugé, L., Schlenker, S., Schlickeiser, R., Schmidt, F., Schröder, R., Schwanke, U., Schwarzburg, S., Schwemmer, S., Shalchi, A., Sol, H., Spangler, D., Spanier, F., Steenkamp, R., Stegmann, C., Superina, G., Tam, P.H., Tavernet, J.-P., Terrier, R., Tluczykont, M., van Eldik, C., Vasileiadis, G., Venter, C., Vialle, J.P., Vincent, P., Völk, H.J., Wagner, S.J., and Ward, M.

### C.2 HEGRA Collaboration

Authors list of the HEGRA collaboration as of April 2001:

Aharonian, F., Akhperjanian, A., Barrio, J., Bernlöhr, K., Börst, H., Bojahr, H., Bolz, O., Contreras, J., Cortina, J., Denninghoff, S., Fonseca, V., Gonzalez, J., Götting, N., Heinzlmann, G., Hermann, G., Heusler, A., Hofmann, W., Horns, D., Ibarra, A., Iserlohe, C., Jung, I., Kankanyan, R., Kestel, M., Kettler, J., Kohnle, A., Konopelko, A.,

Kornmeyer, H., Kranich, D., Krawczynski, H., Lampeitl, H., Lopez, M., Lorenz, E., Lucarelli, F., Magnussen, N., Mang, O., Meyer, H., Mirzoyan, R., Moralejo, A., Ona, E., Padilla, L., Panter, M., Plaga, R., Plyasheshnikov, A., Prahl, J., Pühlhofer, G., Rautenberg, G., Röhring, A., Rhode, W., Rowell, G.P., Sahakian, V., Samorski, M., Schilling, M., Schröder, F., Siems, M., Stamm, W., Tluczykont, M., Völk, H.J., Wiedner, C.A., and Wittek, W.

### C.3 MAGIC Collaboration

Authors list of the MAGIC collaboration as of January 2007:

Albert, J., Aliu, E., Anderhub, H., Antoranz, P., Armada, A., Baixeras, C., Barrio, J.A., Bartko, H., Bastieri, D., Becker, J., Bednarek, W., Berger, K., Bigongiari, C., Biland, A., Bock, R.K., Bordas, P., Bosch-Ramon, V., Bretz, T., Britvitch, I., Camara, M., Carmona, E., Chilingarian, A., Ciprini, S., Coarasa, J.A., Commichau, S., Contreras, J.L., Cortina, J., Curtef, V., Danielyan, V., Dazzi, F., De Angelis, A., de los Reyes, R., De Lotto, B., Domingo-Santamaría, E., Dorner, D., Doro, M., Errando, M., Fagiolini, M., Ferenc, D., Fernández, E., Firpo, R., Flix, J., Fonseca, M.V., Font, L., Fuchs, M., Galante, N., Garczarczyk, M., Gaug, M., Giller, M., Goebel, F., Hakobyan, D., Hayashida, M., Hengstebeck, T., Höhne, D., Hose, J., Hsu, C.C., Jacon, P., Jogler, T., Kalekin, O., Kosyra, R., Kranich, D., Kritzer, R., Laille, A., Liebing, P., Lindfors, E., Lombardi, S., Longo, F., López, J., López, M., Lorenz, E., Majumdar, P., Maneva, G., Mannheim, K., Mansutti, O., Mariotti, M., Martínez, M., Mazin, D., Merck, C., Meucci, M., Meyer, M., Miranda, J.M., Mirzoyan, R., Mizobuchi, S., Moralejo, A., Nilsson, K., Ninkovic, J., Oña-Wilhelmi, E., Otte, N., Oya, I., Paneque, D., Paoletti, R., Paredes, J.M., Pasanen, M., Pascoli, D., Pauss, F., Pegna, R., Persic, M., Peruzzo, L., Piccioli, A., Poller, M., Puchades, N., Prandini, E., Raymers, A., Rhode, W., Ribó, M., Rico, J., Rissi, M., Robert, A., Rügamer, S., Saggion, A., Sánchez, A., Sartori, P., Scalzotto, V., Scapin, V., Schmitt, R., Schweizer, T., Shayduk, M., Shinozaki, K., Sidro, N., Sillanpää, A., Sobczynska, D., Stamerra, A., Stark, L.S., Takalo, L., Temnikov, P., Tesaro, D., Teshima, M., Tonello, N., Torres, D.F., Turini, N., Vankov, H., Vitale, V., Wagner, R.M., Wibig, T., Wittek, W., Zanin, R., and Zapatero, J.

# Bibliography

- AHARONIAN, F. *et al.* (H.E.S.S. COLLABORATION) 2004a. Calibration of cameras of the H.E.S.S. detector. *Astroparticle Physics*, **22**(Nov.), 109–125.
- AHARONIAN, F. *et al.* (HEGRA COLLABORATION) 2004b. Observations of 54 Active Galactic Nuclei with the HEGRA system of Cherenkov telescopes. *A&A*, **421**(July), 529–537.
- AHARONIAN, F. *et al.* (H.E.S.S. COLLABORATION) 2005a. A New Population of Very High Energy Gamma-Ray Sources in the Milky Way. *Science*, **307**(Mar.), 1938–1942.
- AHARONIAN, F. *et al.* (H.E.S.S. COLLABORATION) 2005b. Detection of TeV  $\gamma$ -ray emission from the shell-type supernova remnant RX J0852.0-4622 with HESS. *A&A*, **437**(July), L7–L10.
- AHARONIAN, F. *et al.* (H.E.S.S. COLLABORATION) 2005c. Discovery of VHE gamma rays from PKS 2005-489. *A&A*, **436**(June), L17–L20.
- AHARONIAN, F. *et al.* (H.E.S.S. COLLABORATION) 2005d. H.E.S.S. observations of PKS 2155-304. *A&A*, **430**(Feb.), 865–875.
- AHARONIAN, F. *et al.* (H.E.S.S. COLLABORATION) 2005e. Multi-wavelength observations of PKS 2155-304 with HESS. *A&A*, **442**(Nov.), 895–907.
- AHARONIAN, F. *et al.* (HEGRA COLLABORATION) 2005f. The unidentified TeV source (TeV J2032+4130) and surrounding field: Final HEGRA IACT-System results. *A&A*, **431**(Feb.), 197–202.
- AHARONIAN, F. *et al.* (H.E.S.S. COLLABORATION) 2006a. A detailed spectral and morphological study of the gamma-ray supernova remnant RX J1713.7-3946 with HESS. *A&A*, **449**(Apr.), 223–242.
- AHARONIAN, F. *et al.* (H.E.S.S. COLLABORATION) 2006b. A low level of extragalactic background light as revealed by  $\gamma$ -rays from blazars. *Nature*, **440**(Apr.), 1018–1021.
- AHARONIAN, F. *et al.* (H.E.S.S. COLLABORATION) 2006c. Discovery of very high energy  $\gamma$ -ray emission from the BL Lacertae object H 2356-309 with the HESS Cherenkov telescopes. *A&A*, **455**(Aug.), 461–466.
- AHARONIAN, F. *et al.* (H.E.S.S. COLLABORATION) 2006d. Evidence for VHE  $\gamma$ -ray emission from the distant BL Lac PG 1553+113. *A&A*, **448**(Mar.), L19–L23.
- AHARONIAN, F., *et al.* (H.E.S.S. COLLABORATION) 2006e. Fast Variability of Tera-Electron Volt gamma-rays from the Radio Galaxy M87. *Science*, **314**(Dec.), 1424.
- AHARONIAN, F. *et al.* (H.E.S.S. COLLABORATION) 2006f. HESS Observations of the Galactic Center Region and Their Possible Dark Matter Interpretation. *Physical Review Letters*, **97**(22), 221102–+.

- AHARONIAN, F. *et al.* (HEGRA COLLABORATION) 2006g. Observations of 14 young open star clusters with the HEGRA system of Cherenkov telescopes. *A&A*, **454**(Aug.), 775–779.
- AHARONIAN, F. *et al.* (H.E.S.S. COLLABORATION) 2006h. Observations of the Crab nebula with HESS. *A&A*, **457**(Oct.), 899–915.
- AHARONIAN, F. *et al.* (H.E.S.S. COLLABORATION) 2006i. The H.E.S.S. Survey of the Inner Galaxy in Very High Energy Gamma Rays. *ApJ*, **636**(Jan.), 777–797.
- AHARONIAN, F. *et al.* (H.E.S.S. COLLABORATION) 2007. Detection of extended very-high-energy gamma-ray emission towards the young stellar cluster Westerlund 2. *ArXiv Astrophysics e-prints*, Mar.
- AHARONIAN, F. A. 2000. TeV gamma rays from BL Lac objects due to synchrotron radiation of extremely high energy protons. *New Astronomy*, **5**, 377.
- AHARONIAN, F. A. 2001. TeV Blazars and Cosmic Infrared Background Radiation. *Page 250 of: SCHLICKEISER, R. (ed), Proceedings of 27th ICRC, Highlight papers, Hamburg.*
- AHARONIAN, F. A. 2004. *Very high energy cosmic gamma radiation : a crucial window on the extreme Universe*. Very high energy cosmic gamma radiation : a crucial window on the extreme Universe, by F.A. Aharonian. River Edge, NJ: World Scientific Publishing, 2004.
- AHARONIAN, F. A. *et al.* (HEGRA COLLABORATION) 1999a. The temporal characteristics of the TeV gamma-radiation from MKN 501 in 1997. I. Data from the stereoscopic imaging atmospheric Cherenkov telescope system of HEGRA. *A&A*, **342**(Feb.), 69–86.
- AHARONIAN, F. A. *et al.* (HEGRA COLLABORATION) 1999b. The time averaged TeV energy spectrum of MKN 501 of the extraordinary 1997 outburst as measured with the stereoscopic Cherenkov telescope system of HEGRA. *Astronomy and Astrophysics*, **349**, 11.
- AHARONIAN, F. A. *et al.* (HEGRA COLLABORATION) 2001. Evidence for TeV gamma ray emission from Cassiopeia A. *Astronomy and Astrophysics*, **370**, 112.
- AHARONIAN, F. A. *et al.* (HEGRA COLLABORATION) 2002a. TeV gamma rays from the blazar H 1426+428 and the diffuse extragalactic background radiation. *Astronomy and Astrophysics*, **384**, L23.
- AHARONIAN, F. A. *et al.* (HEGRA COLLABORATION) 2002b. Variations of the TeV energy spectrum at different flux levels of Mkn 421 observed with the HEGRA system of Cherenkov telescopes. *Astronomy and Astrophysics*, **393**, 89.
- AHARONIAN, F. A. *et al.* (HEGRA COLLABORATION) 2003a. Detection of TeV Gamma-Rays from the BL Lac 1ES1959+650 in its low states and during a major outburst in 2002. *Astronomy and Astrophysics*, **406**, L9.
- AHARONIAN, F. A. *et al.* (HEGRA COLLABORATION) 2003b. Is the Giant Radio Galaxy M87 a TeV Gamma-Ray Emitter? *Astronomy and Astrophysics*, **403**, L1.
- AHARONIAN, F. A. *et al.* (HEGRA COLLABORATION) 2003c. Observations of H1426+428 with HEGRA - Observations in 2002 and reanalysis of 1999&2000 data. *Astronomy and Astrophysics*, **403**, 523. astro-ph/0301437.
- AHARONIAN, F. A. *et al.* (H.E.S.S. COLLABORATION) 2004c. High-energy particle acceleration in the shell of a supernova remnant. *Nature*, **432**(Nov.), 75–77.
- ALBERT, J. *et al.* (MAGIC COLLABORATION) 2006a. Discovery of Very High Energy Gamma Rays from 1ES 1218+30.4. *ApJ*, **642**(May), L119–L122.

- ALBERT, J. *et al.* (MAGIC COLLABORATION) 2006b. Discovery of Very High Energy  $\gamma$ -Rays from Markarian 180 Triggered by an Optical Outburst. *ApJ*, **648**(Sept.), L105–L108.
- ALBERT, J. *et al.* (MAGIC COLLABORATION) 2006c. Observations of Mkn 421 with the MAGIC Telescope. *ArXiv Astrophysics e-prints*, astro-ph/0603478.
- ALBERT, J. *et al.* (MAGIC COLLABORATION) 2007a. Detection of Very High Energy Radiation from the BL Lacertae Object PG 1553+113 with the MAGIC Telescope. *ApJ*, **654**(Jan.), L119–L122.
- ALBERT, J. *et al.* (MAGIC COLLABORATION) 2007b. Discovery of very high energy gamma-ray emission from the low-frequency peaked BL Lac object BL Lacertae. *ArXiv Astrophysics e-prints*, Mar.
- ALBERT, J. *et al.* (MAGIC COLLABORATION) 2007c. Variable VHE gamma-ray emission from Markarian 501. *ArXiv Astrophysics e-prints*, Feb.
- ALBERT, J. *et al.* (MAGIC COLLABORATION) 2007d. Very high energy gamma-ray observations during moonlight and twilight with the MAGIC telescope. *ArXiv Astrophysics e-prints*, Feb.
- ANTONI, T., APEL, W. D., BADEA, A. F., BEKK, K., BERCUCI, A., BLÜMER, J., BOZDOG, H., BRANCUS, I. M., CHILINGARIAN, A., DAUMILLER, K., DOLL, P., ENGEL, R., ENGLER, J., FESSLER, F., GILS, H. J., GLASSTETTER, R., HAUNGS, A., HECK, D., HÖRANDEL, J. R., KAMPERT, K.-H., KLAGES, H. O., MAIER, G., MATHES, H. J., MAYER, H. J., MILKE, J., MÜLLER, M., OBENLAND, R., OEHLISCHLÄGER, J., OSTAPCHENKO, S., PETCU, M., REBEL, H., RISSE, A., RISSE, M., ROTH, M., SCHATZ, G., SCHIELER, H., SCHOLZ, J., THOUW, T., ULRICH, H., VAN BUREN, J., VARDANYAN, A., WEINDL, A., WOCHOLE, J., & ZABIEROWSKI, J. 2005. KASCADE measurements of energy spectra for elemental groups of cosmic rays: Results and open problems. *Astroparticle Physics*, **24**(Sept.), 1–2.
- BARTHEL, P. D., CONWAY, J. E., MYERS, S. T., PEARSON, T. J., & READHEAD, A. C. S. 1995. New superluminal quasar 1633 + 382 and the blazar-gamma-ray connection. *ApJ*, **444**(May), L21–L24.
- BEALL, J. H., & BEDNAREK, W. 1999. On the Hadronic Beam Model for Gamma-Ray Production in Blazars. *ApJ*, **510**(Jan.), 188–196.
- BEDNAREK, W. 2005. GeV gamma-rays and TeV neutrinos from very massive compact binary systems: the case of WR 20a. *MNRAS*, **363**(Oct.), L46–L50.
- BEILICKE, M. 2005. *Entdeckung einer unidentifizierten, ausgedehnten TeV- $\gamma$ -Quelle HESS J1303-631 und Bestätigung der Radiogalaxie M 87 als TeV- $\gamma$ -Quelle mit den H.E.S.S.-Cherenkov-Teleskopen*. Ph.D. thesis, Universität Hamburg.
- BELLONI, T., & MEREGHETTI, S. 1994. ROSAT observation of the giant HII region RCW 49. *A&A*, **286**(June), 935–942.
- BENAGLIA, P., & ROMERO, G. E. 2003. Gamma-ray emission from Wolf-Rayet binaries. *A&A*, **399**(Mar.), 1121–1134.
- BENBOW, W., COSTAMANTE, L., & GIEBELS, B. 2006. H.E.S.S. detects historically high fluxes of Very High Energy gamma-rays from PKS 2155-304. *The Astronomer's Telegram*, **867**(July), 1–+.
- BERNLÖHR, K. 1999. Atmospheric effects on the Cherenkov technique. *Pages 276–+ of: International Cosmic Ray Conference*. International Cosmic Ray Conference, vol. 5.

- BERNLÖHR, K. 2000. Impact of atmospheric parameters on the atmospheric Cherenkov technique\*. *Astroparticle Physics*, **12**(Jan.), 255–268.
- BERNLÖHR, K. 2001. *Corsika and sim\_hessarray - Simulation of the imaging atmospheric Cherenkov technique for the H.E.S.S. experiment*. Report. Humboldt Universität, Berlin.
- BERNLÖHR, K., CARROL, O., CORNILS, R., *et al.* 2003. The optical system of the H.E.S.S. imaging atmospheric Cherenkov telescopes, Part I: layout and components of the system. *Astroparticle Physics*.
- BERNSTEIN, R. A., FREEDMAN, W. L., & MADORE, B. F. 2002. The First Detections of the Extragalactic Background Light at 3000, 5500, and 8000 Å. I. Results. *Astronomy and Astrophysics*, **571**, 56.
- BERNSTEIN, R. A., FREEDMAN, W. L., & MADORE, B. F. 2005. Corrections of Errors in “The First Detections of the Extragalactic Background Light at 3000, 5500, and 8000 Å. I, II, and III” (*ApJ*, 571; 56, 85, 107 [2002]). *ApJ*, **632**(Oct.), 713–717.
- BŁAŻEJOWSKI, M., BLAYLOCK, G., BOND, I. H., BRADBURY, S. M., BUCKLEY, J. H., CARTER-LEWIS, D. A., CELIK, O., COGAN, P., CUI, W., DANIEL, M., DUKE, C., FALCONE, A., FEGAN, D. J., FEGAN, S. J., FINLEY, J. P., FORTSON, L., GAMMELL, S., GIBBS, K., GILLANDERS, G. G., GRUBE, J., GUTIERREZ, K., HALL, J., HANNA, D., HOLDER, J., HORAN, D., HUMENSKY, B., KENNY, G., KERTZMAN, M., KIEDA, D., KILDEA, J., KNAPP, J., KOSACK, K., KRAWCZYNSKI, H., KRENNRICH, F., LANG, M., LEBOHEC, S., LINTON, E., LLOYD-EVANS, J., MAIER, G., MENDOZA, D., MILOVANOVIC, A., MORIARTY, P., NAGAI, T. N., ONG, R. A., POWER-MOONEY, B., QUINN, J., QUINN, M., RAGAN, K., REYNOLDS, P. T., REBILLOT, P., ROSE, H. J., SCHROEDTER, M., SEMBROSKI, G. H., SWORDY, S. P., SYSON, A., VALCAREL, L., VASSILIEV, V. V., WAKELY, S. P., WALKER, G., WEEKES, T. C., WHITE, R., ZWEERINK, J., MOCHEJSKA, B., SMITH, B., ALLER, M., ALLER, H., TERÄSRANTA, H., BOLTWOOD, P., SADUN, A., STANEK, K., ADAMS, E., FOSTER, J., HARTMAN, J., LAI, K., BÖTTCHER, M., REIMER, A., & JUNG, I. 2005. A Multiwavelength View of the TeV Blazar Markarian 421: Correlated Variability, Flaring, and Spectral Evolution. *ApJ*, **630**(Sept.), 130–141.
- BLOOM, S. D., & MARSCHER, A. P. 1996. An Analysis of the Synchrotron Self-Compton Model for the Multi-Wave Band Spectra of Blazars. *ApJ*, **461**(Apr.), 657–+.
- BONANOS, A. Z., STANEK, K. Z., UDALSKI, A., WYRZYKOWSKI, L., ŻEBRUŃ, K., KUBIAK, M., SZYMAŃSKI, M. K., SZEWCZYK, O., PIETRZYŃSKI, G., & SOSZYŃSKI, I. 2004. WR 20a Is an Eclipsing Binary: Accurate Determination of Parameters for an Extremely Massive Wolf-Rayet System. *ApJ*, **611**(Aug.), L33–L36.
- BRAND, J., & BLITZ, L. 1993. The Velocity Field of the Outer Galaxy. *A&A*, **275**(Aug.), 67–+.
- BROWN, T. M., KIMBLE, R. A., FERGUSON, H. C., GARDNER, J. P., COLLINS, N. R., & HILL, R. S. 2000. Measurements of the Diffuse Ultraviolet Background and the Terrestrial Airglow with the Space Telescope Imaging Spectrograph. *AJ*, **120**(Aug.), 1153–1159.
- BUCKLEY, J. H., AKERLOF, C. W., BILLER, S., CARTER-LEWIS, D. A., CATANESE, M., CAWLEY, M. F., CONNAUGHTON, V., FEGAN, D. J., FINLEY, J. P., GAIDOS, J., HILLAS, A. M., KARTJE, J. F., KOENIGL, A., KRENNRICH, F., LAMB, R. C., LESSARD, R., MACOMB, D. J., MATTOX, J. R., MCENERY, J. E., MOHANTY, G., QUINN, J., RODGERS, A. J., ROSE, H. J., SCHUBNEL, M. S., SEMBROSKI, G., SMITH, P. S., WEEKES, T. C., WILSON, C., & ZWEERINK, J. 1996. Gamma-Ray Variability of the BL Lacertae Object Markarian 421. *ApJ*, **472**(Nov.), L9+.
- BUTT, Y. M. 2007. The answer is blowing in the wind. *Nature*, **446**(Apr.), 986–987.

- BYKOV, A. M. 2001. Particle Acceleration and Nonthermal Phenomena in Superbubbles. *Space Science Reviews*, **99**(Oct.), 317–326.
- BYKOV, A. M., & TOPTYGIN, I. N. 1987. Effect of shocks on interstellar turbulence and cosmic-ray dynamics. *Ap&SS*, **138**(Nov.), 341–354.
- CAMBRÉSY, L., REACH, W. T., BEICHMAN, C. A., & JARRETT, T. H. 2001. The Cosmic Infrared Background at 1.25 and 2.2 Microns Using DIRBE and 2MASS: A Contribution Not Due to Galaxies? *The Astrophysical Journal*, **555**, 563.
- CARRARO, G., & MUNARI, U. 2004. A multicolour CCD photometric study of the open clusters NGC 2866, Pismis 19, Westerlund 2, ESO96-SC04, NGC 5617 and NGC 6204. *MNRAS*, **347**(Jan.), 625–631.
- CASSE, M., & PAUL, J. A. 1980. Local gamma rays and cosmic-ray acceleration by supersonic stellar winds. *ApJ*, **237**(Apr.), 236–243.
- CASTOR, J., MCCRAY, R., & WEAVER, R. 1975. Interstellar bubbles. *ApJ*, **200**(Sept.), L107–L110.
- CATANESE, M., AKERLOF, C. W., BADRAN, H. M., BILLER, S. D., BOND, I. H., BOYLE, P. J., BRADBURY, S. M., BUCKLEY, J. H., BURDETT, A. M., BUSSONS GORDO, J., CARTER-LEWIS, D. A., CAWLEY, M. F., CONNAUGHTON, V., FEGAN, D. J., FINLEY, J. P., GAIDOS, J. A., HALL, T., HILLAS, A. M., KRENNRICH, F., LAMB, R. C., LESSARD, R. W., MASTERSON, C., MCENERY, J. E., MOHANTY, G., QUINN, J., RODGERS, A. J., ROSE, H. J., SAMUELSON, F. W., SCHUBNELL, M. S., SEMBROSKI, G. H., SRINIVASAN, R., WEEKES, T. C., WILSON, C. W., & ZWEERINK, J. 1998. Discovery of Gamma-Ray Emission above 350 GeV from the BL Lacertae Object 1ES 2344+514. *ApJ*, **501**(July), 616–+.
- CESARSKY, C. J., & MONTMERLE, T. 1983. Gamma rays from active regions in the galaxy - The possible contribution of stellar winds. *Space Science Reviews*, **36**(Oct.), 173–193.
- CHADWICK, P. M., LYONS, K., MCCOMB, T. J. L., ORFORD, K. J., OSBORNE, J. L., RAYNER, S. M., SHAW, S. E., TURVER, K. E., & WIECZOREK, G. J. 1999. Very High Energy Gamma Rays from PKS 2155-304. *ApJ*, **513**(Mar.), 161–167.
- CHEN, W., & WHITE, R. L. 1991. Inverse-Compton gamma-ray emission from chaotic, early-type stellar winds and its detectability by Gamma Ray Observatory. *ApJ*, **381**(Nov.), L63–L66.
- CHURCHWELL, E., WHITNEY, B. A., BABLER, B. L., INDEBETOUW, R., MEADE, M. R., WATSON, C., WOLFF, M. J., WOLFIRE, M. G., BANIA, T. M., BENJAMIN, R. A., CLEMENS, D. P., COHEN, M., DEVINE, K. E., DICKEY, J. M., HEITSCH, F., JACKSON, J. M., KOBULNICKY, H. A., MARSTON, A. P., MATHIS, J. S., MERCER, E. P., STAUFFER, J. R., & STOLOVY, S. R. 2004. RCW 49 at Mid-Infrared Wavelengths: A GLIMPSE from the Spitzer Space Telescope. *ApJS*, **154**(Sept.), 322–327.
- CONTI, P. S., & CROWTHER, P. A. 2004. MSX mid-infrared imaging of massive star birth environments - II. Giant HII regions. *MNRAS*, **355**(Dec.), 899–917.
- CORNILS, R. 2006. *Justierung und Abbildungsfunktion der H.E.S.S.-Reflektoren sowie Untersuchung der ultraleuchtkräftigen Infrarotgalaxie Arp 220 mit dem H.E.S.S.-Teleskopsystem*. Ph.D. thesis, Universität Hamburg.
- CORNILS, R., GILLESSEN, S., JUNG, I., *et al.* 2003. The optical system of the H.E.S.S. imaging atmospheric Cherenkov telescopes, Part II: mirror alignment and point spread function. *Astroparticle Physics*, **20**, 129.
- CORTINA, J., *et al.* 2005. Technical Performance of the MAGIC Telescope. *Page 359 of: International Cosmic Ray Conference*, vol. 5.

- COSTAMANTE, L., GHISELLINI, G., GIOMMI, P., *et al.* 2001. Extreme Synchrotron BL Lac Objects – Stretching the Blazar Sequence. *Astronomy and Astrophysics*, **371**, 512.
- COSTAMANTE, L., AHARONIAN, F., GHISELLINI, G., & HORNS, D. 2003. The SED of the TeV BLLac 1ES 1426+428 after correction for the TeV-IR absorption. *New Astronomy Review*, **47**(Oct.), 677–680.
- CROWTHER, P. A., HADFIELD, L. J., CLARK, J. S., NEGUERUELA, I., & VACCA, W. D. 2006. A census of the Wolf-Rayet content in Westerlund 1 from near-infrared imaging and spectroscopy. *MNRAS*, **372**(Nov.), 1407–1424.
- DAR, A., & LAOR, A. 1997. Hadronic Production of TeV Gamma-Ray Flares from Blazars. *ApJ*, **478**(Mar.), L5+.
- DAUM, A., HERMANN, G., HESS, M., *et al.* 1997. First results on the performance of the HEGRA IACT array. *Astroparticle Physics*, **8**, 1.
- DAVIES, J. M., & COTTON, E. S. 1957. Design of the Quartermaster Solar Furnace. *Journal of Solar Energy*, **1**, 16.
- DE JAGER, O. C., STECKER, F. W., & SALAMON, M. H. 1994. Estimate of the Intergalactic Infrared Radiation Field from Gamma-Ray Observations of the Galaxy MARKARIAN:421. *Nature*, **369**(May), 294+.
- DERMER, C. D., SCHLICKEISER, R., & MASTICHIADIS, A. 1992. High-energy gamma radiation from extragalactic radio sources. *A&A*, **256**(Mar.), L27–L30.
- DOLE, H., LAGACHE, G., PUGET, J.-L., CAPUTI, K. I., FERNÁNDEZ-CONDE, N., LE FLOC'H, E., PAPOVICH, C., PÉREZ-GONZÁLEZ, P. G., RIEKE, G. H., & BLAYLOCK, M. 2006. The cosmic infrared background resolved by Spitzer. Contributions of mid-infrared galaxies to the far-infrared background. *A&A*, **451**(May), 417–429.
- DOMINGO-SANTAMARÍA, E., & TORRES, D. F. 2006. Hadronic processes within collective stellar winds. *A&A*, **448**(Mar.), 613–622.
- DOUGHERTY, S. M., & WILLIAMS, P. M. 2000. Non-thermal emission in Wolf-Rayet stars: are massive companions required? *MNRAS*, **319**(Dec.), 1005–1010.
- DRURY, L. O'C., AHARONIAN, F. A., & VÖLK, H. J. 1994. The Gamma-Ray Visibility of Supernova Remnants. A test of Cosmic Ray Origins. *Astronomy and Astrophysics*, **287**, 959.
- DUBE, R. R., WICKES, W. C., & WILKINSON, D. T. 1979. Upper limit on the extragalactic background light. *ApJ*, **232**(Sept.), 333–340.
- DUBUS, G. 2006. Gamma-ray binaries: pulsars in disguise? *A&A*, **456**(Sept.), 801–817.
- DWEK, E., & ARENDT, R. G. 1998. A Tentative Detection of the Cosmic Infrared Background at 3.5  $\mu\text{m}$  from COBE/DIRBE Observation. *The Astrophysical Journal*, **508**, L9.
- DWEK, E., & KRENNRICH, F. 2005. Simultaneous Constraints on the Spectrum of the Extragalactic Background Light and the Intrinsic TeV Spectra of Markarian 421, Markarian 501, and H1426+428. *ApJ*, **618**(Jan.), 657–674.
- DWEK, E., & SLAVIN, J. 1994. On the determination of the cosmic infrared background radiation from the high-energy spectrum of extragalactic gamma-ray sources. *ApJ*, **436**(Dec.), 696–704.
- DWEK, E., KRENNRICH, F., & ARENDT, R. G. 2005a. Is There an Imprint of Primordial Stars in the TeV  $\gamma$ -Ray Spectrum of Blazars? *ApJ*, **634**(Nov.), 155–160.

- DWEK, E., ARENDT, R. G., & KRENNRICH, F. 2005b. The Near-Infrared Background: Interplanetary Dust or Primordial Stars? *ApJ*, **635**(Dec.), 784–794.
- EADIE, W. T., DRIJARD, D., JAMES, F. E., ROOS, M., & SADOULET, B. 1988. *Statistical Methods in Experimental Physics*. North-Holland Publishing Company; Amsterdam, New-York, Oxford.
- EDELSTEIN, J., BOWYER, S., & LAMPTON, M. 2000. Reanalysis of Voyager Ultraviolet Spectrometer Limits to the Extreme-Ultraviolet and Far-Ultraviolet Diffuse Astronomical Flux. *ApJ*, **539**(Aug.), 187–190.
- EICHLER, D., & USOV, V. 1993. Particle acceleration and nonthermal radio emission in binaries of early-type stars. *ApJ*, **402**(Jan.), 271–279.
- ELBAZ, D., CESARSKY, C. J., CHANIAL, P., AUSSEL, H., FRANCESCHINI, A., FADDA, D., & CHARY, R. R. 2002. The bulk of the cosmic infrared background resolved by ISOCAM. *A&A*, **384**(Mar.), 848–865.
- ELLIS, J., OLIVE, K. A., SANTOSO, Y., & SPANOS, V. C. 2003. Supersymmetric Dark Matter in Light of WMAP. *ArXiv High Energy Physics - Phenomenology e-prints*, Mar.
- ELVIS, M., PLUMMER, D., SCHACHTER, J., & FABBIANO, G. 1992. The Einstein Slew Survey. *ApJS*, **80**(May), 257–303.
- FAZIO, G. G., & STECKER, F. W. 1970. Predicted High Energy Break in the Isotropic Gamma Ray Spectrum: a Test of Cosmological Origin. *Nature*, **226**, 135–+.
- FAZIO, G. G., ASHBY, M. L. N., BARMBY, P., HORA, J. L., HUANG, J.-S., PAHRE, M. A., WANG, Z., WILLNER, S. P., ARENDT, R. G., MOSELEY, S. H., BRODWIN, M., EISENHARDT, P., STERN, D., TOLLESTRUP, E. V., & WRIGHT, E. L. 2004. Number Counts at  $3 \mu\text{m} < \lambda < 10 \mu\text{m}$  from the Spitzer Space Telescope. *ApJS*, **154**(Sept.), 39–43.
- FINKBEINER, D. P., DAVIS, M., & SCHLEGEL, D. J. 2000. Detection of a Far-Infrared Excess with DIRBE at 60 and 100 Microns. *The Astrophysical Journal*, **544**, 81.
- FINLEY, J. P., & THE VERITAS COLLABORATION. 2001 (Aug.). The Whipple Observatory Granite III Upgrade Program. *Pages 2827–+ of: International Cosmic Ray Conference*.
- FOSSATI, G., MARASCHI, L., CELOTTI, A., COMASTRI, A., & GHISELLINI, G. 1998. A unifying view of the spectral energy distributions of blazars. *MNRAS*, **299**(Sept.), 433–448.
- FRAYER, D. T., HUYNH, M. T., CHARY, R., DICKINSON, M., ELBAZ, D., FADDA, D., SURACE, J. A., TEPLITZ, H. I., YAN, L., & MOBASHER, B. 2006. Spitzer 70 Micron Source Counts in GOODS-North. *ApJ*, **647**(Aug.), L9–L12.
- FUNK, S., HERMANN, G., HINTON, J., BERGE, D., BERNLÖHR, K., HOFMANN, W., NAYMAN, P., TOUSSENEL, F., & VINCENT, P. 2004. The trigger system of the H.E.S.S. telescope array. *Astroparticle Physics*, **22**(Nov.), 285–296.
- GAIDOS, J. A., AKERLOF, C. W., BILLER, S. D., BOYLE, P. J., BRESLIN, A. C., BUCKLEY, J. H., CARTER-LEWIS, D. A., CATANESE, M., CAWLEY, M. F., FEGAN, D. J., FINLEY, J. P., HILLAS, A. M., KRENNRICH, F., LAMB, R. C., LESSARD, R., MCENERY, J., MOHANTY, G., MORIARTY, P., QUINN, J., RODGERS, A., ROSE, H. J., SAMUELSON, F., SCHUBNELL, M. S., SEMBROSKI, G., SRINIVASAN, R., WEEKES, T. C., WILSON, C. L., & ZWEERINK, J. 1996. Very Rapid and Energetic Bursts of TeV Photons from the Active Galaxy Markarian 421. *Nature*, **383**, 319–+.

- GAISSER, T. K. 2006. The Cosmic-ray Spectrum: from the knee to the ankle. *Journal of Physics Conference Series*, **47**(Oct.), 15–20.
- GEHRELS, N., & MICHELSON, P. 1999. GLAST: the next-generation high energy gamma-ray astronomy mission. *Astroparticle Physics*, **11**(June), 277–282.
- GEHRELS, N., CHINCARINI, G., GIOMMI, P., MASON, K. O., NOUSEK, J. A., WELLS, A. A., WHITE, N. E., BARTHELMI, S. D., BURROWS, D. N., COMINSKY, L. R., HURLEY, K. C., MARSHALL, F. E., MÉSZÁROS, P., ROMING, P. W. A., ANGELINI, L., BARBIER, L. M., BELLONI, T., CAMPANA, S., CARAVEO, P. A., CHESTER, M. M., CITTERIO, O., CLINE, T. L., CROPPER, M. S., CUMMINGS, J. R., DEAN, A. J., FEIGELSON, E. D., FENIMORE, E. E., FRAIL, D. A., FRUCHTER, A. S., GARMIRE, G. P., GENDREAU, K., GHISELLINI, G., GREINER, J., HILL, J. E., HUNSBERGER, S. D., KRIMM, H. A., KULKARNI, S. R., KUMAR, P., LEBRUN, F., LLOYD-RONNING, N. M., MARKWARDT, C. B., MATTSON, B. J., MUSHOTZKY, R. F., NORRIS, J. P., OSBORNE, J., PACZYNSKI, B., PALMER, D. M., PARK, H.-S., PARSONS, A. M., PAUL, J., REES, M. J., REYNOLDS, C. S., RHOADS, J. E., SASSEEN, T. P., SCHAEFER, B. E., SHORT, A. T., SMALE, A. P., SMITH, I. A., STELLA, L., TAGLIAFERRI, G., TAKAHASHI, T., TASHIRO, M., TOWNSLEY, L. K., TUELLER, J., TURNER, M. J. L., VIETRI, M., VOGES, W., WARD, M. J., WILLINGALE, R., ZERBI, F. M., & ZHANG, W. W. 2004. The Swift Gamma-Ray Burst Mission. *ApJ*, **611**(Aug.), 1005–1020.
- GEORGANOPOULOS, M., & KAZANAS, D. 2003. Decelerating Flows in TeV Blazars: A Resolution to the BL Lacertae-FR I Unification Problem. *ApJ*, **594**(Sept.), L27–L30.
- GINZBURG, V. L., & SYROVATSKII, S. I. 1969. Developments in the Theory of Synchrotron Radiation and its Reabsorption. *Annual Review of Astronomy and Astrophysics*, **7**, 375.
- GIOMMI, P., BLUSTIN, A. J., CAPALBI, M., COLAFRANCESCO, S., CUCCHIARA, A., FUHRMANN, L., KRIMM, H. A., MARCHILI, N., MASSARO, E., PERRI, M., TAGLIAFERRI, G., TOSTI, G., TRAMACERE, A., BURROWS, D. N., CHINCARINI, G., FALCONE, A., GEHRELS, N., KENNEA, J., & SAMBRUNA, R. 2006. Swift and infra-red observations of the blazar 3C 454.3 during the giant X-ray flare of May 2005. *A&A*, **456**(Sept.), 911–916.
- GIROLETTI, M., GIOVANNINI, G., TAYLOR, G. B., & FALOMO, R. 2004. A Sample of Low-Redshift BL Lacertae Objects. I. The Radio Data. *ApJ*, **613**(Oct.), 752–769.
- GOLDWURM, A., CARAVEO, P. A., & BIGNAMI, G. F. 1987. Diffuse Einstein X-ray emission from the region of RCW 49, a bright southern emission nebula. *ApJ*, **322**(Nov.), 349–352.
- GORJIAN, V., WRIGHT, E. L., & CHARY, R. R. 2000. Tentative Detection of the Cosmic Infrared Background at 2.2 and 3.5 Microns Using Ground-based and Space-based Observations. *The Astrophysical Journal*, **536**, 550.
- GÖTTING, N. 2007. *Nachweis von TeV-Gamma-Strahlung aus der Richtung der Blazare H1426+428 und 1ES1959+650 sowie der Radiogalaxie M87 mit den HEGRA-Cherenkov-Teleskopen*. Ph.D. thesis, Universität Hamburg.
- GOULD, R. J., & SCHRÉDER, G. P. 1967. Opacity of the Universe to High-Energy Photons. *Physical Review*, **155**(Mar.), 1408–1411.
- GREISEN, K. 1966. End to the Cosmic-Ray Spectrum? *Physical Review Letters*, **16**, 748.
- GUY, J., RENAULT, C., AHARONIAN, F. A., RIVOAL, M., & TAVERNET, J.-P. 2000. Constraints on the cosmic infra-red background based on BeppoSAX and CAT spectra of Markarian 501. *Astronomy and Astrophysics*, **359**, 419.

- HARTMAN, R. C., BERTSCH, D. L., BLOOM, S. D., CHEN, A. W., DEINES-JONES, P., ESPOSITO, J. A., FICHEL, C. E., FRIEDLANDER, D. P., HUNTER, S. D., McDONALD, L. M., SREEKUMAR, P., THOMPSON, D. J., JONES, B. B., LIN, Y. C., MICHELSON, P. F., NOLAN, P. L., TOMPKINS, W. F., KANBACH, G., MAYER-HASSELWANDER, H. A., MUCKE, A., POHL, M., REIMER, O., KNIFFEN, D. A., SCHNEID, E. J., VON MONTIGNY, C., MUKHERJEE, R., & DINGUS, B. L. 1999. Third EGRET catalog (3EG) (Hartman+, 1999). *VizieR Online Data Catalog*, **212**(Aug.), 30079+.
- HAUSER, M. G., & DWEK, E. 2001. The Cosmic Infrared Background: Measurements and Implications. *Annual Review of Astronomy and Astrophysics*, **39**, 249.
- HAUSER, M. G., ARENDT, R. G., KELSALL, T., DWEK, E., ODEGARD, N., *et al.* 1998. The COBE Diffuse Infrared Background Experiment Search for the Cosmic Infrared Background. I. Limits and Detections. *The Astrophysical Journal*, **508**, 25.
- HECK, D., KNAPP, J., CAPDEVIELLE, J. N., *et al.* 1998. CORSIKA: A Monte Carlo Code to Simulate Extensive Air Shower. Wissenschaftliche Berichte FZKA 6019. Forschungszentrum Karlsruhe. <http://www-ik3.fzk.de/heck/corsika/>.
- HEITLER, M. 1960. *The Quantum Theorie of Radiation*. Oxford, Clarendon.
- HERTZ, P., & GRINDLAY, J. E. 1984. The Einstein galactic plane survey - Statistical analysis of the complete X-ray sample. *ApJ*, **278**(Mar.), 137–149.
- HESS, V. 1912. Observation of Penetrating Radiation of seven Balloon Flights. *Physikalische Zeitschrift*, **13**, 1084.
- HILLAS, A. M. 1985. Cerenkov light images of EAS produced by primary gamma rays and by nuclei. *Page 445 of: 19th International Cosmic Ray Conference*, vol. 3.
- HILLAS, A. M. 2006. Cosmic Rays: Recent Progress and some Current Questions. *ArXiv Astrophysics e-prints*, July.
- HINTON, J. A. 2004. The status of the HESS project. *New Astronomy Review*, **48**(Apr.), 331–337.
- HOFMANN, W., JUNG, I., KONOPELKO, A., KRAWCZYNSKI, H., LAMPEITL, H., & PÜHLHOFER, G. 1999. Comparison of techniques to reconstruct VHE gamma-ray showers from multiple stereoscopic Cherenkov images. *Astroparticle Physics*, **12**(Nov.), 135–143.
- HOFMANN, W., LAMPEITL, H., KONOPELKO, A., & KRAWCZYNSKI, H. 2000. Improved energy resolution for VHE gamma-ray astronomy with systems of Cherenkov telescopes. *Astroparticle Physics*, **12**, 207.
- HORAN, D., & THE VERITAS COLLABORATION. 2001. Observations of the BL Lac Object, 1H1426+428 at TeV Gamma-ray Energies. *Page 324 of: AIP Conf. Proc. 587: Gamma 2001: Gamma-Ray Astrophysics*.
- HORNS, D. 2001. *Suche nach TeV-Photonen aus intergalaktischen Kaskaden und nach Bose-Einstein-Kondensaten in TeV-Photonen*. Ph.D. thesis, Fachbereich Physik der Universität Hamburg. [dissertation.de](http://dissertation.de).
- HORNS, D. 2007. *private communication*.
- JOKIPII, J. R. 1968. Acceleration of Cosmic Rays at the Solar-Wind Boundary. *ApJ*, **152**(June), 799+.
- JONES, T. W., O'DELL, S. L., & STEIN, W. A. 1974. Physics of Compact Nonthermal Sources. Theory of Radiation Processes. *ApJ*, **188**(Mar.), 353–368.

- KARLE, A., AHRENS, J., BAHCALL, J. N., & OTHERS. 2003. IceCube - the next generation neutrino telescope at the South Pole. *Nuclear Physics B Proceedings Supplements*, **118**(Apr.), 388–395.
- KASHLINSKY, A. 2005. Cosmic infrared background and early galaxy evolution [review article]. *Phys. Rep.*, **409**(Apr.), 361–438.
- KASHLINSKY, A., & ODENWALD, S. 2000. Clustering of the Diffuse Infrared Light from the COBE DIRBE Maps. III. Power Spectrum Analysis and Excess Isotropic Component of Fluctuations. *The Astrophysical Journal*, **528**, 74.
- KASHLINSKY, A., MATHER, J.C., ODENWALD, S., & HAUSER, M.G. 1996. Clustering of the Diffuse Infrared Light from the COBE DIRBE Maps. I. C(0) and Limits on the Near-Infrared Background. *The Astrophysical Journal*, **470**, 681.
- KASHLINSKY, A., ARENDT, R. G., MATHER, J., & MOSELEY, S. H. 2005. Tracing the first stars with fluctuations of the cosmic infrared background. *Nature*, **438**(Nov.), 45–50.
- KATAOKA, J., MATTOX, J. R., QUINN, J., KUBO, H., MAKINO, F., TAKAHASHI, T., INOUE, S., HARTMAN, R. C., MADEJSKI, G. M., SREEKUMAR, P., & WAGNER, S. J. 1999. Multi-wavelength observations of the TeV blazar MRK 501 in March 1996. The first report of the detection by EGRET. *Astroparticle Physics*, **11**(June), 149–151.
- KATARZYŃSKI, K., GHISELLINI, G., TAVECCHIO, F., GRACIA, J., & MARASCHI, L. 2006. Hard TeV spectra of blazars and the constraints to the infrared intergalactic background. *MNRAS*, **368**(May), L52–L56.
- KATZ, U. F. 2006. KM3NeT: Towards a km<sup>3</sup> Mediterranean neutrino telescope. *Nuclear Instruments and Methods in Physics Research A*, **567**(Nov.), 457–461.
- KIFUNE, T. 1999. Invariance Violation Extends the Cosmic-Ray Horizon? *ApJ*, **518**(June), L21–L24.
- KLEPACH, E. G., PTUSKIN, V. S., & ZIRAKASHVILI, V. N. 2000. Cosmic ray acceleration by multiple spherical shocks. *Astroparticle Physics*, **13**(May), 161–172.
- KNEISKE, T. M., MANNHEIM, K., & HARTMANN, D. H. 2002. Implications of cosmological gamma-ray absorption. I. Evolution of the metagalactic radiation field. *A&A*, **386**(Apr.), 1–11.
- KONIGL, A. 1981. Relativistic jets as X-ray and gamma-ray sources. *ApJ*, **243**(Feb.), 700–709.
- KRAWCZYNSKI, H., COPPI, P. S., MACCARONE, T., & AHARONIAN, F. A. 2000. X-ray/TeV-gamma-ray observations of several strong flares of Mkn 501 during 1997 and implications. *A&A*, **353**(Jan.), 97–107.
- KRAWCZYNSKI, H., SAMBRUNA, R., KOHNLE, A., COPPI, P. S., AHARONIAN, F., AKHPERJANIAN, A., BARRIO, J., BERNLÖHR, K., BÖRST, H., BOJAHN, H., BOLZ, O., CONTRERAS, J., CORTINA, J., DENNINGHOFF, S., FONSECA, V., GONZALEZ, J., GÖTTING, N., HEINZELMANN, G., HERMANN, G., HEUSLER, A., HOFMANN, W., HORNS, D., IBARRA, A., JUNG, I., KANKANYAN, R., KESTEL, M., KETTLER, J., KONOPELKO, A., KORNMAYER, H., KRANICH, D., LAMPEITL, H., LORENZ, E., LUCARELLI, F., MAGNUSSEN, N., MANG, O., MEYER, H., MIRZOYAN, R., MORALEJO, A., PADILLA, L., PANTER, M., PLAGA, R., PLYASHESHNIKOV, A., PÜHLHOFER, G., RAUTERBERG, G., RÖHRING, A., RHODE, W., ROWELL, G., SAHAKIAN, V., SAMORSKI, M., SCHILLING, M., SCHRÖDER, F., SIEMS, M., STAMM, W., TLUCZYKONT, M., VÖLK, H. J., WIEDNER, C. A., & WITTEK, W. 2001. Simultaneous X-Ray and TeV Gamma-Ray Observation of the TeV Blazar Markarian 421 during 2000 February and May. *ApJ*, **559**(Sept.), 187–195.

- KRAWCZYNSKI, H., HUGHES, S. B., HORAN, D., AHARONIAN, F., ALLER, M. F., ALLER, H., BOLTWOOD, P., BUCKLEY, J., COPPI, P., FOSSATI, G., GÖTTING, N., HOLDER, J., HORNS, D., KURTANIDZE, O. M., MARSCHER, A. P., NIKOLASHVILI, M., REMILLARD, R. A., SADUN, A., & SCHRÖDER, M. 2004. Multiwavelength Observations of Strong Flares from the TeV Blazar 1ES 1959+650. *ApJ*, **601**(Jan.), 151–164.
- KRENNRICH, F., BOND, I. H., BRADBURY, S. M., BUCKLEY, J. H., CARTER-LEWIS, D. A., CUI, W., DE LA CALLE PEREZ, I., FEGAN, D. J., FEGAN, S. J., FINLEY, J. P., GAIDOS, J. A., GIBBS, K., GILLANDERS, G. H., HALL, T. A., HILLAS, A. M., HOLDER, J., HORAN, D., JORDAN, M., KERTZMAN, M., KIEDA, D., KILDEA, J., KNAPP, J., KOSACK, K., LANG, M. J., LEBOHEC, S., MORIARTY, P., MÜLLER, D., ONG, R. A., PALLASSINI, R., PETRY, D., QUINN, J., REAY, N. W., REYNOLDS, P. T., ROSE, H. J., SEMBROSKI, G. H., SIDWELL, R., STANTON, N., SWORDY, S. P., VASSILIEV, V. V., WAKELY, S. P., & WEEKES, T. C. 2002. Discovery of Spectral Variability of Markarian 421 at TeV Energies. *ApJ*, **575**(Aug.), L9–L13.
- KUSUNOSE, M., & TAKAHARA, F. 2006. A Structured Leptonic Jet Model of the “Orphan” TeV Gamma-Ray Flares in TeV Blazars. *ApJ*, **651**(Nov.), 113–119.
- LAGACHE, G., & PUGET, J.-L. 2000. Detection of the extra-Galactic background fluctuations at 170  $\mu\text{m}$ . *Astronomy and Astrophysics*, **355**, 17.
- LAMER, G., BRUNNER, H., & STAUBERT, R. 1996. ROSAT observations of BL Lacertae objects. *A&A*, **311**(July), 384–392.
- LEINERT, C., BOWYER, S., HAIKALA, L. K., HANNER, M. S., HAUSER, M. G., LEVASSEUR-REGOURD, A.-C., MANN, I., MATTILA, K., REACH, W. T., SCHLOSSER, W., STAUDE, H. J., TOLLER, G. N., WEILAND, J. L., WEINBERG, J. L., & WITT, A. N. 1998. The 1997 reference of diffuse night sky brightness. *A&AS*, **127**(Jan.), 1–99.
- LEVENSON, L. R., WRIGHT, E. L., & JOHNSON, B. D. 2007. DIRBE Minus 2MASS: Confirming the CIRB in 40 New Regions at 2.2 and 3.5 Microns. *ArXiv e-prints*, **704**(Apr.).
- LONGAIR, M. S. 1992. *High Energy Astrophysics*. Vol. 1. Cambridge University Press.
- LONGAIR, M. S. 1994. *High Energy Astrophysics*. Vol. 2. Cambridge University Press.
- MADAU, P., & POZZETTI, L. 2000. Deep galaxy counts, extragalactic background light and the stellar baryon budget. *Monthly Notices of the Royal Astronomical Society*, **312**, L9.
- MANNHEIM, K. 1993. The proton blazar. *A&A*, **269**(Mar.), 67–76.
- MANNHEIM, K., & BIERMANN, P. L. 1989. Photomeson production in active galactic nuclei. *A&A*, **221**(Sept.), 211–220.
- MAPELLI, M., SALVATERRA, R., & FERRARA, A. 2004 (Dec.). Extragalactic Background Light: new constraints from the study of the photon-photon absorption on blazar spectra. *In*: DETTMAR, R., KLEIN, U., & SALUCCI, P. (eds), *Baryons in Dark Matter Halos*.
- MARAN, S. P. 1992. *The Astronomy and astrophysics encyclopedia*. New York : Van Nostrand Reinhold, c1992.
- MARASCHI, L., GHISELLINI, G., & CELOTTI, A. 1992. A jet model for the gamma-ray emitting blazar 3C 279. *ApJ*, **397**(Sept.), L5–L9.
- MARTIN, C., HURWITZ, M., & BOWYER, S. 1991. Spectroscopic limits to an extragalactic far-ultraviolet background. *ApJ*, **379**(Oct.), 549–563.

- MATSUMOTO, T., MATSUURA, S., MURAKAMI, H., TANAKA, M., FREUND, M., LIM, M., COHEN, M., KAWADA, M., & NODA, M. 2005. Infrared Telescope in Space Observations of the Near-Infrared Extragalactic Background Light. *ApJ*, **626**(June), 31–43.
- MATTILA, K. 1990. Observations of the extragalactic background light. *Pages 257–268 of: BOWYER, S., & LEINERT, C. (eds), IAU Symp. 139: The Galactic and Extragalactic Background Radiation.*
- MATUTE, I., LA FRANCA, F., POZZI, F., GRUPPIONI, C., LARI, C., & ZAMORANI, G. 2006. Active galactic nuclei in the mid-IR. Evolution and contribution to the cosmic infrared background. *A&A*, **451**(May), 443–456.
- MAZIN, D., & RAUE, M. 2007. New limits on the density of the extragalactic background light in the optical to the far-infrared from the spectra of all known TeV blazars. *A&A*. accepted, astro-ph/0701694.
- MAZINE, D. 2003. *Entwicklung einer Methode zur Einschränkung der Energiedichte des extragalaktischen Hintergrundlichtes mit Hilfe der gemessenen TeV-Gamma-Strahlung*. Diplomarbeit, Institut für Experimentalphysik, Universität Hamburg.
- MCCLURE-GRIFFITHS, N. M., GREEN, A. J., DICKEY, J. M., GAENSLER, B. M., HAYNES, R. F., & WIERINGA, M. H. 2001. The Southern Galactic Plane Survey: The Test Region. *ApJ*, **551**(Apr.), 394–412.
- MEREGHETTI, S., & BELLONI, T. 1996 (Feb.). Discovery of X-ray emission from the Wolf-Rayet star in Westerlund 2. *Pages 53–54 of: ZIMMERMANN, H. U., TRÜMPER, J., & YORKE, H. (eds), Roentgenstrahlung from the Universe.*
- METCALFE, L., KNEIB, J.-P., MCBREEN, B., ALTIERI, B., BIVIANO, A., DELANEY, M., ELBAZ, D., KESSLER, M. F., LEECH, K., OKUMURA, K., OTT, S., PEREZ-MARTINEZ, R., SANCHEZ-FERNANDEZ, C., & SCHULZ, B. 2003. An ISOCAM survey through gravitationally lensing galaxy clusters. I. Source lists and source counts for A370, A2218 and A2390. *A&A*, **407**(Sept.), 791–822.
- MOFFAT, A. F. J., SHARA, M. M., & POTTER, M. 1991. New Wolf-Rayet stars in Galactic open clusters - Sher 1 and the giant H II region core Westerlund 2. *AJ*, **102**(Aug.), 642–653.
- MOFFAT, A. F. J., SCHNURR, O., CHENÉ, A.-N., ST-LOUIS, N., & CASOLI, J. 2006. Keplerian Masses for the Most Massive Stars: The Very Luminous, Hydrogen-Rich Wolf-Rayet Stars. *Calibrating the Top of the Stellar M-L Relation, 26th meeting of the IAU, Joint Discussion 5, 16 August 2006, Prague, Czech Republic, JD05, #1, 5*(Aug.).
- MÜCKE, A., & PROTHEROE, R. J. 2001. A proton synchrotron blazar model for flaring in Markarian 501. *Astroparticle Physics*, **15**(Mar.), 121–136.
- MUNO, M. P., LAW, C., CLARK, J. S., DOUGHERTY, S. M., DE GRIJS, R., PORTEGIES ZWART, S., & YUSEF-ZADEH, F. 2006. Diffuse, Nonthermal X-Ray Emission from the Galactic Star Cluster Westerlund 1. *ApJ*, **650**(Oct.), 203–211.
- PAPOVICH, C., DOLE, H., EGAMI, E., LE FLOC'H, E., PÉREZ-GONZÁLEZ, P. G., ALONSO-HERRERO, A., BAI, L., BEICHMAN, C. A., BLAYLOCK, M., ENGELBRACHT, C. W., GORDON, K. D., HINES, D. C., MISSELT, K. A., MORRISON, J. E., MOULD, J., MUZEROLLE, J., NEUGEBAUER, G., RICHARDS, P. L., RIEKE, G. H., RIEKE, M. J., RIGBY, J. R., SU, K. Y. L., & YOUNG, E. T. 2004. The 24 Micron Source Counts in Deep Spitzer Space Telescope Surveys. *ApJS*, **154**(Sept.), 70–74.
- PEACOCK, J. A. 1999. *Cosmological Physics*. *Cosmological Physics*, by John A. Peacock, pp. 704. ISBN 052141072X. Cambridge, UK: Cambridge University Press, January 1999.

- PERLMAN, E. S., STOCKE, J. T., SCHACHTER, J. F., ELVIS, M., ELLINGSON, E., URRY, C. M., POTTER, M., IMPEY, C. D., & KOLCHINSKY, P. 1996. The Einstein Slew Survey Sample of BL Lacertae Objects. *ApJS*, **104**(June), 251–+.
- PERLMAN, E. S., MADEJSKI, G., GEORGANOPOULOS, M., ANDERSSON, K., DAUGHERTY, T., KROLIK, J. H., RECTOR, T., STOCKE, J. T., KORATKAR, A., WAGNER, S., ALLER, M., ALLER, H., & ALLEN, M. G. 2005. Intrinsic Curvature in the X-Ray Spectra of BL Lacertae Objects. *ApJ*, **625**(June), 727–740.
- PIATTI, A. E., BICA, E., & CLARIA, J. J. 1998. Fundamental parameters of the highly reddened young open clusters Westerlund 1 and 2. *A&AS*, **127**(Feb.), 423–432.
- PINER, B. G., & KINGHAM, K. A. 1997. A Slower Superluminal Velocity for the Quasar 1156+295. *ApJ*, **485**(Aug.), L61+.
- PITTARD, J. M., & DOUGHERTY, S. M. 2006. Radio, X-ray, and  $\gamma$ -ray emission models of the colliding-wind binary WR140. *MNRAS*, **372**(Oct.), 801–826.
- PITTARD, J. M., & STEVENS, I. R. 2002. The dominant X-ray wind in massive star binaries. *A&A*, **388**(June), L20–L23.
- POHL, M. 2002. *Einführung in die Hochenergieastrophysik*. Shaker-Verlag.
- POHL, M., & SCHLICKEISER, R. 2000. On the conversion of blast wave energy into radiation in active galactic nuclei and gamma-ray bursts. *A&A*, **354**(Feb.), 395–410.
- POHL, M., REICH, W., KRICHBAUM, T. P., STANDKE, K., BRITZEN, S., REUTER, H. P., REICH, P., SCHLICKEISER, R., FIEDLER, R. L., WALTMAN, E. B., GHIGO, F. D., & JOHNSTON, K. J. 1995. Radio observations of the  $\gamma$ -ray quasar 0528+134. Superluminal motion and an extreme scattering event. *A&A*, **303**(Nov.), 383–+.
- PRIMACK, J. R., BULLOCK, J. S., & SOMERVILLE, R. S. 2005 (Feb.). Observational Gamma-ray Cosmology. Pages 23–33 of: AHARONIAN, F. A., VÖLK, H. J., & HORNS, D. (eds), *AIP Conf. Proc. 745: High Energy Gamma-Ray Astronomy*.
- PRIMACK, J. R., BULLOCK, J. S., SUMMERVILLE, R. S., & MACMINN, D. 1999. Probing galaxy formation with TeV gamma ray absorption. *Astroparticle Physics*, **11**, 93.
- PROTHEROE, R. J., & MEYER, H. 2000. An Infrared Background – TeV Gamma-Ray Crisis? *Physics Letters B*, **493**, 1.
- PUNCH, M., AKERLOF, C. W., CAWLEY, M. F., CHANTELL, M., FEGAN, D. J., FENNELL, S., GAIDOS, J. A., HAGAN, J., HILLAS, A. M., JIANG, Y., KERRICK, A. D., LAMB, R. C., LAWRENCE, M. A., LEWIS, D. A., MEYER, D. I., MOHANTY, G., O’FLAHERTY, K. S., REYNOLDS, P. T., ROVERO, A. C., SCHUBNELL, M. S., SEMBROSKI, G., WEEKES, T. C., & WILSON, C. 1992. Detection of TeV photons from the active galaxy Markarian 421. *Nature*, **358**(Aug.), 477–+.
- QUINN, J., AKERLOF, C. W., BILLER, S., BUCKLEY, J., CARTER-LEWIS, D. A., CAWLEY, M. F., CATANESE, M., CONNAUGHTON, V., FEGAN, D. J., FINLEY, J. P., GAIDOS, J., HILLAS, A. M., LAMB, R. C., KRENNRICH, F., LESSARD, R., MCENERY, J. E., MEYER, D. I., MOHANTY, G., RODGERS, A. J., ROSE, H. J., SEMBROSKI, G., SCHUBNELL, M. S., WEEKES, T. C., WILSON, C., & ZWEERINK, J. 1996. Detection of Gamma Rays with  $E > 300$  GeV from Markarian 501. *ApJ*, **456**(Jan.), L83+.
- RAUE, M. 2003. *Entwicklung einer Energierekonstruktion für die H.E.S.S.-Cherenkov-Teleskope und erste Ergebnisse für den Krebsnebel*. M.Phil. thesis, Universität Hamburg.

- RAUW, G., DE BECKER, M., NAZÉ, Y., CROWTHER, P. A., GOSSET, E., SANA, H., VAN DER HUCHT, K. A., VREUX, J.-M., & WILLIAMS, P. M. 2004. WR 20a: A massive cornerstone binary system comprising two extreme early-type stars. *A&A*, **420**(June), L9–L13.
- RAUW, G., CROWTHER, P. A., DE BECKER, M., GOSSET, E., NAZÉ, Y., SANA, H., VAN DER HUCHT, K. A., VREUX, J.-M., & WILLIAMS, P. M. 2005. The spectrum of the very massive binary system WR 20a (WN6ha + WN6ha): Fundamental parameters and wind interactions. *A&A*, **432**(Mar.), 985–998.
- RAUW, G., MANFROID, J., GOSSET, E., NAZÉ, Y., SANA, H., DE BECKER, M., FOELLM, C., & MOFFAT, A. F. J. 2007. Early-type stars in the core of the young open cluster Westerlund 2. *A&A*, **463**(Mar.), 981–991.
- REIMER, A., REIMER, O., & POHL, M. 2006. Gamma rays from colliding winds of massive stars. *ArXiv Astrophysics e-prints*, Nov.
- RIPKEN, J. 2001. *Untersuchungen zur Rekonstruktion der Richtung photoninduzierter Luftschauer mit dem stereoskopischen System abbildender Cherenkovteleskope des HEGRA-Experimentes*. Diplomarbeit am Institut für Experimentalphysik, Universität Hamburg.
- RIPKEN, J. 2007. *Not yet titled*. Ph.D. thesis, Universität Hamburg.
- RIPKEN, J., & ET AL. 2005. Dark matter annihilation as possible origin of the very high energy gamma-radiation from the Galactic center measured by H.E.S.S. *Pages 151–+ of: International Cosmic Ray Conference*.
- RODGERS, A. W., CAMPBELL, C. T., & WHITEOAK, J. B. 1960. A catalogue of H $\alpha$ -emission regions in the southern Milky Way. *MNRAS*, **121**, 103–+.
- ROWELL, G. 2003. *A 'Template' Background Model in HEGRA CT-System Data Analysis*. To appear in *Astronomy and Astrophysics*.
- SALVATERRA, R., & FERRARA, A. 2003. The imprint of the cosmic dark ages on the near-infrared background. *Monthly Notice of the Royal Astronomical Society*, **339**, 973.
- SALVATERRA, R., & FERRARA, A. 2006. Where are the sources of the near-infrared background? *MNRAS*, **367**(Mar.), L11–L15.
- SAMBRUNA, R. M., AHARONIAN, F. A., KRAWCZYNSKI, H., AKHPERJANIAN, A. G., BARRIO, J. A., BERNLÖHR, K., BOJAHN, H., CALLE, I., CONTRERAS, J. L., CORTINA, J., DENNINGHOFF, S., FONSECA, V., GONZALEZ, J. C., GÖTTING, N., HEINZELMANN, G., HEMBERGER, M., HERMANN, G., HEUSLER, A., HOFMANN, W., HORNS, D., IBARRA, A., KANKANYAN, R., KESTEL, M., KETTLER, J., KÖHLER, C., KOHNLE, A., KONOPELKO, A., KORNMEYER, H., KRANICH, D., LAMPEITL, H., LINDNER, A., LORENZ, E., MAGNUSSEN, N., MANG, O., MEYER, H., MIRZOYAN, R., MORALEJO, A., PADILLA, L., PANTER, M., PLAGA, R., PLYASHESHNIKOV, A., PRAHL, J., PÜHLHOFER, G., RAUTERBERG, G., RÖHRING, A., SAHAKIAN, V., SAMORSKI, M., SCHILLING, M., SCHEMELE, D., SCHRÖDER, F., STAMM, W., TLUCZYKONT, M., VÖLK, H. J., WIEBEL-SOOTH, B., WIEDNER, C., WILLMER, M., WITTEK, W., CHOU, L., COPPI, P. S., ROTHSCHILD, R., & URRY, C. M. 2000. Correlated Intense X-Ray and TEV Activity of Markarian 501 in 1998 June. *ApJ*, **538**(July), 127–133.
- SCHACHTER, J. F., STOCKE, J. T., PERLMAN, E., ELVIS, M., REMILLARD, R., GRANADOS, A., LUU, J., HUCHRA, J. P., HUMPHREYS, R., URRY, C. M., & WALLIN, J. 1993. Ten new BL Lacertae objects discovered by an efficient X-ray/radio/optical technique. *ApJ*, **412**(Aug.), 541–549.

- SCHROEDTER, M., BADRAN, H. M., BUCKLEY, J. H., BUSSONS GORDO, J., CARTER-LEWIS, D. A., DUKE, C., FEGAN, D. J., FEGAN, S. F., FINLEY, J. P., GILLANDERS, G. H., GRUBE, J., HORAN, D., KENNY, G. E., KERTZMAN, M., KOSACK, K., KRENNRICH, F., KIEDA, D. B., KILDEA, J., LANG, M. J., LEE, K., MORIARTY, P., QUINN, J., QUINN, M., POWER-MOONEY, B., SEMBROSKI, G. H., WAKELY, S. P., VASSILIEV, V. V., WEEKES, T. C., & ZWEERINK, J. 2005. A Very High Energy Gamma-Ray Spectrum of 1ES 2344+514. *ApJ*, **634**(Dec.), 947–954.
- SHARA, M. M., SMITH, L. F., POTTER, M., & MOFFAT, A. F. J. 1991. A deep survey for Galactic Wolf-Rayet stars. I - Motivation, search technique, and first results. *AJ*, **102**(Aug.), 716–743.
- SIKORA, M., BEGELMAN, M. C., & REES, M. J. 1994. Comptonization of diffuse ambient radiation by a relativistic jet: The source of gamma rays from blazars? *ApJ*, **421**(Jan.), 153–162.
- STECKER, F. W., & DE JAGER, O. C. 1993. New Upper Limits on Intergalactic Infrared Radiation from High-Energy Astrophysics. *ApJ*, **415**(Oct.), L71+.
- STECKER, F. W., & GLASHOW, S. L. 2001. New tests of Lorentz invariance following from observations of the highest energy cosmic  $\gamma$ -rays. *Astroparticle Physics*, **16**(Oct.), 97–99.
- STECKER, F. W., DE JAGER, O. C., & SALAMON, M. H. 1996. Predicted Extragalactic TeV Gamma-Ray Sources. *ApJ*, **473**(Dec.), L75+.
- STECKER, F. W., MALKAN, M. A., & SCULLY, S. T. 2006. Intergalactic Photon Spectra from the Far-IR to the UV Lyman Limit for  $0 < z < 6$  and the Optical Depth of the Universe to High-Energy Gamma Rays. *ApJ*, **648**(Sept.), 774–783.
- STEVENS, I. R., & HARTWELL, J. M. 2003. The cluster wind from local massive star clusters. *MNRAS*, **339**(Feb.), 280–288.
- STEVENS, I. R., & POLLOCK, A. M. T. 1994. Stagnation-Point Flow in Colliding Wind Binary Systems. *MNRAS*, **269**(July), 226–+.
- TENORIO-TAGLE, G. 1979. The gas dynamics of H II regions. I - The champagne model. *A&A*, **71**(Jan.), 59–65.
- TLUCZYKONT, M. 2003. *Beobachtung und Nachweis von Aktiven Galaktischen Kernen und Suche nach Galaktischen Objekten im TeV-Energiebereich mit den HEGRA-Cherenkov-Teleskopen sowie Modellierung eines Photonspektrums durch den Zerfall neutraler Pionen aus schockbeschleunigten Hadronen*. Ph.D. thesis, Fachbereich Physik der Universität Hamburg. [dissertation.de](http://dissertation.de).
- TOLLER, G. N. 1983. The extragalactic background light at 4400 Å. *ApJ*, **266**(Mar.), L79–L82.
- TORRES, D. F., DOMINGO-SANTAMARÍA, E., & ROMERO, G. E. 2004. High-Energy Gamma Rays from Stellar Associations. *ApJ*, **601**(Jan.), L75–L78.
- TOWNSLEY, L., FEIGELSON, E., MONTMERLE, T., BROOS, P., CHU, Y.-H., GARMIRE, G., & GETMAN, K. 2005 (Apr.). Parsec-Scale X-ray Flows in High-Mass Star-Forming Regions. In: *X-Ray and Radio Connections* (eds. L.O. Sjouwerman and K.K Dyer) Published electronically by NRAO, <http://www.aoc.nrao.edu/events/xraydio> Held 3-6 February 2004 in Santa Fe, New Mexico, USA, (E3.04) 10 pages.
- TSUJIMOTO, M., *et al.* 2004. Massive Star Birth - A Crossroad of Astrophysics. In: CESARONI, R., CHURCHWELL, E., FELLI, M., & WALMSLEY, C.M. (eds), *Proc. of the IAU Symposium 227*. Cambridge University Press.
- URRY, C. M., & PADOVANI, P. 1995. Unified Schemes for Radio-Loud Active Galactic Nuclei. *PASP*, **107**(Sept.), 803–+.

- VAN DER HUCHT, K. A. 2001. The VIIth catalogue of galactic Wolf-Rayet stars. *New Astronomy Review*, **45**(Feb.), 135–232.
- VÖLK, H. J. 1983. Cosmic-ray acceleration and transport, and diffuse galactic gamma-ray emission. *Space Science Reviews*, **36**(Sept.), 3–25.
- VÖLK, H. J., & FORMAN, M. 1982. Cosmic rays and gamma-rays from OB stars. *ApJ*, **253**(Feb.), 188–198.
- WEEKES, T. C. 1989. Observation of TeV Gamma Rays from the Crab Nebula using the Atmospheric Cherenkov Imaging Technique. *The Astrophysical Journal*, **342**, 379.
- WEEKES, T. C. 2003. *Very high energy gamma-ray astronomy*. Very high energy gamma-ray astronomy, by Trevor C. Weekes. IoP Series in astronomy and astrophysics, ISBN 0750306580. Bristol, UK: The Institute of Physics Publishing, 2003.
- WESTERLUND, B. 1960. *Arkiv for Astronomi* **2**, 419.
- WHITE, R. L. 1985. Synchrotron emission from chaotic stellar winds. *ApJ*, **289**(Feb.), 698–708.
- WHITE, R. L., & CHEN, W. 1992. Pi<sup>0</sup>-decay gamma-ray emission from winds of massive stars. *ApJ*, **387**(Mar.), L81–L84.
- WHITE, R. L., & CHEN, W. 1995. IAU Symposia, 163.
- WHITEOAK, J. B. Z., & UCHIDA, K. I. 1997. High-resolution radio observations of RCW 49. *A&A*, **317**(Jan.), 563–568.
- WHITNEY, B. A., INDEBETOUW, R., BABLER, B. L., MEADE, M. R., WATSON, C., WOLFF, M. J., WOLFIRE, M. G., CLEMENS, D. P., BANIA, T. M., BENJAMIN, R. A., COHEN, M., DEVINE, K. E., DICKEY, J. M., HEITSCH, F., JACKSON, J. M., KOBULNICKY, H. A., MARSTON, A. P., MATHIS, J. S., MERCER, E. P., STAUFFER, J. R., STOLOVY, S. R., & CHURCHWELL, E. 2004. A GLIMPSE of Star Formation in the Giant H II Region RCW 49. *ApJS*, **154**(Sept.), 315–321.
- WOLTER, A., COMASTRI, A., GHISELLINI, G., GIOMMI, P., GUAINAZZI, M., MACCACARO, T., MARASCHI, L., PADOVANI, P., RAITERI, C. M., TAGLIAFERRI, G., URRY, C. M., & VILLATA, M. 1998. BeppoSAX spectral survey of soft X-ray selected BL Lacertae objects. *A&A*, **335**(July), 899–911.
- WOO, J.-H., URRY, C. M., VAN DER MAREL, R. P., LIRA, P., & MAZA, J. 2005. Black Hole Masses and Host Galaxy Evolution of Radio-Loud Active Galactic Nuclei. *ApJ*, **631**(Oct.), 762–772.
- WRIGHT, E. L., & REESE, E. D. 2000. Detection of the Cosmic Infrared Background at 2.2 and 3.5 Microns Using DIRBE Observations. *The Astrophysical Journal*, **545**, 43.
- ZATSEPIN, G. T., & KUZ'MIN, V. A. 1966. Upper Limit on the Spectrum of Cosmic Rays. *JETP Letters*, **4**, 78.

# Acknowledgments

Foremost I wish to thank Götz Heinzelmann for the support and the excellent working conditions at the Institut für Experimentalphysik, Hamburg. I always had the freedom and the support to follow my interests. I also would like to thank Götz Heinzelmann for the opportunity to spend time at the H.E.S.S. experiment in Namibia and to participate in many different scientific conferences.

Furthermore I would like to thank the members of the Hamburg group Matthias Beilicke, Rene Cornils, Niels Goetting, Joachim Ripken and Martin Tluczykont for the good atmosphere, inspiring discussions and the help in preparing this manuscript. I also would like to thank my collaborators Daniel Mazin and Olaf Reimer for our productive work together and I hope for more collaborative work in the future.

I wish to thank Chris for the support over all these years. Your thorough proof reading of the manuscript hugely improved the readability of this thesis and maybe (hopefully, surely) your understanding of my work. Thank you for the dinner!

This work has been supported by the Bundesministerium für Bildung und Forschung.